EEE4113F Group 1 Final Report

Group 1:
Phila Haanyama (HNYPHI001)
Daniel Kreuzer (KRZDAN001)
Lulama Lingela (LNGLUL002)
Bume Mxenge (MXNBUM001)

Prepared for:
EEE4113F
Department of Electrical Engineering
University of Cape Town

May 19, 2026

Declaration

1. I know that plagiarism is wrong. Plagiarism is to use another's work and pretend that it is one's own.
2. I have used the IEEE convention for citation and referencing. Each contribution to, and quotation in, this report from the work(s) of other people has been attributed, and has been cited and referenced.
3. This report is my own work.
4. I have not allowed, and will not allow, anyone to copy my work with the intention of passing it off as their own work or part thereof.

May 19, 2026

Phila Haanyama, Daniel Kreuzer, Lulama Lingela, Bume Mxenge   Date

Acknowledgements

To Dan - the mind behind FAPDM-AUV (Fully Autonomous Phytoplankton Data Measurement - Autonomous Underwater Vehicle)

This report is dedicated to MJ&PPG (Buttercup, Bubbles, Blossom, Mojo Jojo and most importantly - Professor Utonium)

Figure 1: Lebron

Lastly we'd like to dedicate this project to our knight in shining armour, our light in the darkness, our North star: LeBron Raymone James. Boy oh boy where do we even begin. Lebron... honey, our pookie bear. We have loved you ever since we first laid eyes on you. The way you drive into the paint and strike fear into your enemies eyes. Your silky smooth touch around the rim, and that gorgeous jumpshot. We would do anything for you. We wish it were possible to freeze time so we would never have to watch you retire. You had a rough childhood, but you never gave up hope. You are even amazing off the court, you're a great husband and father, sometimes we even call you dad. We forever dread and weep, thinking of the day you will one day retire. We would sacrifice our own lives it were the only thing that could put a smile on your beautiful face. You have given us so much joy, and heartbreak over the years. We remember when you first left Cleveland and it was like our hearts got broken into a million pieces. But a tear still fell from our collective right eyes when we watched you win your first ring in miami, because deep down, our glorious king deserved it. I just wanted you to return home. Then allas, you did, our sweet baby boy came home and we rejoiced. 2015 was a hard year for us baby, but in 2016 you made history happen. You came back from 3-1 and we couldn't believe it. We wer crying, bawling even, and we heard our glorious king exclaim these words, 'CLEVELAND, THIS IS FOR YOU!' Not only have you changed the game of basketball and the world forever, but you've eternally changed our worlds. And now you're getting older, but still the goat, our goat. We love you pookie bear, our glorious king, Lebron James.

Abstract

This report presents the design, simulation, and validation of a profiling float for phytoplankton concentration measurement in Antarctic waters. Phytoplankton are critical indicators of ocean health and climate change, yet current measurement methods rely on manual vessel-based sampling that is labour-intensive, expensive, and limited in spatial and temporal resolution in remote polar environments. The proposed solution addresses this by enabling autonomous, repeatable depth profiling without human intervention.

The vehicle operates on a buoyancy engine principle: a motor-driven piston mechanism displaces water into and out of an internal chamber to regulate vehicle density and therefore depth, eliminating the need for thrusters and minimising power consumption. The complete system was designed by a team of four students over ten weeks within a hardware budget of R2 000, and is validated as a proof-of-concept targeting a maximum operating depth of 2 m.

The system is decomposed into four subsystems: Depth Actuator, Depth Controller, Power, and Housing.

System-level validation was performed through subsystem-level simulation and hardware testing. All primary acceptance test procedures are performed and discussed. The design demonstrates that autonomous buoyancy-driven depth control is achievable within the constraints of the project, and provides a validated foundation for scaling toward operational Antarctic deployment.

Contents

List of Figures

Chapter 1

Introduction

1.1 Background

Phytoplankton are microscopic photosynthetic organisms that form the foundation of aquatic food webs and contribute approximately half of global oxygen production. Monitoring phytoplankton concentration is therefore an important indicator of ocean health, climate change, and marine ecosystem productivity. In Antarctic waters, phytoplankton blooms are highly sensitive to environmental conditions, making their measurement particularly valuable for climate and ecological research. Current methods typically rely on manual sampling from research vessels or fixed buoy systems, which are costly, labour-intensive, and limited in spatial and temporal resolution, especially in remote polar environments.

1.2 Problem Statement

At the Design School (D-School), the team participated in activities focused on stakeholder engagement, problem identification, brainstorming, and prototype development. These sessions emphasised understanding the client's needs from a user-centred perspective rather than approaching the problem only from a technical viewpoint. The team practiced interviewing stakeholders, developing problem statements, and presenting prototype concepts for peer review. Feedback received during these reviews helped identify design blind spots and improve communication of ideas in preparation for meeting the clients from the Marine and Antarctic Research Centre for Innovation and Sustainability (MARiS).

Sandy Thomalla is a biologist working at the Council for Scientific and Industrial Research (CSIR) and MARiS, studying phytoplankton in the Antarctic. The existing tools that she has for phytoplankton data collection are expensive and require deployment from research vessels, thus making large-scale data collection impractical. Additionally, the unique harshness of the Southern Ocean adds significant challenges to data collection. Owing to this, Sandy needs a way to gather long-term data sets of phytoplankton concentrations throughout the Southern Ocean, that is autonomous, accurate, cost-effective, and durable enough to withstand Antarctic conditions.

1.3 Objectives

This project addresses Sandy's need for an autonomous system capable of measuring phytoplankton concentration at specified depths without continuous human intervention. The proposed solution is an autonomous profiling float that regulates depth using a piston-based buoyancy engine. Retracting the piston draws seawater into an internal chamber, increasing the vehicle's density and causing it to descend, while extending the piston expels water and restores buoyancy, causing the vehicle to rise. This approach, similar to that used in underwater gliders, eliminates the need for propellers or thrusters and therefore reduces power consumption and mechanical complexity.

The vehicle is designed as a proof-of-concept (POC) system targeting a maximum operating depth of 2 m. This allows the core depth-control functionality to be developed and validated within the project's time and resource constraints while demonstrating principles that could be extended to deeper deployments.

1.4 System Requirements

The complete system is divided into four subsystems, each designed by a separate group member:

- **Control Actuator - KRZDAN001:** Design and implementation of the actuation mechanism used in the buoyancy engine.
- **Controller - HNHPYI001:** Design and implementation of the cascaded feedback control system regulating vehicle depth using pressure sensor and shaft velocity feedback.
- **Housing - LNGLUL002:** Design of the multi-zone enclosure, including the piston-based buoyancy chamber, external sensor mounting interfaces, sealing mechanisms, and passive stability through ballast mass distribution.
- **Power - MXNBUM001:** Design and implementation of the power supply system, used to power loads, monitor and protect the battery, and maintain high electrical efficiency.

1.5 Scope & Limitations

The scope of this report is limited to proof-of-concept autonomous depth regulation along the vertical axis. Lateral navigation, attitude control, and the internal operation of the phytoplankton sensing payload are outside scope. The design was additionally constrained by a total project budget of R2 000, a team size of four students, and a 10-week development period. These constraints influenced component selection, limited the extent of hardware testing, and favoured solutions that could be validated efficiently through modelling and simulation.

1.6 Report Outline

Although the system is not intended for immediate Antarctic deployment, the project demonstrates the feasibility of autonomous buoyancy-driven depth control using a low-cost embedded platform. The report presents the system requirements, design decisions, modelling, controller development, simulation-based validation, and recommendations for future improvement.

The complete project source code, simulation files, and supporting documentation are available in the project GitHub repository: [https://github.com/Phila-H-23/AUV-Phytoplankton-Project].

Chapter 2

Literature Review

2.1 Background

Phytoplankton in the Southern Ocean are a key component of the global carbon cycle, contributing significantly to marine primary production and facilitating the export of atmospheric carbon to the deep ocean. Globally, marine phytoplankton dominate primary production across approximately 70% of the Earth's surface and play a central role in ocean carbon sequestration [4]. In particular, the Antarctic Marginal Ice Zone is a highly productive and dynamic region, where interactions between sea ice, stratification, and light availability drive phytoplankton growth and variability [5]. These processes are strongly influenced by environmental factors such as temperature and ocean variability, which significantly impact phytoplankton distribution and diversity [4].

Despite their importance, current methods for measuring phytoplankton concentrations rely predominantly on ship-based sampling and satellite observations. Ship-based methods are costly and geographically limited, while satellite-derived chlorophyll-*a* measurements are restricted to surface observations and are sensitive to environmental variability [5]. Furthermore, phytoplankton datasets remain sparse and unevenly sampled at the global scale, particularly in polar regions, limiting the ability to accurately characterise spatial and temporal dynamics [4]. These challenges are exacerbated during the Antarctic winter due to sea ice coverage and extreme weather, resulting in significant temporal gaps in data.

These limitations motivate the development of autonomous, persistent ocean monitoring systems capable of year-round operation in polar environments [4]. Such systems must address key engineering challenges, including energy efficiency, environmental robustness, sensing reliability, and limited communication in ice-covered and GPS-denied conditions [4].

This literature review evaluates existing autonomous marine technologies for Antarctic phytoplankton monitoring. It examines platform architectures, depth sensing and control strategies, and data acquisition and communication methods, with the aim of identifying key design constraints and informing the development of a scalable, long-term monitoring solution.

2.2 Autonomous Marine Architectures for Polar Exploration

2.2.1 Classification of Autonomous Marine Architectures

The design of long-term autonomous sensing systems for the Southern Ocean requires architectures capable of withstanding extreme pressures, harsh environmental conditions, and the polar night data gap. Ocean observation technologies have evolved from static, single-node platforms to distributed, multi-node systems that improve spatial and temporal sampling resolution [6, 7].

Lagrangian Drifters and Profiling Floats

Lagrangian floats are water-following platforms that sample vertical water columns over extended periods [8, 6]. They utilise buoyancy-driven mechanisms to profile depths of 1,000–2,000 m, monitoring temperature, salinity, and biogeochemical properties [9, 10]. Buoyancy control is typically achieved through oil pumping systems or piston-driven actuators, enabling controlled ascent and descent [11, 12]. Their low energy consumption and cost-effectiveness make them suitable for large-scale deployments such as the Argo programme [9, 10, 13]. However, their passive horizontal drift limits spatial control. In polar environments, ice-sensing algorithms are required to prevent surfacing beneath sea ice, with data buffered until communication is possible [10, 13].

Autonomous Underwater Gliders (AUGs)

Autonomous underwater gliders convert buoyancy changes into forward motion using fixed wings, producing a characteristic sawtooth trajectory. This approach enables highly energy-efficient operation, supporting missions lasting several months [14, 15]. Despite their endurance, gliders operate at low speeds (0.25–0.5 m/s) and have limited manoeuvrability, reducing their effectiveness in strong currents or complex under-ice environments [14].

Autonomous Underwater Vehicles (AUVs)

AUVs are propeller-driven platforms designed for high-resolution mapping, targeted sampling, and under-ice exploration. They offer high manoeuvrability and speeds exceeding 1 m/s, enabling detailed surveys of seafloor and ice-shelf structures [16]. Operation in GPS-denied environments requires navigation systems integrating DVL, INS, and sensor fusion techniques [16, 17]. While these systems enable precise positioning, they increase complexity and energy consumption. As a result, AUVs are constrained by mission duration and face operational risks in under-ice environments [16].

Unmanned Surface Vehicles (USVs)

USVs operate at the air–sea interface and function as communication relays, energy hubs, and coordination platforms for multi-vehicle systems [8, 18]. Hybrid architectures integrating USVs with AUVs and UAVs enable multi-domain sensing and extended mission capabilities. The Small Waterplane Area Twin Hull (SWATH) design provides enhanced stability and reduced wave-induced motion compared to monohull vessels, along with increased deck space for scientific payloads [8]. To support long-term deployments, hybrid energy systems combining wind propulsion and marine current harvesting have been proposed, enabling continuous operation during polar winter [8, 18].

2.2.2 Comparative Analysis and Design Trade-offs

Selecting an optimal architecture for Antarctic phytoplankton sensing requires resolving key trade-offs between mission persistence, spatial controllability, energy consumption, and system cost. Table 2.1 summarises these trade-offs across established autonomous marine platforms.

Table 2.1: Engineering Comparison of Autonomous Marine Platforms

Platform Type	Persistence	Control Mode	Typical Speed	Relative Cost
Profiling Float	3–4 Years	Passive (Drifting)	$< 0.2\,\mathrm{m/s}$	Low
AUG (Glider)	Months	Buoyancy-Driven	0.25–$0.5\,\mathrm{m/s}$	Moderate
AUV (Propelled)	1–30 Days	Active Precision	$> 1.0\,\mathrm{m/s}$	High
USV (SWATH)	Seasonal/Continuous	Hybrid (Wind/Solar/Current)	1.2–$1.7\,\mathrm{m/s}$	High (System-Level)

Persistence, control, speed characteristics, and cost summarised from [9, 10, 11, 14, 16, 8].

The dominant trade-off lies between persistence and controllability. Profiling floats achieve multi-year deployments with minimal energy consumption through passive advection, but lack horizontal control, limiting their ability to target dynamic features such as phytoplankton blooms [9, 11]. In contrast, AUVs provide precise navigation and high-resolution sampling via advanced navigation systems (INS/DVL), but their propulsion-driven operation results in high energy consumption and short mission durations (days to weeks) [16, 17].

Gliders occupy an intermediate position, trading speed and maneuverability for improved endurance through buoyancy-driven propulsion. While effective for large-scale transects, their limited speed and reduced authority in strong currents constrain their use in dynamic polar environments [14].

Surface platforms, particularly SWATH-based USVs, provide complementary capabilities as persistent energy and communication hubs. Their stability in high sea states and ability to harvest environmental energy enable long-duration missions and coordination with subsurface assets, addressing the energy and communication constraints of underwater vehicles [8].

Design Implication: No single platform satisfies both persistence and controllability requirements. Passive systems offer endurance but lack targeting capability, while active systems provide precision but are energy-limited. This motivates a hybrid, multi-platform architecture combining persistent surface or drifting systems with mobile subsurface vehicles to achieve both coverage and resolution [8, 6].

Hydrodynamics and Movement

Hydrodynamic efficiency directly determines vehicle endurance by influencing drag and energy consumption. AUVs employ streamlined, torpedo-like geometries to minimise drag and maximise propulsion efficiency [16], while gliders use lifting surfaces to convert vertical buoyancy changes into forward motion, significantly reducing energy use at the expense of speed and manoeuvrability [14]. Profiling floats prioritise vertical stability but exhibit low damping and high inertia, leading to depth control challenges in dynamic environments. Segmented PD control methods improve depth convergence without requiring environment-specific tuning [11, 19, 20]. For surface platforms, stability is critical in the Southern Ocean. SWATH designs reduce wave-induced motion by minimising the waterplane area, improving seakeeping and enabling reliable deployment of subsurface systems [8].

Materials and Structural Geometry

Material selection governs structural integrity, buoyancy, and payload capacity. For deep-sea applications, composite materials such as carbon/epoxy offer up to 46% weight reduction compared to metallic alloys while maintaining sufficient buckling resistance at depth [21]. In polar environments, materials must also withstand low temperatures and corrosion. Low-density polymers such as polypropylene provide inherent buoyancy, corrosion resistance, and suitability for sub-zero conditions [22, 21]. Encapsulation materials are critical for protecting electronics, with low-permeability elastomers preferred for long-term reliability. Acoustic compatibility must also be considered for sonar and communication systems [23].

Design Implication: Lightweight composites and polymer-based structures increase payload capacity and energy efficiency, enabling greater sensor integration within the constraints of polar deployment environments.

2.2.3 Innovative Technologies for Polar Systems

Polar observation systems must operate under extended darkness, limited communication, and extreme conditions. These constraints have driven the development of technologies that enable long-term autonomous operation [8, 6].

Open-Source Hardware and Modular Integration

Open-source hardware has reduced the cost and complexity of large-scale deployments. Modular embedded platforms enable flexible integration of sensing, communication, and storage systems [24]. For example, “waves-in-ice” instruments can be built for approximately $2,000, enabling scalable deployment compared to proprietary alternatives [24, 25]. To improve reliability, these systems increasingly incorporate onboard processing and real-time operating systems, allowing high-frequency sampling and reducing dependence on continuous communication.

Biofouling Mitigation for Optical Sensing

Biofouling degrades optical measurements over time, limiting long-term deployment of phytoplankton sensors [26]. Copper-based mitigation strategies create localised toxic environments that inhibit biofilm formation, extending reliable operation from days to over a year [26]. This is essential for polar systems, where maintenance is not feasible during winter.

2.3 Depth Control and Sensing

2.3.1 Depth Sensing Methods

An essential part of data collection at varying depths is accurate and reliable depth control and sensing. As such, there is a significant body of research addressing these topics. Far and away the most common technique used here is to use pressure sensors [17],[19],[27]. These are relatively inexpensive and allow for precise conversions from pressure to depth due to the high pressure gradient of water and sensors for various exploration depths are readily available [17].

2.3.2 Depth Control Methodologies

Buoyancy vs Thruster Systems

Depth control actuation methods on AUVs can be broadly categorized into two categories: Thruster based and buoyancy based actuation methods [19]. Thrust based depth control actuation here, refers to the use of propellers to apply a downwards force to submerge an AUV towards the desired target depth. These systems rely on the AUV having a positive buoyancy in water, such that when no force is supplied by the propellers the AUV will move up towards the surface automatically.[19]. On the other hand, buoyancy based methods rely on either variable mass (ballast) or variable volume systems [27] to alter either the buoyant or gravitational force to move up and down the water column [27]. In rare cases, these can be combined to get the advantages of each, such as in the SOTAB-I, described by Choyekh et al., an AUV made to investigate oil spills, which uses a combination of a hydraulic oil pump to alter the volume of the vehicle through an oil bladder and thrusters to provide an additional control[20].

In a paper by Morales-Aragón et al. [19] these two methods were directly compared in a salt-water lagoon environment. The results showed similar performance with a mean absolute depth error (MADE) of $5.7cm$ for the variable ballast system (VBS) and a MADE of $5.6cm$ for the thruster system[19]. Furthermore, the thruster system was found to have a battery life of 127 days for for the configuration used, whilst the VBS had a battery life of 48 days[19]. This discrepancy was due to the heavy and slow piston used, to let water into and push water out of the ballast. This slow response of the piston (approximately $18s$ for a full extension) also led to some overshooting in the step responses [19].

Ultimately however, in practical conditions Morales-Aragón et al. found that the VBS was a far more reliable due to the effects of bio-fouling (accumulation of organic material on the body of the AUV) on the differing systems [19]. In the lagoon where the AUVs were tested significant bio-fouling caused severe disruption to the thruster based system due to the additional mass added to the vehicle. The added mass resulted in the thruster based AUV no longer having a baseline positive buoyancy, making resurfacing impossible without continuous use of the propellers which would have quickly drained the battery. This limited the practical time of autonomy to only a few days, which was deemed insufficient for the required application [19].The VBS method, however was shown to be robust to the effect of bio-fouling leading to a much greater number of days of autonomy. Furthermore, Morales-Aragón et al. also determined the risk of exposure to the marine environment to be far lower for the VBS system, bolstering their choice actuation methods.

Variable Mass(ballast) vs Variable Volume Systems

Both variable mass and variable volume buoyancy systems are used widely throughout the literature. Variable mass systems are often implemented through the use of a ballast tank, into which water is admitted or expelled to alter the weight of the vehicle, as in the system described by Morales-Aragón et al. [19]. Variable volume systems instead alter the overall displacement of the vehicle to change the buoyant force acting upon it. A simple example of such a mechanism, described by Kim et al., is a cylinder that protrudes outwards from the main body of the AUV to displace water and increase buoyancy, and retracts to decrease buoyancy by decreasing volume, whilst also increasing mass by letting water in, thereby making it a combination of these 2 types of systems [12]. A more sophisticated implementation is an oil bladder system, wherein oil is pumped between an internal reservoir and an external flexible bladder, increasing the external volume of the vehicle when inflated [20], [27].

A key consideration in the choice between these approaches is the working fluid used. Elkolali et al. note that oil-based variable volume systems benefit significantly from the roughly 45 times greater viscosity of oil compared to seawater [27]. The lower viscosity of seawater, when used as the working fluid in ballast systems, can lead to accelerated erosion of moving components and greater energy losses due to reduced lubrication [27]. Elkolali et al. proposed a miniature electro-hydraulic variable buoyancy system making use of an oil bladder, a bi-directional internal gear micro-hydraulic pump coupled to a brush-less DC motor, a servo-actuated control valve, and position sensors to measure oil transfer [27]. This system was shown to be operational at depths of up to $400m$, and was designed to fit within a cylindrical volume of only $80mm$ in diameter and $600mm$ in length, with a total mass of approximately 1.95–2 kg [27]. However, the energy efficiency of the proposed design was found to be consistently below 30%, representing a notable drawback [27].

2.3.3 Control Algorithms

A range of control algorithms have been applied to AUV depth control in the literature. The most common approach is the PID controller, which was used in the thruster-based system evaluated by Morales-Aragón et al. [19]. However, due to the non-linearities present in many buoyancy-based systems, more complex control structures are often required[19]. In the VBS developed by Morales-Aragón et al., a cascaded control architecture comprising three nested loops was employed [19]. The innermost loop managed the piston position using a three-state logic approach (filling, emptying, and stopping), the middle loop used a PID controller to regulate the ascent speed of the AUV, and the outermost loop controlled the target depth [19]. This system achieved a MADE of 5.7 cm, with 90.54% of samples falling within a $\pm$10 cm dead-band [19]. It is worth noting that achieving zero steady-state error would require the piston to be in continuous motion; the dead-band was therefore a deliberate design choice to conserve energy [19].

A predictive controller was used in the SOTAB-I system described by Choyekh et al. [20]. This choice was motivated by the known limitations of PID control for buoyancy-driven systems, namely that the actuators must remain active continuously, and the forces and rate of buoyancy change vary considerably for large depth ranges, requiring PID parameters to be retuned as the vehicle descends [20].

A more advanced approach is the sliding mode active disturbance rejection controller (SM-ADRC) presented by Zhang et al. [28]. This controller is composed of three components: a tracking differentiator, an extended state observer, and a non-linear state error feedback law. Simulation results demonstrated significant improvements over a traditional PID controller in terms of setpoint tracking, overshoot, disturbance rejection, and settling time [28]. However, the work remained at the simulation stage and no physical implementation was reported [28].

2.4 Power Systems and Energy Management

This section examines how autonomous polar measurement systems are powered, sustained, and kept operational during long deployments. Across the literature, the power subsystem is a primary design driver rather than a supporting detail. It determines mission length, sensing cadence, data handling and communication frequency. The general pattern is that small polar instruments remain battery-limited, while renewable generation becomes practical only once the platform is large enough to absorb the added mass, control hardware and environmental uncertainty of the renewable system [29, 24, 30, 18, 31].

2.4.1 Energy Supply and Storage for Polar Autonomy

For compact systems, batteries remain the most credible baseline. The value of battery-only operation is not simply simplicity. It is predictability. OpenMetBuoy shows that a tightly managed lithium battery design can deliver around 4.5 months of operation on two SAFT LSH20 D-cells without solar input, provided that GNSS (Global Navigation Satellite System) fixes, wave measurements and Iridium transmissions are kept to modest intervals [29]. SHARC points to the other side of the same trade-off. Once the system moves to continuous operation, high-frequency IMU sampling, onboard processing and more frequent transmission, the required energy reserve increases sharply, to the point that an eight-cell Li-$SOCl_2$ pack with a conservative 50% derating still yields about nine days of estimated endurance [30]. The broader point is that battery-only architectures scale well only while the load profile remains disciplined [29, 30].

Renewable generation can extend endurance, but the literature shows that its value depends strongly on platform scale and environmental exposure. At station scale, ARC-MO combines solar and wind generation with a 30 kWh lead-acid bank and 24 V distribution, and supports a large sensor estate by switching on high-power equipment only when needed [18]. Solar is attractive in the bright season, but the same study shows that its output falls to zero during the polar night, leaving winter operation dependent on wind alone. It also notes that snow accumulation can shadow modules to the point that the container system requires a specific vertical dual-string arrangement to retain partial output under snow cover [18]. Wave harvesting offers another route, and Arctic-TENG demonstrates that it can support sparse satellite communications using a supercapacitor and a dedicated power management circuit [31]. However, for small floating systems, harvesting hardware also adds enclosure and interface complexity. The broader buoy literature shows that exposed or elevated hardware is vulnerable to burial by snow, while ocean-going platforms require carefully designed housings, waterproof interfaces and watertight cabins to remain reliable in service [24, 32, 25]. The implication is that solar, wind, and wave energy are all technically useful, but for a compact, low-cost Antarctic node, they are better viewed as augmentations to a battery-led design than as the primary basis for autonomy [18, 31].

Battery selection should also be treated as a cold-environment design problem rather than a catalogue choice. Li-$SOCl_2$ chemistry appears repeatedly in the polar buoy literature due to its high energy density, low self-discharge, and good low-temperature suitability [29, 30]. Even so, the battery study shows that low temperature and higher current draw reduce the head voltage and effective load capacity. At $-40\,°C$, voltage sag becomes severe under heavier discharge, and ageing worsens that behaviour further [33]. This matters directly for autonomous systems because the most demanding events are rarely steady loads. They are short current bursts during communication, wake-up and subsystem startup. In practice, cell selection, derating, and regulator sizing must be considered together [29, 30, 33].

2.4.2 Power Distribution, Regulation and Switched Subsystem Control

The stronger designs in the literature do not continuously expose every subsystem to the battery; they separate a low-power supervisory layer from switched measurement and communication loads. In the Cold Regions instrument, a dedicated power-control module remains on, manages charging and decides when to wake the logger. In contrast, the logger, Raspberry Pi processing stage and Iridium modem are active only during defined measurement and transmission windows [24]. The same architectural principles apply to the borehole measurement system, where the battery logger unit acts as a master controller, provides controllable power outputs to the measurement and camera subsystems, and monitors battery state and temperature [34]. This is an important design lesson. Long polar endurance depends as much on how power is distributed and gated as on the stored energy itself [24, 34].

This separation also improves subsystem flexibility. The Argo literature shows that when a platform must support both core functions and evolving payloads, a modular power-and-control structure is more valuable than a single undifferentiated supply rail. Core Argo floats use battery power across communications, sensors, control and hydraulic buoyancy systems, while the newer NAOS architecture introduces separate boards for core float management and payload functions [10, 13]. That arrangement protects the essential mission functions while allowing the payload side to evolve. For this project, the same logic supports a modular add-on power subsystem.

2.4.3 Principal Energy Burdens over Long Deployments

The dominant energy burdens are consistent across the literature. Communication produces the most demanding instantaneous loads, while sensing, onboard processing and actuation determine the average energy drain over time. OpenMetBuoy quantifies this clearly. Its Iridium transmission mode draws bursts up to 250 mA, far above sleep, GNSS or wave-measurement modes, which is why a stable buck-boost rail is required even in an otherwise low-power design [29]. Arctic-TENG reaches the same conclusion from the opposite direction by directly measuring the communication side. Its satellite payload requires 15.6 J per transmission, enough to make the communication schedule a first-order design parameter rather than a housekeeping decision [31].

The instrument's behaviour between transmissions then sets the average consumption. SHARC shows how costly continuous operation becomes once high-rate IMU logging, an onboard DSP, and local storage are added to the mission [30]. Argo systems show that mechanical autonomy also has a price, because the battery must support communications, sensing and the hydraulic work needed to control buoyancy [10], while NAOS explicitly targets lower-power hydraulic systems to increase the number of achievable cycles [13]. Therefore, it can be inferred that endurance is rarely lost to a single component in isolation. It is lost when too many expensive functions are simultaneously treated as essential [10, 13].

2.4.4 Endurance Management and Implications for This Project

The literature is most consistent on one point. Long deployment life is won primarily through load management. OpenMetBuoy reduces demand through low-power firmware, sleep states, buffered binary packets and adjustable measurement rates over a two-way Iridium link [29]. The earlier Cold Regions design follows the same logic through periodic wake-up, short measurement windows, local processing and compressed transmission [24]. Even the larger observatory and float platforms rely on selective activation and mission configuration to keep energy use within a survivable envelope [18, 10, 13]. In other words, endurance is not just a battery-sizing problem. It is a scheduling problem [29, 24, 18, 10, 13].

For this project, that narrows the most defensible design direction. A first proof of concept under a tight budget is better aligned with a battery-dominant architecture than with full renewable dependence. The most transferable features from the literature are:

- cold-tolerant battery cells
- conservative derating
- a regulated power rail sized for communication peaks
- switched payload outputs
- battery monitoring
- local storage with reduced transmission frequency

By contrast, container-scale hybrid generation is too large and costly, whereas wave harvesting is better suited to very small data payloads or late-stage augmentation [18, 31]. Continuous high-rate sensing, as in SHARC, is also unlikely to be justified in an early low-cost prototype unless it is central to the scientific objective [30]. The opportunity, therefore, is not to maximise subsystem complexity, but to combine modest stored energy with disciplined power delivery and a tightly managed duty cycle. That is the approach most likely to remain scalable, affordable and credible for Antarctic deployment [29, 24, 30, 18, 31, 10, 13, 34, 33].

2.5 Applications and Limitations

Autonomous ocean monitoring systems have become increasingly important for collecting both environmental and biological data in remote marine environments. These systems include Autonomous Underwater Vehicles (AUVs), underwater gliders, and other robotic sensing platforms. As highlighted by Zhang et al. such systems form the foundation of modern ocean frameworks which enables large-scale and long-term data acquisition that would otherwise not be possible using traditional ship-based methods [35].

Autonomous platforms are developed for long-term ocean observation. As highlighted by Testor et al., these systems enable “continuous monitoring in harsh and remote environments where traditional methods are limited” [15]. This capability is especially important in polar regions as research vessels are unable to operate throughout the year.

Autonomous systems are also widely used in climate monitoring and oceanography. Riser et al. note that these platforms allow for “the observation of biochemical processes over large spatial and temporal scales” [7], which is critical for understanding ocean circulation and carbon cycling. This is particularly relevant in the Southern Ocean as phytoplankton play a key role in carbon sequestration.

Recent work has explored adaptive sampling techniques where systems respond dynamically to environmental conditions. For example, Smith et al. demonstrate that autonomous platforms can “adjust their sampling strategy based on real-time data to improve the detection of features such as phytoplankton blooms” [36]. This represents a shift towards more intelligent and efficient data collection.

Furthermore, there is an emergence of distributed monitoring systems distributed monitoring systems where “heterogeneous autonomous platforms collaborate to provide comprehensive environmental data” [37]. This integration allows more comprehensive and scalable ocean observation.

2.5.1 System Limitations

Despite these advantages, there are several limitations to autonomous ocean monitoring systems that restrict their effectiveness.

One of the most significant challenges is the energy limitation. As discussed by Wang et al. “the low power consumption of gliders limits their speed and payload capacity” [38]. This creates a trade-off between mission duration and sensing capability. Similarly Zhang et al. note that propeller-driven AUVs consume significantly more energy which in turn limits the possible mission duration and operational range [35].

Another limitation is navigation and localisation. Since GPS signals cannot be transmitted through water, alternative methods for localisation and navigation must be employed. Paull et al. explain that “inertial and dead-reckoning navigation methods accumulate error over time,” which will then lead to positional drift [17]. This issue is further exacerbated in polar environments where “dynamic ocean currents and movement introduce additional uncertainty in vehicle positioning” as pointed out by Garau et al. [37].

Communication constrains also pose a signifiant challenge. Underwater communication relies on acoustic signals, which are inherently limited. This is owing to the low bandwidth and high latency of acoustic signals which makes transmitting real-time data challenging [35]. As a result, these systems must operate with a high degree of autonomy.

Environmental conditions introduce additional constraints, particularly in Antarctic regions. Obstacles such as ice coverage can significantly affect the autonomous system’s navigation accuracy and ability to transmit data [15]. Additionally, ice prevents vehicles form surfacing, which is critical if GPS signals are being used for updates and satellite communication, increasing the risk of mission failure.

Finally, there are limitations related to biological sensing accuracy. Riser et al. note that “fluorescence-based measurement can be influenced by environmental conditions such as light and temperature” [7], which introduces uncertainty in phytoplankton estimation. This reduces the reliability of the data collected by autonomous systems.

2.5.2 Identified Gaps

The literature highlights several gaps that limit the effectiveness of current autonomous ocean monitoring systems, particularly for long-term phytoplankton monitoring in Antarctic environments.

Firstly, there is a lack of solutions that are scalable while also being cost-effective. Zhang et al. argue that “the high cost and operational complexity of current AUV systems limit their accessibility and scalability” [35]. This restricts widespread deployment and continuous monitoring.

Secondly, current systems are not dully capable of robust navigation in ice-covered environments. The dynamic and unpredictable ice conditions in the Southern ocean rendering route planning challenging [37]. This highlights the need for more reliable autonomous navigation strategies.

Zhang et al. suggest that “future systems must incorporate greater autonomy to compensate for limited communication capabilities” [35]. This is to address the communication limitation which remains to be a major barrier without improved onboard intelligence.

2.6 Conclusion

This review has analysed current autonomous marine systems for Antarctic phytoplankton monitoring and identified key trade-offs between persistence, controllability, and energy consumption. Profiling floats provide long-term, low-cost deployment but lack spatial control, while AUVs enable precise sampling at the expense of limited endurance. Gliders offer an intermediate solution but remain constrained in dynamic polar environments.

A key insight from the literature is that no single platform satisfies all system requirements. This motivates a hybrid, multi-platform architecture that combines persistent platforms for large-scale coverage with mobile systems for targeted sampling. Surface vehicles are particularly important as communication relays and energy hubs, helping to overcome underwater communication and power limitations.

Several critical constraints must be addressed in the system design. These include limited energy availability, especially during polar winter, unreliable communication under ice, navigation challenges in GPS-denied environments, and reduced sensing accuracy due to environmental effects such as biofouling and light variability.

From these findings, the proposed design must prioritise: (i) energy-efficient operation to enable long-term deployment, (ii) robust and modular sensing systems to maintain data quality, (iii) reliable data storage and delayed communication strategies, and (iv) a system architecture that balances coverage with adaptability.

Overall, the literature supports the development of an integrated, scalable, and resilient autonomous system capable of continuous operation in extreme Antarctic conditions, forming the basis for improved long-term phytoplankton monitoring.

Chapter 3

Control Actuator Subsystem

Prepared By: Daniel Kreuzer - KRZDAN001

3.1 Introduction

This chapter details the design and implementation of the electro-mechanical actuation subsystem for the AUV depth controller. The objective was to develop a robust, efficient, and easily controllable system tailored to our objectives. This is crucial for the measurement of phytoplankton concentrations, since it allows us to measure phytoplankton activity at multiple depths in the water column to get a more complete picture of phytoplankton populations in the Southern Ocean.

The scope of this subsystem includes the motor sizing, and drivetrain layout only. It does not discuss the control algorithm used to control the system or the housing it fits into. Lastly, the maximum depth for the prototype was established at $2m$, though considerations are made for the $100m$ depth final design.

3.1.1 Choice of Mechanism

A Variable Ballast System (VBS) utilizing a linear actuator-driven piston was selected over a Variable Volume System (VVS). This allows for greater design simplicity and mitigates risks of catastrophic failure due to damage to the internal bladder used in a VVS, which could cause leakage, subsequent damage to electronics and buoyancy loss. (see 2.3.2 for a more detailed breakdown).

The chosen mechanism to drive the ballasting piston was a translating screw jack, which utilizes a worm gear drive. In this configuration, the worm wheel serves as the drive nut; as it rotates, it translates the lead screw along its linear axis to move the piston head.

This layout is a standard mechanism for lifting heavy loads and is used to convert the rotational torque of a motors to linear motion[39]. Critically, the worm gear ensures self-locking, preventing the piston from being be back-driven by the the load (water). This is extremely important, since it means we don't have to use electrical power to maintain a constant piston position while at steady state, thereby significantly improving electrical efficiency of the AUV during measurement; allowing for a longer battery life and deployment. A diagram of a standard translating screw jack driven by a worm gear is shown in Figure 3.1 below:

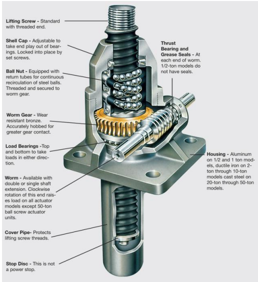

Figure 3.1: Diagram Showing all the Working Parts of a Translating Screw Jack

3.2 Requirement Analysis

Table 3.1 shows the list of functional (FR) and user requirements(UR) of the system:

Requirement ID	Description
UR01	Actuator piston must be waterproof
UR02	Actuator must be able to make the system sink or float
FR01	Actuator must work up to the specified depth
FR02	Actuator must be fast enough to allow for good control
FR03	Actuator must not stress the power subsystem

Table 3.1: Table Showing all Requirements

From Table 3.1 above the following corresponding specifications and Specification IDs can be generated:

Requirement	Spec ID	Specification
UR01	SP01	Piston head, which is contact with the water, must be properly sealed
UR02	SP02	Piston must be able to provide up to $19.6N$ of buoyancy force ($\approx 2kgH_2O$)
FR01	SP03	Maximum piston force must be $> 230N$ ($\approx F_{pressure}$ for water at $2m$)
FR02	SP04	Piston must have minimum full stroke period of $18s$ at all rated depths
FR03	SP05	Actuator must be self-locking
FR03	SP06	Maximum current draw at $2m < 3A$

Table 3.2: Table Showing the Specifications Along with the Corresponding Requirement they Fulfil

3.2.1 Acceptance Test Procedures

Table 3.3: Table Showing the List of Acceptance Test Procedures and the Corresponding Requirement and Specification They Test

ATP ID	Tests	Description
ATP01	UR01:SP01	Apply a wet cloth on top of the piston head and place a piece of paper at the bottom. Move the piston up and down for 10 minutes. Pass if the piece of paper is completely dry after 10 minutes.

Continued on next page...

Continuation of Table 3.3		
ATP ID	**Tests**	**Description**
ATP02	UR02:SP02	Measure the change in volume from the bottom position of the piston to the top position using callipers to measure the length and radius, where $\Delta V = \pi r^2 \Delta l$. Pass if $\Delta V > 2000cm^3$
ATP03	FR01:SP03	Place cylinder on a scale and measure Δm_{scale}(change on the scale reading at full power vs when the motor is off) when driving the motor at full power. Pass if the $\Delta m_{scale} > 23kg$
ATP04	FR02:SP04	Place equivalent weight on the piston head to the force exerted by water pressure at $2m$ ($\approx 23kg$ needed). Pass if $T_{stroke} < 18s$ for both retracting and extending
ATP05	FR03:SP05	With the motor off and the piston extended, add a $5kg$ weight on the piston head. Pass if the piston is not pushed back in after 10 minutes.
ATP06	FR03:SP06	Add the full load weight and drive piston at rated speed. Measure current draw using DC power supply readings. Pass if $I_{motor} < 3A$. Performed concurrently with ATP03.

3.3 Design Decisions

This section delves deeper into some of the key design decisions evaluated when developing the subsystem including the piston cylinder dimensions, choice of motor, gearbox and screw design, as well as the stand used to guide the piston. For more information on the piston head used, see 10.2

3.3.1 Piston Dimensions

Prototype Design

The first step in the design of the actuation system was to decide on the dimensions for the actuator piston. The volume of water that the piston needs to be able to ballast, and the volume of the piston cylinder itself, depends on the required maximum buoyancy change. Alternatively, this buoyancy change can be looked at as a maximum desired change in effective mass of the AUV due to buoyancy. Using Archimedes principle, to describe the maximum buoyancy force provided by the piston:

$$F_{B_{piston}} = \rho_{water} g V_{cylinder} = \Delta m_{eff} g$$

The Δm_{eff} chosen was $2kg$. This value was decided upon in conjunction with the housing and control subsystem designer. Since, initial estimates for the mass of the AUV also sat around $2kg$, more than this would be unnecessary as the geometry of the AUV itself adds additional buoyancy proportional to it's volume. Using a large range of buoyancy positions, however does make the system easily controllable in line with FR02. Thus, substituting $F_B = 2 \times 9.81$ into the equation above:

$$2(9.81) = (997)(9.81)V_{cylinder}$$

$$V_{cylinder} = 0.00201m^3$$

Choosing a cylindrical shape for the piston to allow for easier O-ring sealing and even heat expansion:

$$V_{cylinder} = 0.00201 = \pi r^2 l_{cylinder}$$

Assuming a cylinder radius of $6cm$ and solving for the required length gives:

$$l_{cylinder} = 18cm$$

For more information on the trade-offs associated with our choice of radius see appendix section 10.1.

Final Product Design Considerations

Repeating a similar process for $100m$ depth, the following dimensions are recommended: $r = 0.03m$, $l_{cylinder} = 0.71m$. These dimensions were chosen, since there is significantly higher power draw and force on the piston at lower depths due to the extreme hydrostatic pressure. A reduction in the radius of the cylinder is proposed to counteract this. This would however, make the AUV significantly longer, which would require changes to the housing design.

3.3.2 Motor Selection

Prototype Design

The motor specifications were calculated as follows. For the maximum force required the following formula was used:

$$F_{piston} = \rho_{water} g h_{max} \pi r^2$$

Substituting $997kg/m3$ for the density of water, 9.81 for g, $0.06m$ for r and $2m$ for the maximum depth h_{max} gives us:

$$F_{piston} = 221.23N$$

Next the mechanical power required from the motor is given by:

$$P_{motor} = \frac{Fv}{\epsilon_{mech}}$$

Where F is the force exerted by the piston and v is the speed and ϵ_{mech} is the mechanical efficiency of the actuator. For a cylinder length of $18cm$ and a stroke period of $18s$ speed is given by $v = \frac{l}{T_{stroke}} = 0.01m/s$, whilst the mechanical efficiency for translating screw jacks is usually low, between 35% and 45% due to their self-locking nature. Substituting $F = 221.23N$, $v = 0.01m/s$ and $\epsilon_{mech} = 0.35$:

$$P_{motor} = 9.48W$$

The 3 motors found that match these requirements, whilst also being within the budget set by the team for the motor ($< R400$) are compared in Table 3.4 below:

Name	Rated Voltage (V)	Rated Power (W)	Price (ZAR)
RSDC	24	36.6	385.24
RS PRO Geared DC Motor	$3 - 7.2$	19.8	158.83
DYD3430D024	$12 - 24$	$200W$	298.30

Table 3.4: Table Showing the Differences Between Motor Options

Ultimately, the **RS PRO Geared DC Motor** was chosen here due to it being the cheapest while offering the most desirable input voltage range. This is because the battery we are using has a voltage range of $9 - 12V$, meaning both other motors would need a boost converter, whilst the chosen motor requires a buck converter. Generally speaking, step-down (buck) converters are more efficient than step-up (boost) converters[40], which will allow for slightly less power draw. Furthermore, the DYD3430D024 and RSDC are both over-specced for the application and thus run at their maximum efficiency at much higher power draws, with the DYD3430D024 in particular only having an efficiency of 8% at a $20W$ draw [41].

Finally, the estimated current draw of our RS PRO motor, assuming we operate near our maximum efficiency point (typically ≈ 85% for brushed DC motors [42]) and that the motor receives $7.2V$ is:

$$I = \frac{P}{V \times \epsilon_{electrical}} = \frac{9.48}{(7.2)(0.85)} = 1.55A$$

which is theoretically well below our current draw specification of $< 3A$

Note: The assumption that we are operating near our maximum efficiency speed will late be accounted for in the gearbox design section.

Final Product Design Considerations

For the $100m$ depth design, using the dimensions outlined for the $100m$ design in 3.3.1, and the same speed specification as for our $2m$ design, the required motor power of $280W$. This means a much more powerful motor is required, with a possible motor that could be used being the 90ZY24-300, available for $R3417.68$ at Mantech. This power requirement can be reduced if the speed specifications are relaxed however.

3.3.3 Screw Driven Linear Actuator Design

Prototype Design

Screw:

The screw used was 3-D printed to save on cost and weight. The diameter of the screw required to prevent buckling (primary failure mode for screw jacks), was then determined according to the formula:

$$d_{required} = \sqrt{\frac{4F_{axial}}{\pi \sigma_{PLA}}}$$

Here $F_{axial} = 221.23N$, as determined in 3.3.2 and σ_{PLA} is the tensile strength of PLA, which is typically $60MPa$ [43], substituting these into the formula yields:

$$d_{required} = 4mm$$

For a greater safety margin however, $16mm$ diameter screw was used, since our screw would not be able to use 100% infill due to printing times, which is what the σ_{PLA} value is based on.

The screw length was also designed to be $22cm$, to allow roughly $4cm$ of space from the top of the guide stand for our gearbox, whilst still allowing for our $18cm$ piston ballast range.

Lastly, for lead screws trapezoidal threads are required, since they allow for better durability and self-locking behaviour which is desired for lead screws.

Worm gear Drive:

In a translating screw jack the primary mechanism used to translate rotational motion into linear motion, is the use of a worm wheel as a nut revolving around a rotationally locked screw, as seen in Figure 3.1. Both the worm gear and wheel nut are then prevented from translating either horizontally or vertically respectively by thrust bearings, which lock the worm gear drive in place whilst providing as little resistance to their rotation as possible. This forces the screw to translate through the worm wheel when it is driven by the worm gear.

The primary consideration for weather a worm gear is self-locking or not, meaning whether it can be back-driven by the output, is whether the friction angle (ϕ) is greater than the lead angle(λ) or not, where ϕ can be obtained from the kinetic friction co-efficient (μ) according to: $\phi = \arctan(\mu)$. Thus for our PLA 3-D printed worm gear and screw with $\mu_k \approx 0.3$ [44], the requirements for our worm drive to be self-locking are:

$$\lambda < \arctan(\mu_{PLA})$$

$$\lambda < 17^\circ$$

The efficiency of the worm gear drive is then given by:

$\eta = \frac{\tan(\lambda)}{\tan(\lambda+\phi)} \times 100\%$, where $\eta < 50\%$ is required for self-locking behaviour.

For our design we chose a 10°, which gives us an efficiency of 34.6%. This was done to allow for a greater safety margin whilst maintaining some efficiency, as gradual wear will result in changes in the friction co-efficient between the 2 surfaces. The worm gear drive, as well as all other gears used in this design were generated, using the GF Gear Generator toolbox in Autodesk Fusion and an identical trapezoidal thread to the screw was added to the inside of the worm wheel to form the nut.

Gear Box:

In order to limit peak power and current consumption , the choice was made to operate peak motor efficiency near the slowest allowable speed, as outline at the end of the motor selection section. Limiting peak current draw is vital, since veroboards typically only supports a maximum current draw of $2-3A$. The peak efficiency speed of the piston was therefore chosen to be $v = 1.5cm/s$, slightly above the $1cm/s$ minimum.

Since no efficiency graphs were provided by the manufacturer, the peak efficiency speed had to be estimated from the rated no-load speed of $22356rpm$. For brushed DC motors this is typically between $70\% - 75\%$ of no-load speed[45]. Assuming peak efficiency at 72.5%, we get a peak efficiency point of $\omega_{motor} = 16767rpm$.

To determine the transmission ratio of the gears required, we must relate the speed rating of the piston to a speed rating of the worm wheel. From this the overall reduction ratio of the gear box can be calculated. The worm wheel speed is calculated using:

$$\omega_{wheel_{RPM}} = \frac{v_{piston} \times 60}{p} = 225rpm$$

Substituting in $4mm$ for the screw pitch used and $1.5cm/s$ for the piston speed gives us $\omega_{wheel_{RPM}} = 225rpm$. This along with the calculated peak efficiency speed can be used to get the transmission ratio:

$$TR = \frac{\omega_{motor(peakefficiency)}}{\omega_{wheel}} = \frac{N_{wheel}N_{spur_2},}{N_{spur_1}} = 72$$

where N_{wheel}, N_{spur_1} and N_{spur_2} are the number of teeth on the worm wheel and the primary and secondary spur gears respectively.

This transmission ratio was achieved using an initial $4:1$ reduction from a pair of spur gears, with 10 teeth om the primary gear and 40 on the secondary. This was then mechanically connected to worm gear drive via a shaft, which provide a further $18:1$ speed reduction as seen in Figure 3.2:

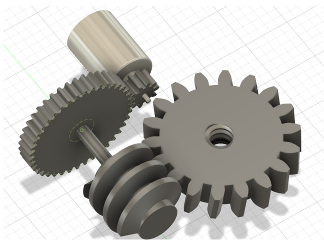

Figure 3.2: 3-D Render of the Final Gear Box and its Connection to the Motor

For the spur gears a module of $1.5mm$ was used whilst for the worm wheel a module of $2mm$ was used resulting in failure large gears, since $d = mN$, where d is diameter, m is the module and N is the number of teeth. Since the most common failure mode for 3-D printed gears is shearing at the teeth, the larger teeth were deemed necessary, because larger gears have more material at the teeth, thereby mitigating this risk.

Final Product Design Considerations

Screw

For the $100m$ design the same dimensions can be used for the screw, however, you would need to change the material to a stronger substance. Steel screws would be ideal due to their increased durability and strength for long deployments, whilst being widely available and cheap. For steel, with a typical tensile strength of $500MPa$, the minimum screw diameter at $100m$ is $4.7mm$, assuming a piston radius of $3cm$. This is well below the $16mm$ diameter of the trapezoidal screw used.

Gears

For the final product, it is recommended to use a tin-bronze alloy for the worm gear drive. This is standard practice for worm gears [46], due the alloy's exceptional durability. This is the recommended, since the threads of worm gears typically wear-down over time and thus need to be reinforced

The friction coefficient of lubricated tin-bronze is typically ≈ 0.1 [46], meaning that the lead angle, $\lambda < 5.7°$, is required for this application. Here a lead angle of $5°$ could be chosen for maximum efficiency, since we don't have to worry as much about friction coefficient changes over time. This give us an efficiency of $\eta = 46.3\%$.

For the spur gears, steel gears would be recommended with the gear ratio needing to be adjusted to the specific motor used following the same process as the prototype.

3.3.4 Guide Stand Design

Prototype Design

In order for a jack screw mechanism to work, the screw must be prevented from rotating, which forces it to translate up or down when the nut is rotated. In our design this is achieved using a guide stand with a square opening for the screw to move in. The bottom of the screw was then fitted with a matching square piece that prevents it from rotating as seen in Figure 3.3.

The top of the guide stand was then also designed to provide a bracket for the motors, as well as mounting points for the bearing brackets, which our shaft will run trough. Space for the wiring of the motor and position sensor was also left in the platform. Importantly, the guide cylinder was also designed to integrate into the main housing. The intended orientation was for the piston to face downwards and be secured it into the main body of the housing via the mounting holes. A labelled Diagram is provided below:

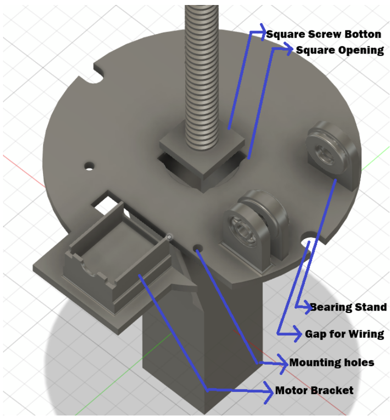

Figure 3.3: Image Showing the Guide Stand and Matching Screw Piece

Final Design Considerations

The final design of the guide stand would not need to change significantly, since the guide stand itself does not experience any significant forces, however the platform and motor bracket, would of course have to be resized according to the size of motor and gears used.

3.4 Testing and Implementation

The system was built and assembled according to the Fusion files in Github link.

Before assembly, the system was simulated using the dynamic joints feature in Fusion assemblies, which allows us to simulate the kinetics of the system. A MATLAB program estimating the different forces and pressures on the system was then also used to assist in the design, however a full stress and force analysis of the whole system could not be conducted due to time constraints. The maximum tensile and compressive stress for the piston head was found to be $0.96MPa$, which is well below the $60MPa$ maximum stress of PLA [43], whilst the screw stress was accounted for during the design phase.

After the system was validated in simulation, the design was then 3-D printed and assembled as seen in Figure 3.4 and Figure 3.5:

Figure 3.4: Image Showing the Actual Final Assembly

Figure 3.5: Image Showing the 3-D printed Piston head and Lead Screw Head

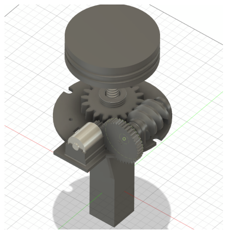

Figure 3.6: Image Showing the Final Assembly in Fusion

3.4.1 Testing Results and Evaluation

Below are the results of the ATPs described in 3.3:

Acceptance Test Procedure ID	Result (Pass/Fail)
ATP01	Pass
ATP02	Pass
ATP03	Fail
ATP04	Fail
ATP05	Pass
ATP06	Fail

Table 3.5: Table Showing the Results of our Acceptance Tests

Overall, 50% of ATPs where passed, with the system passing the waterproofing, self-locking and volume tests demonstrating significant promise. At no load conditions the system also demonstrated the ability to translate the piston up and down at the desired speed.

For all 3 failed tests, however there was a common cause of failure. Since, all these tests were performed at full load, the reason for failure was buckling and snapping of the lead screw, with an image of this shown in 10.3 of the appendix.

The reason for this was that the infill was far too low, as the simulations assumed a solid screw (or 100%). In practice, however, due to the time limitations and high demand for printing time, the infill had to be reduced to 20%, whilst the extra diameter allocation of the screw in 3.3.3 was not sufficient to counteract this. Determining the precise second moment of area for the different infill pattern and percentage required, would have been challenging and ultimately too time consuming. Thus, a trial and error approach was intended to get the precise 3-D printing parameters, with the constraints in place not allowing for further testing with different infill patterns and percentages.

For ATP06 (current draw), the test was unable to be performed thoroughly due to the mechanical limitations of the system. However, the peak current measured before mechanical failure and during all other tests was indeed observed to be $< 3A$, as monitored by the power subsystem designer during the tests. Since, we were unable to monitor this throughout the whole test it was seen as a fail however.

3.5 Recommendations

To rectify the problem of the screw buckling it is recommended, to use a higher infill percentage on your 3-D printer, preferably close to 100% to ensure mechanical integrity. This can also simulated in a FEA (finite element analysis) software, such as ANSYS to find the optimal infill percentage. Additionally, it is recommended to switch from using the standard grid infill pattern to a gyroid pattern for the screw since, as this has the greatest load capacity[47].

Furthermore, it is recommended to find additional waterproofing methods, such as waterproofing paint or coating with epoxy, if you intend to deploy the system for any prolonged period of time using 3-D printed parts. This is because even with waterproof filament types such as PETG, the 3-D printing process itself introduces tiny gaps through which water can seep in after prolonged exposure. Since this design was treated primarily as a proof of concept however, this was not factored in to our waterproofing test (only tested for 10 minutes).

3.6 Conclusion

In conclusion, the final design and implementation of the control actuator subsystem successfully demonstrated a proof of concept for future designs. Although, some structural weaknesses were found in the lead screw during testing, this can easily be rectified using the recommendations outlined. All around the system was found to be functional and suitable as a baseline design for future designs, whilst still leaving some room for improvement.

Chapter 4

Controller Subsystem

Prepared By: Phila Haanyama HNYPHI001

4.1 Introduction

The chosen solution of a buoyancy-controlled autonomous underwater vehicle (AUV) regulates depth using a piston-based displacement system. Increasing internal water volume increases vehicle density, causing descent, while expelling water reduces density and enables ascent.

The depth control subsystem ensures accurate and stable tracking of a commanded depth without operator intervention. It is a critical subsystem, as depth accuracy directly affects the validity of phytoplankton measurements.

The subsystem operates across three domains: depth sensing, control, and actuator interfacing. The actuator consists of a DC motor-driven screw jack translating rotational motion into piston displacement, resulting in coupled electrical, mechanical, and hydrodynamic dynamics.

4.2 User Requirements

User requirements define the required system behaviour and are derived from the project brief. These requirements are mapped to functional requirements and design specifications through the traceability matrix to ensure full design accountability.

ID	Requirement Description
UR-1	Autonomous depth tracking without human intervention.
UR-2	Stable depth control with no sustained oscillations.
UR-3	Reach setpoint within physical motion constraints.
UR-4	Surface recalibration before each dive.
UR-5	Sensor and actuator communication via selected interfaces.
UR-6	Protection against mechanical/electrical limits.
UR-7	Real-time operation on Raspberry Pi Pico.

Table 4.1: User Requirements

User Requirement	Functional Requirement	Design Specification
UR-1	**FR-1**: Closed-loop depth control with integral action.	**SP-1**: SS error $\leq 0.05\,\text{m}$.
UR-2	**FR-2**:Stability margins (PM $\geq 45°$).	**SP-2**: No oscillation.
UR-3	**FR-3**: Acceptable settling time.	**SP-3**: $\leq 120\,\text{s}$ rise time for a 1 m step.
UR-4	**FR-4**: Surface calibration routine.	**SP-4**: Zeroed depth at startup.
UR-5	**FR-5**: I^2C + PWM interface implementation.	**SP-5**: I^2C at 400 kHz; 20 kHz PWM.
UR-6	**FR-6**: Voltage + stroke limiting.	**SP-6**: Hardware/software protection.
UR-7	**FR-7**: 200 Hz control loop execution.	**SP-7**: ≤ 5 ms loop time.

Table 4.2: Traceability Matrix

4.3 Requirement Analysis

This section translates user and functional requirements into quantitative engineering constraints that guide the control system design.

4.3.1 Depth Range and Sensor Rating

The system is designed for a 0-2 m operating depth range which is approximately 0.2 bar of guage pressure.

The selected depth sensor must therefore :

- operate accurately over this pressure range,
- provide centimetre-scale resolution,
- tolerate transient pressure disturbances (e.g., wave motion),
- and maintain robustness under brief over-depth conditions.

Additionally, a safety margin above the maximum operating pressure is required to accommodate environmental uncertainty.

4.3.2 Control Loop Timing

To meet the performance requirements of the system, a feedback control architecture is required. A cascaded control structure is assumed for the purposes of requirement derivation, as it is widely used in electromechanical DC motor systems where separating velocity and position control loops improves disturbance rejection and simplifies tuning. This structure is consistently applied in practical implementations reported by Elhamid, A.S, where inner velocity regulation is used to linearise actuator dynamics [48], and by Ibrahim et al., who demonstrate improved stability and tracking performance through outer-loop position control built on a fast inner loop [49]. Its justification is presented in Section 4.4.

To ensure stable discretised implementation, the sampling frequency must significantly exceed system bandwidth. While Nyquist requires only 2x bandwidth [50], practical control systems require ≥10x to preserve phase margin after discretisation [51].

The controller must therefore operate at a sufficiently high sampling rate to capture inner-loop dynamics, which dominate system speed.

4.3.3 Cascade Bandwidth Selection

For stable cascade operation, the inner loop must be significantly faster than the outer loop, ensuring it behaves as an approximately instantaneous actuator.

A minimum separation of 5:1 is required to avoid loop interaction and preserve independent tuning [52].

4.3.4 Steady-State Error

The system must maintain a constant depth without steady-state offset.

This requires at least one integrator in the closed-loop system, either in the controller or plant, to ensure zero steady-state error to step inputs.

4.4 Design Decisions

This section maps requirements in Section 4.3 to design choices and ensures traceability.

4.4.1 Depth Sensor Selection

The depth sensing solution must satisfy FR-1 and FR-4, while meeting SP-1.

Criteria	**MS5837-02A** [53]	**MS5837-30BA** [54]	**Requirement Link**
Pressure Range	0–2 bar (≈ 20 m)	0–30 bar (≈ 300 m)	Section 4.3
Resolution (0–2 m)	High	Lower	SP-1
Interface	I^2C	I^2C	FR-5
Calibration Support	Yes	Yes	FR-4

Table 4.3: Depth Sensor Comparison Table

Both sensors satisfy interface and calibration requirements. Selection was hence based on resolution over the 0-2 m range. The MS5837-02A was selected as superior resolution directly improves depth tracking accuracy. The MS5837-30BA variant is over-specified for this application as seen in Table

4.3 however it would be justified for deployment in the Antarctic ocean where the operating range is ≈50-100 m.

4.4.2 Microcontroller Selection

Board	Clock	SRAM	I2C	HW PWM	Price (ZAR)
Raspberry Pi Pico [55]	133 MHz	264 KB	2×	2 channels	∼R158
ESP32 Dev Board [56]	240 MHz	520 KB	1×	Limited under MicroPython	∼R178
Arduino Nano 33 IoT [57]	48 MHz	32 KB	1×	Software only	∼R493
Arduino Uno [58]	16 MHz	2 KB	1×	3 pins	∼R136

Table 4.4: Comparison of candidate microcontroller boards

The Raspberry Pi Pico was selected due to:

- hardware PWM stability,
- sufficient memory for 200 Hz loop execution,
- deterministic real-time behaviour,
- low cost and system simplicity

which can be seen in Table 4.4.

ESP32 was rejected due to non-deterministic PWM under MicroPython and unnecessary wireless overhead. Arduino platforms were rejected due to memory and timing constraints.

For a scaled research vehicle, a two-tier architecture is common: an STM32H7 [59] (or equivalent industrial Cortex-M) handles the real-time control loop, while a higher-level SBC (e.g CM4 Industrial [60]) handles mission management, data logging, and communication.

4.4.3 Piston Position Sensor Selection

Criteria	Linear Potentiometer [61]	Multi-turn Encoder [62]	AS5600 [63]
Measurement Type	Linear (direct)	Absolute multi-turn	Angular (rotary)
Waterproofing	Poor	Moderate	Easy
Complexity	High	Moderate	Simple
Resolution	Moderate	High	High
Cost	R4 030,99	R3 397,84	R325,68
Interface	Analog	Digital	I^2C (FR-5)

Table 4.5: Position Sensor Comparison Table

Based on Table 4.5, the AS5600 was selected due to:

- contactless operation (improved reliability),

- sufficient resolution (12-bit),
- simple I^2C integration,
- reduced mechanical complexity.

The AS5600 is a bare PCB magnetic encoder with no environmental sealing. For deep deployment, the motor assembly itself needs to be either in a pressure-compensated oil-filled housing or fully sealed. Hence a better sensor for that operation would be the RLS AksIM-2 [64].

4.4.4 Controller Architecture Selection

Two control strategies were considered: a single-loop PID controller and a cascaded control architecture with separate inner (velocity) and outer (position) loops.

Criteria	Single-loop PID	Cascaded Control
Disturbance Rejection	Poor	Good
Tuning	Difficult	Structured
Stability Margins (SP-2)	Harder to guarantee	Easier to enforce
Meets FR-2 (stability)	Risky	Reliable
Meets FR-3 (response time)	Limited	Flexible tuning

Table 4.6: Control Architecture Comparison Table

As can be seen in Table 4.6, the cascaded architecture provides improved disturbance rejection and independent loop tuning allowing for separation of actuator and system dynamics. The cascaded architecture can be seen in Figure 4.1

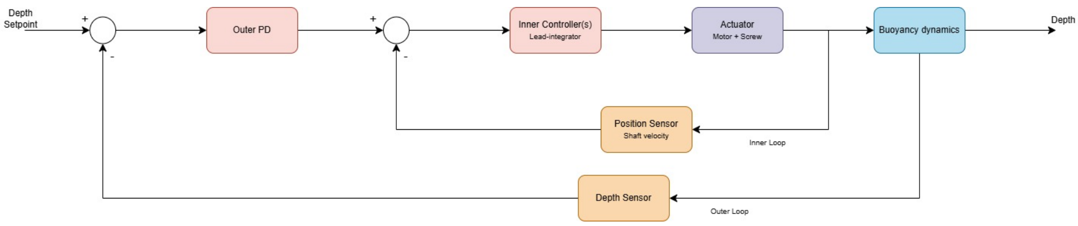

Figure 4.1: Cascaded Depth Control Block Diagram

4.5 Design and Simulation

4.5.1 Plant Modelling

The objective of this section is to demonstrate that the implemented design satisfies the performance and stability requirements defined in Section 4.3

The actuator was modelled as an electromechanical system using the standard armature-controlled DC motor transfer function [65] consisting of:

- DC motor electrical dynamics,

- rotational inertia and damping,
- screw jack conversion K_s.

$$G_{position}(s) = \frac{K_t K_s}{[(L_s + R)(J_s + b) + K_t K_e]s} \tag{4.1}$$

with motor parameters: R = 0.714 Ω, L = 0.001 H, K_t = 0.002 Nm/A, J = 5×10^{-6} $kg \cdot m^2$, b = 4.49×10^{-6} $Nm \cdot s/rad$. The screw gain was calculated from the physical geometry (lead angle 10°, diameter 25 mm, Appendix 11.8.1) and found to be $K_s = 0.002204$ m/rad (See Figure 11.2).

Using the system parameters, plant validation confirmed (See Figure 11.1):

- $\tau_{electrical}$ = 1.4 ms,
- $\tau_{mechanical}$ = 1.1 s.

Since the electrical dynamics are much faster (800:1), the model was reduced to second order without loss of accuracy (See Figure 11.3)[66].

4.5.2 Inner Velocity Loop Design

The inner loop regulates shaft velocity and ensures stability and disturbance rejection.

The resulting lead compensator was designed interactively using MATLAB's sisotool [67] as seen in

$$C_{inner}(s) = 937.5 \cdot \frac{s + 4}{s(s + 50)} \tag{4.2}$$

(See Figure 11.4, Appendix 11.8.4)

Key features:

- Integrator: zero steady-state velocity error
- Zero at -4: phase compensation
- Pole at -50: noise attenuation [68]

(See Figure 11.7)

Performance:

- Phase margin: 61.53 °
- Gain margin: ∞
- Bandwidth: 21.53 rad/s

(See Figures 11.5 and 11.6)

4.5.3 Outer Loop Control

The outer loop regulates depth by generating a velocity reference for the inner loop based on depth error and depth rate feedback.

The control law is defined as:

$$v_{ref} = K_{outer}(d_{ref} - d) - K_D\dot{d} \tag{4.3}$$

This structure was chosen due to the non-linear, slow buoyancy dynamics not captured in the MATLAB model. The derivative action provides damping and prevents overshoot due to buoyancy momentum [48].

Depth rate is low-pass filtered to prevent noise amplification.

Outer Loop Gain Tuning

MATLAB models are insufficient for outer-loop tuning as it does not contain buoyancy dynamics.

For this reason a separate physics simulation, which can be seen in Figure 11.13 was used:

$$\ddot{d} = BUOY\_GAIN(x_{shaft} - x_{equilibrium}) - DRAG\dot{d} \tag{4.4}$$

(See Figures: 11.8 and 11.9) where:

- x_{shaft} is piston position
- $x_{equilibrium}$ is the neutral buoyancy equilibrium position of the piston
- $BUOY\_GAIN = \frac{\rho A_{piston} g}{m_{vehicle}}$
- $DRAG = 5.0\ s^{-1}$

This model includes:

- buoyancy force coupling,
- drag ($\zeta \approx 2.5$),
- 3 kg vehicle mass,
- sensor noise ($\sigma = 1$ mm)

The final gains were found to be $K_{outer} = 0.1$ and $K_D = 4.3$ (See Figure 11.14). This achieved monotonic convergence with zero overshoot.

4.5.4 Sensitivity Analysis

A sensitivity analysis was performed to evaluate the robustness to disturbances and measurement noise. The robustness of the closed-loop system was evaluated using the sensitivity function [69]:

$$S(s) = \frac{1}{1 + L(s)}, T(s) = \frac{L(s)}{1 + L(s)} \tag{4.5}$$

Peak |S| was found to be 0.87 dB (the standard robustness 6 dB requirement [70]). Figure 11.10 shows the complementary sensitivity peaks at 0 dB at DC and rolls off above the outer loop bandwidth, confirming high-frequency encoder noise is attenuated before reaching the motor command (See Figure 11.11).

4.5.5 Discretisation and Digital Implementation

Since the controller is implemented on a Raspberry Pi Pico microcontroller, the continuous-time compensators must be converted into discrete form.

A sampling frequency of 200 Hz ($T_s = 0.005$ s) was selected to satisfy both the Nyquist criterion and practical control stability requirements, ensuring sufficient phase margin preservation relative to the inner-loop bandwidth.

The Tustin (bilinear) approximation [71] was used to preserve frequency response.

The resulting discrete inner controller is:

$$u[k] = 1.778u[k-1] - 0.778u[k-2] + 2.104e[k] + 0.042[k-1] - 2.063[k-2] \tag{4.6}$$

The continuous and discrete responses are nearly identical, as can be seen in 11.12 , with PM reducing from 61.53 ° → 50.69 °

4.6 Testing and Validation

All acceptance test procedures (ATPs) were validated using a Python Software-in-the-Loop (SIL) simulation.

The SIL simulation is a high-fidelity validation environment that executes the exact MicroPython control difference equations deployed on the Raspberry Pi Pico, rather than an abstract or linearised controller model. These discrete equations are evaluated against a numerically integrated buoyancy-driven plant model, enabling realistic pre-deployment verification of closed-loop behaviour. Using the model from Section 4.5.3, at each 5 ms timestep (200 Hz), the SIL executes:

- Buoyancy plant update (numerical integration)
- Depth measurement with noise injection
- Depth-rate filtering (first-order low-pass)
- Outer-loop PD update
- Inner-loop update (Pico firmware coefficients)
- Physical constraints (± 2.142 V, stroke limits, velocity limits (Appendix 11.8.3))

As the SIL executes identical code control and parameters as the embedded implementation, it provides a valid pre-hardware verification of system behaviour.

Four test scenarios were evaluated over a 1 m step input:

- **S1:** Clean step (noise only)
- **S2:** Load disturbance at t = 60 s
- **S3:** Sensor noise only (σ = 1 mm)
- **S4:** Combined noise and disturbance

4.6.1 Acceptance Test Procedures

ATP	Spec	Test & Evidence	Result
ATP-1	200 Hz timing	Full loop execution. SIL must show no overruns (<1 ms/step).	Pass
ATP-2	Overcurrent & stroke limit	Max step input; voltage output clamped at 2.142 V clamp and shaft limit constrained to 0-162 mm. See Fig. 11.15.	Pass
ATP-3	SS error < 50 mm	1 m step input: 2.6 mm (clean), 3.1 mm (noise); 70–73 mm under disturbance. See Figs. 11.15 and 11.16.	Pass (Limited.)
ATP-4	Stability	MATLAB margins and SIL response: all PM/GM above spec, SIL response shows no oscillation under nominal and noise conditions. See Fig. 11.16.	Pass
ATP-5	90% rise time < 120 s	1 m step: 90 % of target depth reached at 87 s (consistent with 14.73 mm/s physical velocity limit). See Fig. 11.17.	Pass
ATP-6	Disturbance rejection	Equivalent voltage disturbance of 0.64 V (30% of V SAFE MAX) applied at t = 150 s; System remains stable but 70 mm offset observed due to PD structure. See Figs. 11.16 and 11.18.	Pass (Limited.)
ATP-7	Noise rejection	σ = 1 mm MS5837 noise applied; Bounded response with SS error 2.0 mm. Brief velocity reference spikes of up to 21 mm/s observed but not propogated to physical motion. See Fig. 11.17 and 11.18.	Pass

Table 4.7: Acceptance Test Procedures and Results

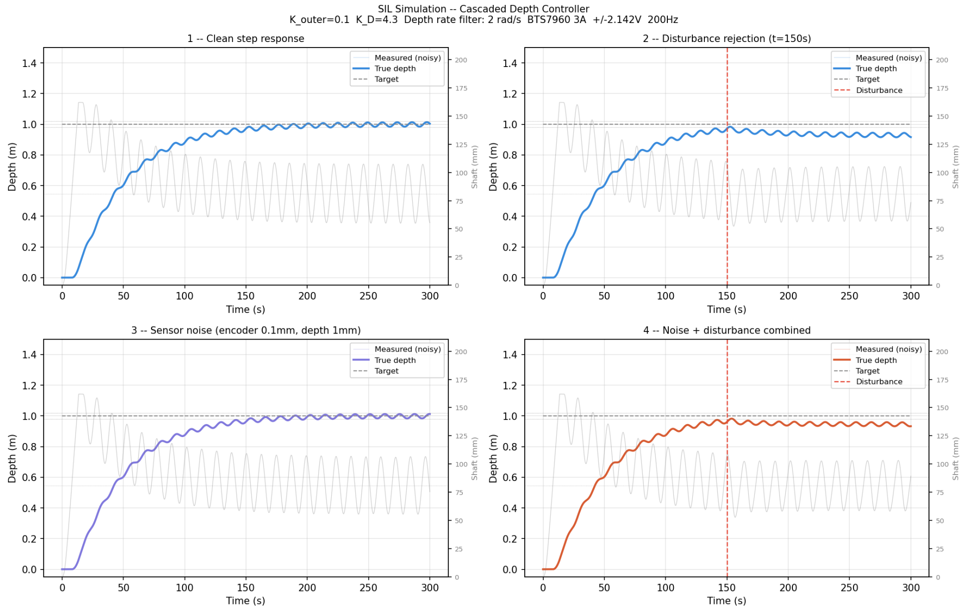

Figure 4.2: SIL Results

Explanation of Qualified Results

Two ATPs exhibit correct operation under nominal conditions but show known limitations under specific stress cases.

ATP-3 and ATP-6 (Steady-state disturbance error): Under a sustained voltage disturbance equivalent to 0.64 V (Scenarios 2 and 4), a steady-state depth error of 70–73 mm is observed, exceeding SP-1. This is a structural property of the PD outer loop: under a constant external load, a non-zero velocity command is required to produce the corrective buoyancy force, which in turn requires a persistent non-zero depth error to sustain it.

This behaviour is not expected under normal operating conditions where the vehicle acts near neutral buoyancy and external forces are small. The limitation is bounded and the system remains stable. It can be eliminated by introducing integral action in the outer loop, as discussed in Section 7.

ATP-7 (Velocity transients under noise and disturbance): In Scenarios 3 and 4, the MS5837 depth noise passes through the derivative path of the outer loop, producing brief velocity reference spikes of up to 21 mm/s, exceeding the 14.73 mm/s physical ceiling. These spikes are transient hence the velocity ceiling clamp in control-step() prevents them from reaching the motor, and the inner loop bandwidth limits further attenuate any residual excitation. The depth response in both scenarios remains stable and monotonic, confirming that the 2 rad/s low-pass filter on the depth rate estimate provides adequate noise rejection for this sensor and operating condition.

4.7 Conclusion and Recommendations

The depth control subsystem was designed and validated for a buoyancy-driven AUV operating up to 2 m depth. A cascaded architecture separates fast actuator dynamics (inner loop) from slow buoyancy dynamics (outer loop), enabling independent controller design.

The inner lead–integrator controller achieves zero steady-state velocity error and maintains a discrete phase margin of 50.69° at 200 Hz, above the 45° requirement. The outer PD controller ($K_{outer} = 0.1$, $K_D = 4.3$) achieves monotonic, zero-overshoot depth tracking across all SIL scenarios. A depth-rate filter (2 rad/s cutoff) is essential to prevent noise amplification.

All ATPs pass under nominal conditions. Two limitations are observed: (i) steady-state error under sustained disturbance due to lack of outer-loop integral action, and (ii) brief velocity reference spikes under combined noise and disturbance. Both are analytically explained and do not affect stability or convergence.

The design is therefore validated for proof-of-concept deployment.

4.7.1 Recommendations

1. Add outer-loop integral action: Introduce PI control to eliminate steady-state error under constant disturbance. Anti-windup must be implemented to prevent integrator accumulation at stroke limits.

2. Verify equilibrium piston position: Confirm neutral buoyancy stroke position experimentally in water. Update STROKE_EQUILIBRIUM in firmware if asymmetric.

3. Validate hardware timing: Confirm 200 Hz loop execution on Pico under real I^2C latency. Worst-case timing dominated by sensor conversion delays (1–2 ms total).

4. Tune noise filter if required: If velocity spikes persist in hardware, reduce depth-rate filter cutoff from 2 rad/s to 1 rad/s. This improves noise rejection with minimal impact on response speed.

Chapter 5

Power Subsystem

Prepared By: Bume Mxenge MXNBUM001

5.1 Introduction

This report develops the power subsystem for an autonomous underwater vehicle intended to support polar research instrumentation in the Southern Ocean. The subsystem must supply electrical energy to the controller, actuator, and research-instrument interfaces while meeting reliability, endurance, space, noise, and cold-environment constraints.

The engineering problem is not only to provide power, but to allow loads with different voltage levels, current demands, operating modes, and noise sensitivities to operate safely from one onboard source. High-current actuator operation must be supported without disturbing low-voltage sensing and control electronics, while inactive loads must be managed to reduce unnecessary energy loss.

The subsystem is therefore considered across four concerns: energy storage, regulated delivery, protection, and load management. These are translated into functional requirements, specifications, and acceptance tests using the load characterisation in Appendix 12.1, then evaluated through architecture development, design justification, sensitivity analysis, and physical testing.

5.2 Requirements Definition and Analysis

5.2.1 User Requirements

ID	Requirement Description
UR01	Provide onboard electrical energy to all AUV subsystems.
UR02	Accommodate the electrical interfaces of the research instruments specified for the mission.
UR03	Support extended deployment periods.
UR04	Remain operable in the cold conditions of the Southern Ocean.

Table 5.1: User Requirements

The user requirements define the system-level expectations for the power subsystem. To translate these into functional requirements and specifications, the expected electrical loads were mapped in

(Appendix add label). The load map captures the supply demands, current ratings, operating modes, and noise sensitivities associated with the AUV subsystems and external loads.

5.2.2 Functional Requirements

ID	Requirement Description
FR01	Provide on-board rechargeable energy storage sized to the system load profile, including margin for environmental degradation.
FR02	Provide regulated supply rails matched to the voltage and current needs of each load.
FR03	Provide a dedicated motor power output for bidirectional actuator operation via a motor driver.
FR04	Protect the energy source and downstream rails against fault conditions.
FR06	Support selective switching of non-essential loads.
FR07	Monitor battery condition to support safe shutdown and low-energy controller decisions.
FR08	Fit within the allocated housing limits while maintaining safe and reliable electrical integration.

Table 5.2: Power Subsystem Functional Requirements

5.2.3 Design Specifications

ID	Design Specification
SP01	Main pack current capacity $\geq 5\,\text{A}$ continuous.
SP02	7.2 V motor rail; 3 A peak operating draw.
SP03	3.3 V rail; ripple $< 50\,\text{mV}_{\text{pp}}$ and 160 mA draw.
SP04	Bidirectional H-bridge motor drive at 20 kHz PWM.
SP05	Load and main switch $< 1\,\mu\text{A}$ OFF.
SP06	Cell-to-cell voltage balance within 0.02 V.
SP07	Physical implementation shall fit within three veroboards, each 6 cm high by 10 cm wide, with 1 cm clearance maintained on each side.

Table 5.3: Power Subsystem Design Specifications

5.2.4 Acceptance Test Procedures

ID	Procedure	Acceptance Condition
ATP01	Charge pack to 12 V. Connect four 10 Ω resistors in parallel, giving 2.5 Ω, across the pack to draw approximately 4.8 A. Measure V_{BAT} with a digital multimeter at no-load and under load.	V_{BAT} drops less than 0.5 V between no-load and 4.8 A load.
ATP02	Power the 3.3 V rail input from a bench supply at 11.1 V. Connect a 22 Ω resistor across the output, giving approximately 150 mA draw. Measure output voltage with a digital multimeter and ripple with an oscilloscope, AC coupled, at the rail output.	Output is 3.3 V; ripple $\leq 50\,\mathrm{mV_{pp}}$.
ATP03	Drive the H-bridge PWM input with a signal generator using a 3.3 V square wave at 20 kHz and 50 % duty cycle. Connect a 2.4 Ω resistor across the bridge outputs. Capture PWM input and bridge output on a 2-channel oscilloscope. Reverse the direction-control input and repeat.	PWM frequency is 20 kHz ±5%; bridge output polarity reverses when the direction input is switched.
ATP04	Command all switches OFF using bench logic signals. Place a digital multimeter, set to the µA range, in series with each switch output and the main switch. Read the OFF-state current.	Current ≤ 1 µA per channel OFF and ≤ 1 µA on main switch OFF.
ATP05	Charge pack to 12 V. Measure each cell voltage with a digital multimeter. Discharge through a 10 Ω resistor down to 10.5 V and measure each cell again.	Maximum cell voltage minus minimum cell voltage ≤ 0.02 V at both measurement points.

Table 5.4: Power Subsystem Acceptance Test Procedures

5.2.5 Requirements Analysis

This section highlights the main requirement tensions and how they are balanced through specifications and acceptance testing.

Capacity vs Deployment Duration

UR01 requires the source to supply all AUV loads, while UR03 requires extended deployment. The tension is that energy demand increases with current draw and deployment time, while peak current must still be available during active operation. FR01 addresses this by requiring the energy source to be sized from the load profile, with capacity scalable to deployment duration. SP01 sets the minimum current-delivery requirement at ≥ 5 A continuous. ATP01 validates this by checking that V_{BAT} does not sag excessively under an approximately 4.8 A load.

Motor Demand vs Stable Low-Voltage Supply

The motor has the highest current demand and is the main noise source, while the low-voltage electronics require a stable rail with limited ripple. The tension is that one shared supply path would couple motor disturbances into sensitive loads. FR02 and FR03 separate regulated load requirements from motor-drive requirements. SP02 defines the motor rail demand, while SP03 limits the 3.3 V rail ripple to $< 50\,\mathrm{mV_{pp}}$. ATP02 validates the sensitive rail, while ATP03 validates the motor drive independently.

Endurance vs Switch Complexity

UR03 makes standby energy loss important because small leakage currents accumulate over long deployments. The tension is that switching inactive loads improves endurance, but adds hardware complexity and possible failure points. FR06 limits switching to non-essential loads, while SP05 sets the OFF-state current target at $< 1\,\mu\mathrm{A}$. ATP04 validates this by measuring switch leakage directly, confirming that the added switching hardware meaningfully reduces standby loss.

5.2.6 Traceability Matrix

UR	Functional Requirement(s)	Design Specification(s)	Verification / ATP
UR01	FR01, FR02, FR03	SP01, SP02, SP03, SP04	ATP01, ATP02, ATP03
UR02	FR02, FR06	SP03, SP05	ATP02, ATP04
UR03	FR01, FR06, FR07	SP01, SP05, SP06	ATP01, ATP04, ATP05
UR04	FR01, FR04, FR07	SP01, SP05, SP06	ATP01, ATP04, ATP05
Implementation constraint	FR08	SP07	Mechanical inspection

Table 5.5: Power Subsystem Requirements Traceability Matrix

5.3 Power Subsystem Architecture

The power subsystem uses a modular architecture made up of four primary modules and one bridging module:

- **Power Source and Protection:** Supplies and manages the main power input to the system.
- **Motor Power Delivery:** Provides the dedicated motor supply and supporting driver power required for controlled actuator operation.
- **Control System Power Delivery:** Supplies the microcontroller and sensor interfaces, with switching to support different operating modes.
- **Research Instrument Power Delivery:** Provides the power and communication support needed to interface with the external research instrument, namely the phytoplankton sensor, and the GNSS module.
- 3.3 V **Regulated Rail:** Acts as a bridging module by deriving the shared low-voltage logic rail from the 11.1 V main bus and supplying it to the control and research instrument sections.

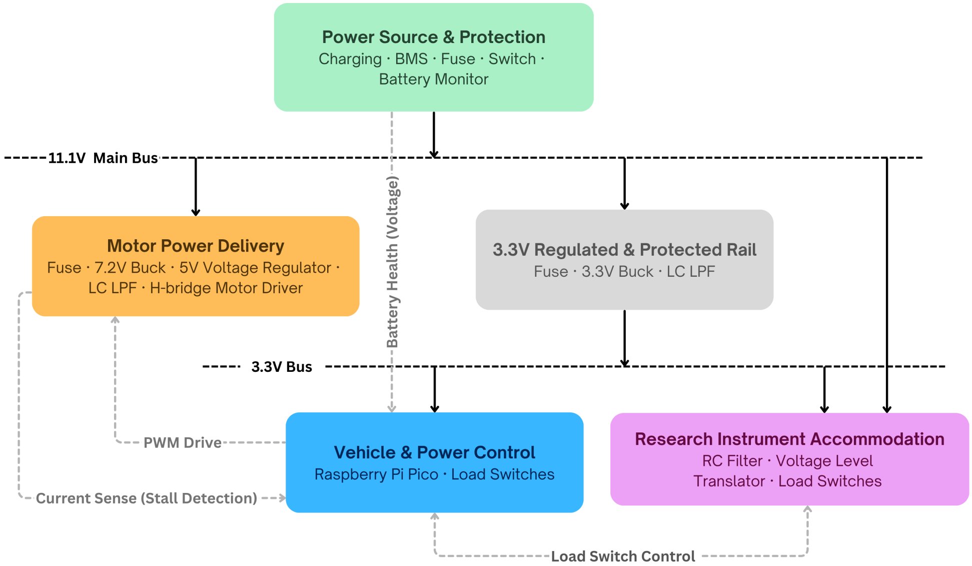

Figure 5.1: Overview of Power Subsystem Architecture

5.4 Design Decisions and Justifications

The power subsystem design was guided by three main constraints: maintaining regulated supply rails as the battery voltage varies, allowing high-current actuator loads and sensitive sensing/control loads to operate simultaneously, and prioritising energy efficiency through both efficient device selection and selective load operation. The design decisions below therefore focus on rail regulation, motor-noise filtering, load switching, and the physical wiring accommodations required for high-current and switching loads.

5.4.1 Energy Source and Battery Topology

18650 Li-ion Cell Selection

Rechargeable 18650 Li-ion cells were selected because they provide a scalable and energy-efficient storage option for the prototype. Each cell provides 9.62 Wh at approximately 214 Wh/kg, allowing capacity and current capability to be increased by adding cells in parallel. This supports longer deployment periods without significantly increasing mass. Supporting cell-level calculations and datasheet values are provided in Appendix 12.2.1.

3S vs 2S Battery Topology

A 3S Li-ion topology was selected over 2S because it gives better voltage headroom, lower battery-side current, and greater stored energy per pack row. For the prototype, it was agreed that the motor would operate at ≤ 3 A. Since the motor rail is 7.2 V, the most power-intensive load is therefore approximately 21.6 W.

Criterion	**2S Li-ion**	**3S Li-ion**	**Design implication**
Nominal voltage	7.4 V	11.1 V	3S provides stronger voltage headroom for downstream regulation.
Pack energy, 1P	19.24 Wh	28.86 Wh	3S stores 50% more energy per series row.
Discharge current capacity, 1P	3.9 A	3.9 A	Both use the same cells, so current capacity per parallel row is the same.
Response to most power-intensive load: 7.2 V at 3 A	4.24 A from battery	2.67 A from battery	2S exceeds the 1P cell current rating; 3S remains within it.
Parallel expansion	+3.9 A per added row	+3.9 A per added row	Both scale current equally, but 3S adds more energy per row.

Table 5.6: Comparison of 2S and 3S Li-ion battery topologies.

The 3S choice therefore trades higher cell count, volume, and BMS complexity for lower current stress, better rail compatibility, and greater usable energy. The full energy, current, scalability, and cold-derating comparison is shown in Appendix 12.2.2.

5.4.2 Motor Noise Control

Load Separation

The motor driver was identified as the main noisy load because it switches high current at approximately 20 kHz PWM. To protect the Pico and sensors from this switching noise, the motor branch was separated from the rest of the system from the battery bus onward.

To further ensure isolation, the design uses a star-ground approach: ground rails of each bus meet at one common battery-side ground point, instead of sharing a long ground wire. This reduces the chance of motor current creating noise on the sensor ground reference.

Ferrite Bead Assessment

A ferrite bead was considered because its mechanism is more attractive than a regular inductor for high-frequency noise. A conventional inductor mainly stores magnetic energy, so it can reflect noise back into the circuit and potentially contribute to ringing. A ferrite bead behaves differently: at low frequencies it acts like a very small inductor, but at higher frequencies magnetic losses increase and its impedance becomes mainly resistive. This means high-frequency noise energy is dissipated as heat rather than only redirected.

However, the motor PWM fundamental is 20 kHz, while the available Murata ferrite bead is intended for noise suppression mainly in the MHz range. At 20 kHz, its impedance is too small to meaningfully attenuate the PWM disturbance. It was therefore rejected as the main filter for motor PWM noise.

LC Filter Selection

A second-order LC filter was selected because its corner frequency can be designed around the motor PWM frequency. A 34 µH power inductor rated at 3 A was used so that it can carry the agreed prototype motor current limit without saturating during normal operation. The target corner frequency was approximately 2 kHz, one decade below the 20 kHz PWM fundamental.

$$C = \frac{1}{4\pi^2 f_c^2 L}$$

$$C = \frac{1}{4\pi^2(2000)^2(34 \times 10^{-6})} \approx 186\,\mu\text{F}$$

A standard 220 µF electrolytic capacitor was selected. With the selected values,

$$f_c = \frac{1}{2\pi\sqrt{LC}} = \frac{1}{2\pi\sqrt{(34 \times 10^{-6})(220 \times 10^{-6})}} \approx 1.84\,\text{kHz}$$

The 220 µF electrolytic capacitor provides bulk energy storage and low impedance near the PWM frequency. The 100 nF ceramic capacitor provides high-frequency bypassing where the electrolytic becomes less effective due to ESR (equivalent series resistance) and ESL (equivalent series inductance). The capacitors are placed close to the H-bridge supply pins so that switching disturbances are diverted locally.

At 20 kHz, the selected filter gives approximately 41.5 dB attenuation. This means only about 0.84% of the switching disturbance passes upstream.

5.4.3 Efficient High-Current Device Selection

On top of being the main noise contributor, the motor path was also the highest power-draw path in the subsystem. The motor driver was therefore selected by comparing current margin, voltage compatibility, conduction loss, and fault protection. The detailed comparison is provided in Appendix 12.3.

The BTS7960 was selected over the L298N for three key reasons:

- **Current margin:** the prototype motor is limited to ≤ 3 A, with an estimated stall current of 11.2 A. The L298N module is rated at only 2 A peak, while the BTS7960 module is rated at 43 A peak.
- **Lower conduction loss:** the L298N uses a bipolar output stage with a large saturation voltage drop. At 2 A, its estimated loss is approximately 9.8 W. The BTS7960 uses MOSFET switching, giving an estimated loss of only 0.29 W at 3 A.
- **Fault protection:** the BTS7960 includes over-voltage, under-voltage, over-current, short-circuit, and over-temperature protection, making it more suitable for the subsystem's highest-power load.

The L298N was therefore rejected because its current rating and saturation losses make it inefficient and thermally unsuitable for the prototype motor rail.

5.5 Final Design and Sensitivity Analysis

5.5.1 Final Design

The final power subsystem is implemented as a protected 3S lithium battery architecture with pack-level, main-bus, and branch-level protection. The architecture separates the high-current motor branch from the low-power 3.3 V control rail and the research-instrument supply. Regulated outputs provide 7.2 V for the motor, 3.3 V for logic and sensors, and 10 V for the phytoplankton sensor. Digitally controlled load switches allow the Pico to isolate the sensor, GNSS, and phytoplankton branches during inactive periods. The complete implementation is shown in Figure 12.2, with the component-level design summary provided in Table 12.12.

For the physical demonstration, only the AUV-related power paths were implemented and tested. The research-interface branch was retained in the final design because it is required for system scalability and usability, but it was not physically implemented because the external research instrument was outside the scope of the demonstration.

The custom load-switch design uses an IRF9530N PMOS and 2N7000 NMOS gate-pull device. Their voltage and current ratings are checked against the respective datasheets in Appendix 12.4.1 [72, 73]. The sensitivity analysis below only evaluates the practical concern: whether the IRF9530N produces an acceptable voltage drop when used on the low-current 3.3 V switched branches.

5.5.2 Load-Switch Sensitivity Analysis

Sensitivity analysis evaluates the custom high-side PMOS load switches used for the 3.3 V GNSS, depth-sensor, and position-sensor branches, as well as the 10 V phytoplankton-sensor branch. The detailed circuit justification, resistor selection, and device-rating checks are given in Appendix **??**. The key uncertainty is the gate-drive margin, because the IRF9530N is not specified as a logic-level PMOS.

The LTspice test checks whether the switched output follows the input rail under the active-load currents identified in the load map. Each load is represented by an equivalent resistance,

$$R_{\text{load}} = \frac{V_{\text{rail}}}{I_{\text{load}}},$$

so that each branch draws its expected active current at its rated supply voltage. Three cases are stepped: the combined depth and position sensors on the 3.3 V rail, the GNSS module on the 3.3 V rail, and the phytoplankton sensor on the 10 V rail. The control input is held at 3.3 V for the on-state test.

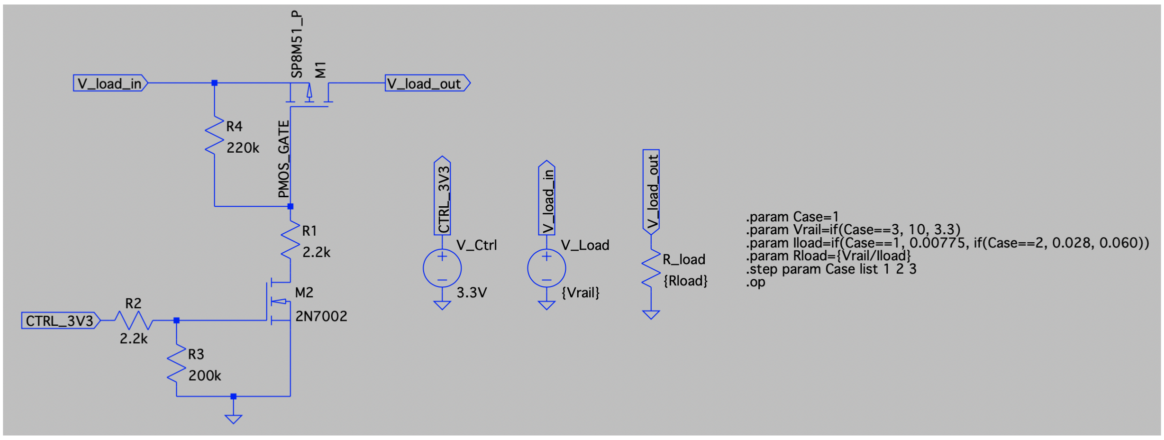

Figure 5.2: LTspice configuration for the high-side load-switch sensitivity analysis.

To keep the result clear, the main plotted quantity is the normalised output voltage, $V_{\text{out}}/V_{\text{in}}$. A value close to 1 shows that the switch passes the rail voltage correctly for each load case. The supporting monitored quantities are $V_{\text{drop}} = V_{\text{in}} - V_{\text{out}}$, $V_{GS,P}$, and I_D, which confirm that the PMOS is being driven on and that the expected load current is supplied.

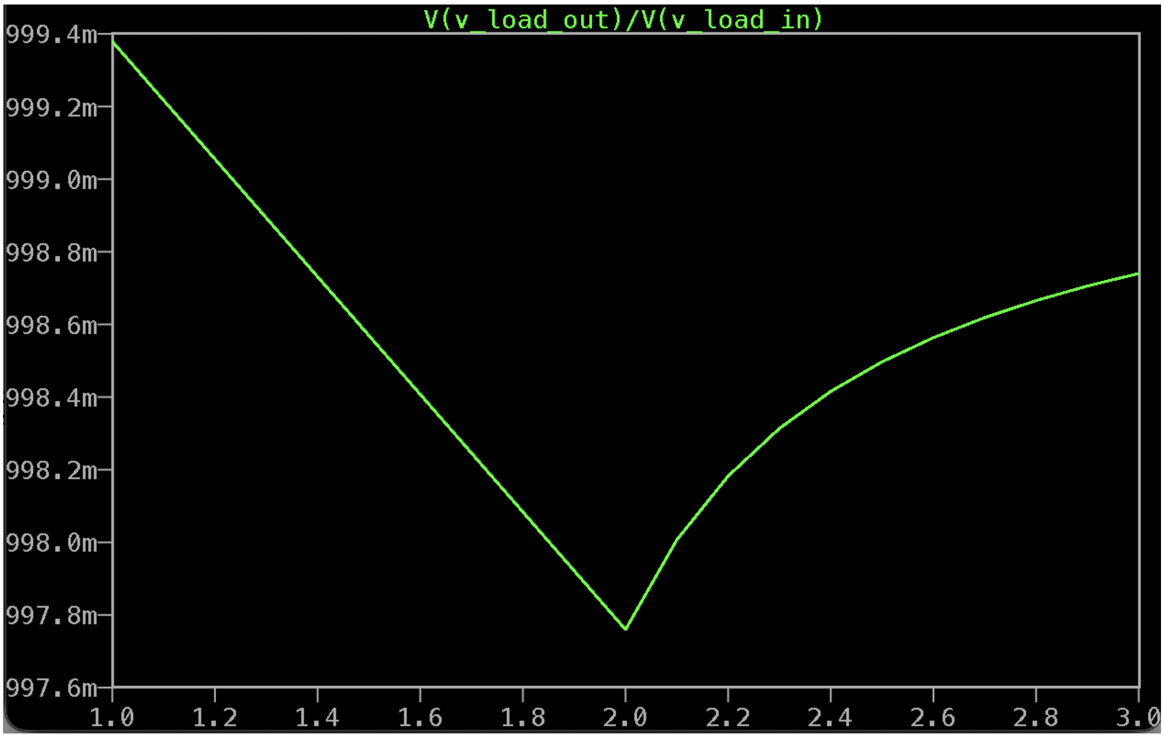

Figure 5.3: Normalised switched output voltage for the high-side load-switch active-load cases.

The supporting quantities were checked directly from the LTspice operating-point results. The voltage drop, $V_{\text{drop}} = V_{\text{in}} - V_{\text{out}}$, remained small for all three cases, confirming that the PMOS does not significantly reduce the supplied rail voltage. The PMOS gate-source voltage, $V_{GS,P}$, was negative in the on-state, showing that the gate was pulled below the source by the NMOS driver. The drain current, I_D, matched the expected active-load current for each stepped case, confirming that the switch supplied the required load current.

The normalised output voltage remains close to 1 for all three stepped load cases, showing that the switched output follows the relevant input rail for both the 3.3 V and 10 V branches. Since the voltage drop is low, the PMOS is correctly driven on, and the expected load current is delivered in each case, the switch is accepted for the specified active-load conditions.

5.6 Testing and Validation

Physical testing was conducted in White Lab using the passive components available for the prototype build. Measurements were taken using a digital multimeter, oscilloscope, DC power supply, and function generator.

ATP	Spec	Test evidence	Result
ATP01	Pack voltage sag	$V_{\mathrm{BAT}} = 12.04\,\mathrm{V}$ no-load and 11.72 V at 4.8 A; drop = 0.32 V < 0.5 V.	Pass
ATP02	3.3 V rail regulation and ripple	Output measured 3.27 V at approximately 150 mA; oscilloscope ripple measured 42 mVpp.	Pass
ATP03	H-bridge PWM and reversal	PWM measured 20.1 kHz; bridge output polarity reversed correctly when direction input was changed.	Pass
ATP04	Off-state leakage	Physical switch OFF: < 0.1 µA. Digital switch OFF: 2.8 µA to 3.4 µA, above the 1 µA limit.	Fail
ATP05	Cell voltage balance	Cell spread was 8 mV when charged and 14 mV after discharge; both remain below the 20 mV limit.	Pass

Table 5.7: Acceptance test procedure results.

Failure of ATP04: Off-state Leakage

ATP04 failed because the physical switch fully isolates the battery, while the MOSFET-based digital switches leave a small leakage path when OFF. The residual current is caused by IRF9530N off-state leakage and the gate-bias network, causing the digital branches to exceed the 1 µA target.

5.7 Risks and Recommendations

Permanent supervisor rail. A small always-on supervisor rail should be placed upstream of the main switch, supplying an ultra-low-power MCU, current/voltage monitor, and GNSS control. This would allow battery health and position to be monitored continuously while the downstream regulators and converters are fully disconnected in safe mode, removing their quiescent draw. It would also allow downstream faults to be isolated without switching off the controller itself. This should be validated by forcing low-battery and fault conditions and confirming that telemetry remains active while the main loads are cut off.

Battery charge tracking. The present voltage-based battery monitor can mistake load sag for a low battery, forcing a conservative safe-mode threshold. A future version should add coulomb counting, where a current sensor tracks charge entering and leaving the battery over time. This would estimate remaining capacity more accurately and allow more of the battery to be used without compromising protection.

TPS25947 eFuse on the motor branch. The motor branch should use a TI TPS25947 eFuse instead of relying on the polyfuse and BTS7960 fault sensing. A polyfuse rating is its hold current, not a precise trip point, so protection only occurs above the rated current and with delay. An eFuse provides a set current limit, faster shutdown, and fault/current reporting, giving more predictable protection during motor stall.

5.8 Conclusion

The developed power subsystem provides a protected and modular electrical architecture for the AUV prototype. It addresses the key requirement tensions of supplying high-current actuator loads, maintaining stable low-voltage rails, reducing standby losses, and protecting the battery and downstream circuits from faults.

Testing confirmed that the main power-delivery functions were successful. The battery maintained acceptable voltage under load, the regulated 3.3 V rail met its voltage and ripple limits, the motor driver produced the required PWM and direction reversal, and the cells remained balanced. The main weakness was digital-switch off-state leakage, which exceeded the 1 µA target despite the physical switch achieving near-complete isolation.

Overall, the subsystem meets its main objective of delivering reliable, regulated, and protected power to the AUV prototype. Future improvements should focus on ultra-low-leakage load-switch ICs, an always-on supervisor rail, improved battery charge tracking, and a dedicated motor-branch eFuse to strengthen long-duration deployment performance.

Chapter 6

Housing Subsystem

Prepared By: Lulama Lingela - LNGLUL002

6.1 Introduction

The housing subsystem forms the structural and environmental core of the autonomous profiling float. Its primary role is to protect all onboard electronics from the Antarctic ocean environment while simultaneously enabling the buoyancy-driven vertical motion required for bio-optical profiling. Unlike a simple enclosure, the housing is an active mechanical platform that integrates the piston-based buoyancy engine, provides calibrated mounting points for three external sensors, and sets the conditions for passive vertical stability through deliberate mass distribution.

The housing interfaces with all three other subsystems: the actuator subsystem's motor, gearbox, and lead screw occupy the lower dry zone; the power subsystem's battery and electronics are rack-mounted in the electronics tube; and the ECO FLNTU, TRN100, and MS5837-30BA sensors mount externally on the sensor-actuator collar with signal cables passing through sealed penetrations into the dry interior.

The scope of this subsystem covers the structural enclosure, multi-zone internal layout, sealing strategy, sensor mounting interfaces, ballast system, and mechanical integration of the buoyancy engine. It excludes the actuation mechanism, power electronics, and embedded control software, which are addressed in their respective subsystem chapters.

6.2 Requirements

The housing requirements were derived from the system-level acceptance test procedures and from the physical constraints imposed by the sensor datasheets, the actuator geometry, and the Antarctic deployment environment. The prototype targets shallow tank testing at 0–2 m with the structure over-rated to 5 m for margin; full-depth Antarctic deployment, ice interaction, and biofouling validation are out of scope.

6.2.1 Requirements definition

User requirements

Table 6.1: User requirements.

ID	User requirement
UR1	Protect onboard electronics from the marine environment for the deployment duration.
UR2	Enable controlled vertical profiling between the surface and the design depth.
UR3	Provide mounting and sealed signal access for three external bio-optical and environmental sensors.
UR4	Allow field servicing (battery charging, electronics access) without specialist tooling.
UR5	Be manufacturable from materials and processes available within the project resource allocation.

Functional and non-functional requirements

Table 6.2: Functional and non-functional requirements for the housing subsystem.

ID	Type	Requirement	Description
R1	Functional	Environmental isolation	Fully seal the electronics and power zones against seawater ingress.
R2	Functional	Selective zoning	Implement three distinct zones: a dry electronics zone, a wet-interface sensor zone, and an open buoyancy zone.
R3	Functional	Structural integrity	Withstand hydrostatic pressure at the design depth without permanent deformation, buckling, or seal failure.
R4	Functional	Sensor integration	Mount the ECO FLNTU, TRN100, and MS5837-30BA at 120° circumferential spacing with correct orientation.
R5	Functional	Buoyancy integration	Provide a sealed piston chamber and bulkhead interface for the actuator subsystem.
R6	Functional	Modular assembly	Allow zones to be independently detached via threaded joints, with the electronics zone accessible without disturbing others.
R7	Functional	Servicing access	Allow battery charging via an internal USB-C port without full disassembly.
R8	Non-functional	Corrosion resistance	Use materials compatible with Antarctic saline conditions across all wetted surfaces.
R9	Non-functional	Passive stability	Position the centre of buoyancy above the centre of mass to provide a passive righting moment.
R10	Non-functional	Low drag	Present a cylindrical external profile with no large protrusions perpendicular to the axis of motion.
R11	Non-functional	Fail-safe buoyancy	Remain net positively buoyant across the full piston stroke range, ensuring surface return on power or motor failure [?].
R12	Non-functional	Manufacturability	Produce all structural components by 3D printing (PLA/PETG) or off-the-shelf stock within the project allocation of R2000.

Specifications

Table 6.3: Quantitative specifications for the housing subsystem.

ID	Parameter	Value	Source
S1	Operating depth (prototype)	0–2 m	Project scope
S2	Pressure rating	$\geq$0.5 bar gauge	5 m depth margin
S3	CB–CM separation	$\geq$5 % of float length	Stability margin
S4	Net buoyancy (piston extended)	>0 N	Fail-safe return (R11)
S5	Total assembled mass	<5.2 kg	Buoyancy budget
S6	Seal rating	IP68 equivalent	Continuous submersion
S7	Piston stroke	~164 mm	Actuator subsystem

6.2.2 Requirements analysis and traceability matrix

The requirements interact in ways that drive key design trade-offs. The CB–CM stability target (S3) requires ballast mass, but the total mass is bounded by the buoyancy budget (S5) and must preserve net positive buoyancy at piston extension (R11, S4); ballast sizing was resolved using the reactive weight calculator (Section 6.4.1). Modular assembly (R6) requires more threaded joints, each adding a potential leak path conflicting with environmental isolation (R1); this was resolved by consolidating the sensor and actuator zones into a single printed part (Section 6.4.1). Wall thickness must be sufficient to withstand hydrostatic load (R3) without exceeding the print-time and material budget implied by R12.

Table 6.4: Traceability between user requirements, functional/non-functional requirements, specifications, and acceptance tests.

UR	Functional/NF requirements	Specifications	ATPs
UR1	R1, R3, R8, R11	S2, S6	ATP-H03, ATP-H07
UR2	R5, R9, R11	S1, S3, S4, S7	ATP-H04, ATP-H05, ATP-H06
UR3	R4	S6	ATP-H07
UR4	R6, R7	—	ATP-H02
UR5	R12	S5	ATP-H01

6.3 Design Decisions

This section documents the design choices behind the final housing architecture, ordered from the most foundational geometric decisions down to component-level selections. Where the prototype implementation differs from the ideal solution due to budget or availability constraints, both options are reported and a recommendation for field deployment is provided.

6.3.1 Architecture development

The housing architecture evolved through three configurations, each transition driven by integration constraints surfaced through cross-subsystem feedback.

Single-tube stacked layout: A single 120 mm ID cylinder was rejected because it had no provision for externally mounted sensors requiring direct seawater access, and routing sensor cables through the dry electronics zone introduced cross-contamination risk between dry and wet zones.

Coaxial overlapping architecture: Partial radial overlap of the piston chamber and electronics zone was rejected on a single decisive ground: a seal failure would flood the electronics zone directly rather than containing the failure to the wet zone. This would be an unacceptable single point of failure for a deployable instrument.

Modular threaded-zone architecture (final): The final architecture separates the float into independent zones joined by threaded interfaces, with sensors on a dedicated collar and the piston at the base. Four deliberate decisions shaped this configuration: piston-at-bottom orientation, an integrated sensor collar, length reduction, and a service-cap electronics tube, each detailed in the subsections below.

6.3.2 Cylindrical geometry

A cylindrical primary form was selected because it distributes external hydrostatic pressure efficiently through hoop stress rather than bending, and is widely used in existing profiling float platforms such as the Argo network [9]. Cylindrical geometries also permit standard O-ring face seals and minimise hydrodynamic drag during vertical profiling. Spherical housings were rejected as impractical for modular internal layout; rectangular cross-sections were excluded due to stress concentration at corners under pressure loading.

6.3.3 Multi-zone partitioning and orientation

The housing was partitioned into independent dry (electronics, actuator) and wet (sensor collar, buoyancy chamber) zones rather than a single internal volume, on the basis of reliability and serviceability. Compartmentalising the failure surface means a leak at any one sensor penetration or threaded joint is contained to the affected zone, rather than flooding the entire instrument. The dry electronics zone also remains directly inspectable and serviceable without fluid contamination risk to circuit boards.

Piston-at-bottom orientation. On the recommendation of the actuator subsystem team, the piston and external cylinder were reoriented to face downward at the base of the float. This change introduced two fail-safe properties: if motor power is lost at any piston position, net positive buoyancy returns the float to the surface without assistance [11]; and gravity acts in the direction that increases displaced volume, so even a stalled actuator offers some passive tendency to extend the piston and return to surface.

Integrated sensor collar. A dedicated sensor zone was added to host three externally mounted sensors at 120° spacing (R4). Later in development, the sensor collar and actuator tube were consolidated into a single co-printed middle piece, eliminating one threaded joint and its associated leak path. The resulting part uses a stepped bore geometry (Ø140 mm upper section widening to Ø161 mm at the lower actuator section), accommodating both sensor mounting features and the actuator assembly in a single print.

Service-cap electronics tube. Consolidating the battery pack and all electronics into a single

115 mm tube means the entire electronics assembly can be accessed and serviced by removing only the top service cap (quarter-turn bayonet lock with face O-ring) without disturbing the sensor or actuator zones below.

6.3.4 Sensor selection

The ECO FLNTU [74] was chosen for the bio-optical channel on the recommendation of the project's primary stakeholder, who had prior experience with the manufacturer (Sea-Bird Scientific) . It provides the minimum viable chlorophyll fluorescence and backscatter channels for phytoplankton detection, while remaining part of a family of sensors with a common mechanical and electrical form factor (ECO Triplet, ECO Puck), giving the end user flexibility to swap to a higher-specification sensor without mechanical redesign. The TRN100 was selected for its threaded G 1/4 body [75] that integrates cleanly into the printed sensor collar with a built-in flange O-ring, eliminating the need for a custom sealing solution.

6.3.5 Material selection

Structural components. PETG was specified for all printed structural components for its superior moisture resistance, impact toughness, and low-temperature dimensional stability relative to PLA, making it better suited to the harsh Antarctic environment where ice loading and thermal cycling are significant structural concerns [21]. However, only PLA filament was available within the project, so all printed parts were produced in PLA. PETG remains the recommendation for any deployment-grade iteration [44].

O-rings. EPDM was specified for all O-rings due to superior low-temperature flexibility and saltwater resistance relative to NBR or silicone [23]. NBR 70 Shore A was used throughout the prototype as EPDM O-rings in the required sizes were unavailable within the project budget. NBR is acceptable for short-duration tank testing; EPDM is recommended for deployment.

Fasteners. All fasteners are A4 316 stainless steel for saltwater corrosion resistance.

Biofouling. Biofouling on optical sensor windows is a known risk in extended deployments [26] and would require anti-fouling coatings or mechanical wipers on the ECO FLNTU face for any mission beyond short-duration tank testing.

6.3.6 Sealing strategy

The housing uses face O-ring seals at all threaded joints and integral seals at sensor penetrations (Table 6.5). Face O-ring grooves are dimensioned to compress the cord by approximately 25 % at assembly, per standard face-seal practice [2].

Table 6.5: Sealing elements and their locations in the assembled housing.

Location	**Seal type**	**Sealing element**
Top cap to electronics tube	Bayonet + face O-ring	NBR 70 ShA, w 3.53 mm

Table 6.5 continued

Location	Seal type	Sealing element
Electronics tube to sensor-actuator tube	Face O-ring	NBR 70 ShA, w 3.53 mm
Sensor-actuator tube to external cylinder	Face O-ring	NBR 70 ShA, w 3.53 mm
ECO FLNTU penetration	Bulkhead	MCBH-6 integral O-ring [76]
TRN100 temperature sensor	Threaded face	G 1/4 integral flange O-ring [75]
MS5837 depth sensor [54]	Radial	Sensor lid O-ring in Ø3.07 mm bore [77]

Lead screw shaft interface. The lead screw passes through the disc separating the actuator dry zone from the external wet cylinder. Because the screw is fully threaded along its length and translates vertically, a conventional dynamic shaft seal was not feasible within the prototype timeline. A telescoping concentric guide cylinder, consisting of nested PLA rings that extend during piston extension and collapse during retraction, is proposed for the field deployment configuration as a means of providing a smooth, sealable surface for a dynamic shaft seal stack.

6.3.7 Mass distribution and ballast determination

Passive vertical stability (R9) requires the centre of buoyancy to lie above the centre of mass. Since the electronics zone, the heaviest dry subassembly, resides at the top of the float, an active ballast strategy was needed to lower the composite CM. A reactive weight calculator was developed (Figure 6.1) to size the ballast ring. The tool accepts ring outer diameter, height, inner diameter, and material, alongside adjustable zone heights, and computes ring mass, composite CM position, CB–CM separation as a percentage of float length, net buoyancy force across the piston stroke, and the equilibrium piston position at neutral buoyancy.

Using slicer-derived masses for all printed components and BOM masses for electronics, sensors, and mechanical parts, the system mass without ballast is 1.63 kg. A ballast shell (OD 200 mm, ID 126 mm, height 80 mm) filled with a combination of M10 × 100 mm hex bolts (720 g) and building sand ($1920\,\mathrm{kg\,m^{-3}}$) yields a total ballast mass of 3574 g, producing a CB–CM separation of 28.2 % of float length, well above the 5 % target (S3), with a net upward buoyancy of 27.56 N at full piston extension. The mixed bolt-and-sand fill allows incremental ballast trim during tank testing; a machined 316 stainless steel ring is recommended for field deployment for more precise, moisture-stable ballast.

The calculator confirmed that the equilibrium piston position at neutral buoyancy is 43.2 mm from the base of the external cylinder (26 % of stroke), and that net positive buoyancy is retained across the full piston stroke. This is consistent with Argo-style profiling float operation, in which piston position controls the *magnitude* of the net buoyancy force rather than enabling hovering at a fixed depth [11]. Both the equilibrium position and the net buoyancy profile were communicated to the controller subsystem as control-law inputs.

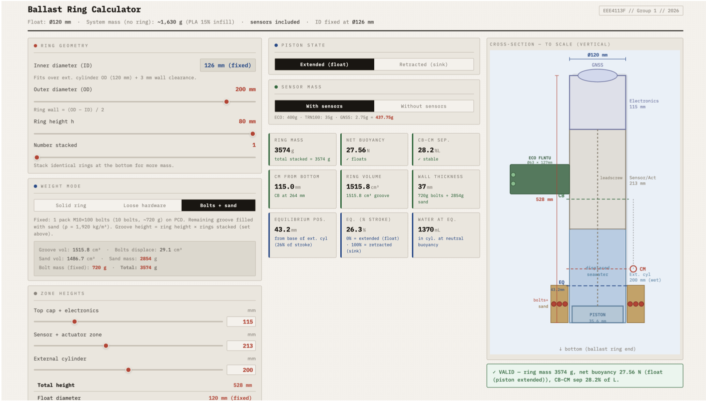

Figure 6.1: Reactive weight calculator showing the stability and buoyancy calculation for the prototype configuration.

6.4 Final Design

6.4.1 Architecture overview

The final housing consists of four stacked assemblies joined coaxially along the vertical float axis (Figure 6.2). From top to bottom: the service cap, electronics tube, sensor-actuator tube, and flanged base with external wet cylinder. Total assembled float length is approximately 528 mm; key dimensions are tabulated in Appendix 13.2.

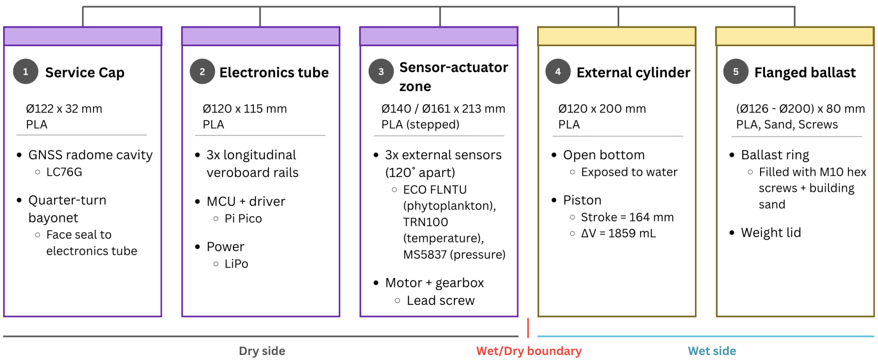

Figure 6.2: System architecture of the housing subsystem. Zones are colour-coded by function. CB and CM markers indicate the calculated stability positions for the ballasted assembly.

6.4.2 Service cap

The service cap seals the electronics tube via a quarter-turn bayonet lock with a single NBR face O-ring. A recessed radome cavity in the cap roof accommodates the LC76G GNSS patch antenna with the required 1 mm–2 mm antenna-to-radome clearance, with no metallic features within 10 mm of the patch to avoid signal attenuation.

6.4.3 Electronics tube

The electronics tube (PLA, Ø120 mm ID) houses all power and control electronics on a three-rail vertical mounting system, allowing independent insertion and removal of each carrier board without disturbing those above. The USB-C charging port is located internally on a carrier board rather than

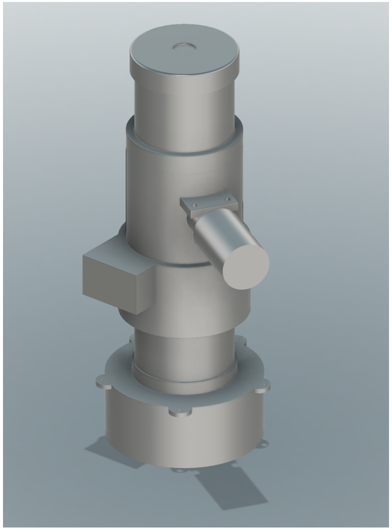

(a) Isometric CAD view.

(b) Assembled full-size model.

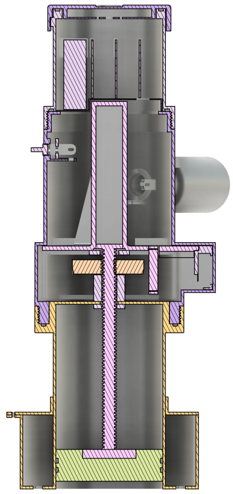

(c) Cross-section — right view.

Figure 6.3: Final assembly and CAD renderings of the housing model and internal sealing arrangement. Component-level renders with cross-sections are provided in Appendix 13.4.

as a side-wall penetration, eliminating a potential leak path.

6.4.4 Sensor-actuator tube

The sensor-actuator tube is a stepped-bore PLA print housing the motor and gearbox in its wider lower section, with three external sensor mounting features at 120° spacing on the upper section: an M4 brass-insert pad for the ECO FLNTU L-bracket, a G 1/4 BSPP threaded boss for the TRN100, and a precision bore for the MS5837. The three-part assembly (top, middle, bottom) allows the shaft seal stack to be located at the mid-section bulkhead where the lead screw exits the dry zone.

6.4.5 Flanged base and external wet cylinder

The flanged base transitions the sensor-actuator tube to the external wet cylinder (PLA, Ø120 mm ID, 3 mm wall), which is open at the bottom to allow free water ingress and egress as the piston translates. The ballast ring (sand and hex screw fill) is secured at the base of the flange; the mixed-fill approach allows incremental trim during tank testing while achieving the required CB–CM separation (Appendix 13.1.4).

6.4.6 Submodule analysis and extensions

Stability sensitivity analysis

The ballast ring geometry was swept across ±5 % dimensional tolerance and zone heights varied by ±10 mm. The CB–CM separation remained above the 5 % target (S3) across the full parameter sweep. The full calculation is provided in Appendix 13.1.4.

Hydrostatic buckling check

The external wet cylinder is the element most exposed to external pressure. Using the classical thin-walled buckling expression [78]:

$$P_{\mathrm{cr}} = \frac{2E}{1-\nu^2}\left(\frac{t}{D}\right)^3 \tag{6.1}$$

For the PLA wet cylinder ($E = 3.5\,\mathrm{GPa}$, $\nu = 0.36$, $t = 3\,\mathrm{mm}$, $D = 120\,\mathrm{mm}$), $P_{\mathrm{cr}} \approx 2.4\,\mathrm{bar}$, giving a safety factor of $\sim$4.8 against the 0.5 bar design pressure (S2).

Finite element analysis (hydrostatic pressure)

Static FEA was performed in SimScale on the three primary housing components under 19.62 kPa hydrostatic pressure ($P = \rho g h$, 2 m depth), with PLA properties ($E = 3.5\,\mathrm{GPa}$, $\nu = 0.36$, $\sigma_y = 50\,\mathrm{MPa}$) and a fixed support at the lower mating face of each component. All three satisfy requirement S2 with safety factors well above 2.0 (Table 6.6). The lowest margin of 11.5 occurs in the sensor-actuator zone at the ECO FLNTU bracket recess, which is a geometric stress concentration rather than a global structural failure mode. Maximum displacements are sub-millimetre across all components. Full stress and displacement plots are provided in Appendix 13.3.

Table 6.6: FEA results summary under 19.62 kPa hydrostatic pressure. Safety factor = $\sigma_y/\sigma_{\max}$, $\sigma_y = 50\,\mathrm{MPa}$.

Component	**Max σ_{VM} (MPa)**	**Max disp. (mm)**	**Safety factor**
Electronics tube	1.70	0.009	29.4
Sensor-actuator zone	4.35	0.112	11.5
External wet cylinder	0.84	0.020	59.7

Together, these analyses confirm that the housing structure is adequately dimensioned for the 2 m proof-of-concept operating depth. The analytical buckling check gives a safety factor of 4.8 on the most pressure-exposed component, and the FEA safety factors range from 11.5 to 59.7 across the three primary components, which are all well above the minimum of 2.0 [21]. The FEA and analytical results are consistent for the external wet cylinder, providing mutual validation of both methods. The dominant structural risk is the geometric stress concentration at the ECO FLNTU bracket recess in the sensor-actuator zone. Adding a fillet radius at this corner is recommended for future iterations but is not required at the prototype operating depth.

Design extensions

For deployment beyond the proof-of-concept scope, three substitutions are recommended: PETG filament and EPDM O-rings for improved moisture and low-temperature performance; a machined 316 stainless steel ballast ring for precise, moisture-stable trim; and a telescoping guide cylinder around the lead screw to provide a clean dynamic seal surface at the bulkhead.

6.5 Testing and Verification

Physical testing was conducted in three stages: bench-level dimensional and fit verification, a scaled-down prototype to validate the overall layout, and incremental submersion tests on the full-scale assembly. The modular zone architecture was key to the sealing strategy — each interface was tested in isolation before full assembly submersion, allowing any ingress to be attributed to a specific joint. All tests correspond to ATP-H01 through ATP-H07 defined in Appendix 13.6; results are consolidated in Table 6.7.

6.5.1 Bench verification (ATP-H01, ATP-H02)

Critical dimensions were verified using digital calipers before assembly. The electronics tube bore measured Ø120.2 mm (0.2 mm from nominal), within the snug-fit clearance budget. Face O-ring grooves measured 2.6 mm depth and 5.3 mm width, matching the 74 % compression target for the 3.53 mm wire O-ring. The MS5837 boss bore was reamed to Ø3.07 mm post-print and engaged correctly. All dimensions passed ATP-H01.

Dry assembly revealed two rework items: the piston was sanded down to correct an exact bore match causing excessive friction, and a clearance slot was added to the actuator section to accommodate the motor base protrusion. Both were incorporated into the final design. A 25 % scale prototype printed prior to full-scale build identified a shallow bayonet lug and sensor pad fillet collisions, both corrected by CAD revision. After rework, all joints and the bayonet cap engaged correctly (ATP-H02).

6.5.2 Submersion and sealing tests (ATP-H03, ATP-H04, ATP-H07)

Each of the four sealing interfaces — piston dynamic seal, sensor penetrations, zone face seals (J1, J2), and service cap — was submerged independently before full assembly testing. This incremental approach proved valuable: every ingress source was isolated and characterised before full submersion was attempted.

The piston completed the full ∼164 mm stroke in both directions with O-rings lubricated and the cylinder flooded; no ingress or rollover was observed (ATP-H04 passed). All three sensor penetrations were dry after 5 min at 0.5 m (ATP-H07 passed): MCBH-6 bulkhead, G 1/4 TRN100 boss, and MS5837 radial bore.

Both threaded zone joints (J1, J2) passed their interface-specific sealing criteria. However, water ingress was observed through the bulk PLA wall material at both joints and at the service cap — separate from the O-ring interfaces, which performed as designed. At the service cap, a tolerance adjustment to the inner diameter introduced micro-gaps in the printed wall; even after correcting an initially mis-joined O-ring cord, seepage continued through the wall rather than past the seal, confirming a material rather than geometry failure.

PLA printed by FDM (fused deposition modelling) can exhibit inter-layer micro-voids that allow slow water permeation under sustained submersion [44]. This is addressed for deployment through PETG substitution or waterproofing coating. For the prototype, the practical consequence was that prolonged full-assembly submersion was not feasible, limiting ATP-H03 and ATP-H06.

6.5.3 Buoyancy and stability tests (ATP-H05, ATP-H06)

Neutral buoyancy (ATP-H05). The calculated sand ballast was added to the ballast ring, and the mock ECO FLNTU body was filled with sand to match the sensor's datasheet mass. On initial pool deployment the float leaned toward the mock sensor due to its radially asymmetric mass; a counterweight of equivalent mass placed on the opposite side inside the sensor-actuator zone corrected this. The float then achieved stable vertical orientation and hovered within the target depth band. ATP-H05 passed after lateral trim correction; this asymmetry will be accounted for in the final ballast design.

Stability self-righting (ATP-H06). Sustained submersion was not achievable due to PLA porosity, preventing repeated self-righting trials. The CB–CM separation of 28.2 % is analytically verified and confirmed robust across the full sensitivity sweep (Appendix 13.1.4); stable vertical orientation was demonstrated in ATP-H05. ATP-H06 is recorded as not completed on this prototype, with self-righting behaviour analytically verified. A waterproofed or PETG-printed prototype is required for full experimental validation.

Table 6.7: Consolidated ATP results for the housing subsystem.

ID	Test	Result	Notes
ATP-H01	Dimensional verification	Pass	All dims within ±0.2 mm
ATP-H02	Dry assembly fit check	Pass	Piston sanded; motor clearance slot added
ATP-H03	Static waterproofing (IPX7)	Fail	PLA wall porosity; sealing interfaces passed independently
ATP-H04	Piston travel (wet)	Pass	No binding or O-ring rollover across full stroke
ATP-H05	Neutral buoyancy	Pass	Lateral counterweight added opposite mock ECO FLNTU
ATP-H06	Stability self-righting	Not completed	PLA porosity prevented sustained submersion; analytically verified
ATP-H07	Sensor penetration seal	Pass	All three penetrations dry after 5 min at 0.5 m

The bench tests (H01, H02) confirmed dimensional accuracy and assembly fit. The incremental sealing strategy successfully isolated all interfaces: H04 and H07 passed, and both zone joints passed their interface criteria. The dominant finding was PLA material porosity, a known FDM limitation rather than a seal design failure, which prevented full IPX7 certification and self-righting validation on this prototype. H05 passed after a lateral trim correction to be incorporated into the final ballast design. Full H03 and H06 validation requires a waterproofed or PETG-printed prototype.

6.6 Conclusion

The housing subsystem was developed as the structural and environmental core of the autonomous bio-optical profiling float, integrating the piston-based buoyancy engine, three external sensors, and all power and control electronics into a single modular assembly. The adopted modular threaded-zone architecture, selected from three candidate configurations, satisfies all five user requirements for environmental isolation, controlled vertical profiling, sealed sensor access, field serviceability, and manufacturability within the project resource allocation.

The reactive weight calculator produced a verified CB–CM separation of 28.2 % of float length, exceeding the 5 % stability target with margin confirmed across a ±5 % parameter sweep. The analytical buckling safety factor of 4.8 and FEA safety factors of 11.5–59.7 across the three primary components confirm the structure is adequately dimensioned for the 2 m proof-of-concept operating depth.

Physical verification passed the dimensional (ATP-H01), dry-fit (ATP-H02), piston travel (ATP-H04), sensor penetration (ATP-H07), and neutral buoyancy (ATP-H05) acceptance tests. The dominant finding from wet testing was PLA material porosity, a known FDM limitation rather than a seal design failure, which prevented full IPX7 certification (ATP-H03) and self-righting validation (ATP-H06) on the prototype.

Three substitutions are recommended for a deployment-grade revision: PETG in place of PLA, EPDM in place of NBR O-rings, and a machined 316 stainless steel ballast ring in place of the sand-filled shell. The lead screw shaft seal remains the single unresolved sealing interface; a telescoping concentric guide cylinder is the proposed path to closing it before any field deployment.

Chapter 7

Conclusions

The purpose of this project was to design and implement a proof-of-concept autonomous buoyancy-driven profiling float capable of regulated vertical depth control, addressing the need for a low-cost autonomous platform for phytoplankton concentration monitoring in Antarctica. The system targeted a maximum operating depth of 2 m, within a budget of R2 000 over a ten-week development period.

Chapter 1 established the scientific need identified by Sandy, the client at MARiS, for persistent autonomous phytoplankton measurement in the Southern Ocean, where ship-based sampling is costly and logistically constrained. Chapter 2 surveyed autonomous marine platforms, depth control strategies, power systems, and system limitations, concluding that a buoyancy-driven architecture with cascaded depth control and a battery-driven power system is the most appropriate approach for a low-cost proof-of-concept system. These findings directly informed the requirements and design decisions across all four subsystems.

Chapter 3 presented the lead-screw piston mechanism driving the buoyancy engine, demonstrating functional proof-of-concept operation with lead screw buckling identified as a rectifiable FDM print parameter issue. Chapter 4 presented the cascaded depth control architecture, validated through software-in-the-loop simulation, achieving zero-overshoot depth tracking with a discrete phase margin of 50.69° at 200 Hz and satisfying all ATP requirements under nominal conditions. Chapter 5 described the power subsystem, which delivered a regulated 3.3 V rail and motor drive output within specification, with the notable exception being digital-switch off-state leakage above the 1 µA standby target. Chapter 6 detailed the modular sealed enclosure, which achieved a CB–CM separation of 28.2 % of float length and passed five of seven ATPs, with the remaining two not met due to PLA material porosity, a known FDM limitation rather than a seal design failure.

All subsystems were independently verified against their acceptance test procedures. Full system integration testing could not be completed prior to the submission deadline due to 3D printing delays, assembly errors with knock-on effects across subsystems, and PLA unreliability under wet conditions. Integration and cross-subsystem validation will be completed ahead of the final demonstration.

In summary, the project achieved the goals that were set out by designing and demonstrating a modular buoyancy-driven profiling float in which each subsystem independently satisfies its functional requirements. The identified limitations are well-understood and confined primarily to FDM material properties and prototype assembly constraints, and do not undermine the viability of the design approach.

Chapter 8

Recommendations

Based on the results achieved for the individual subsystems, some recommendations can be made for future iterations on this design:

Firstly, for the system to be implemented in the field, a GNSS system to transmit the location of the AUV for data retrieval still needs to be implemented. Although, the power supply, housing and communications connection to the microcontroller have already been configured, a full implementation of the firmware and hardware configuration required to transmit location data are still required.

Next, we recommend that the housing and piston head be coated in waterproofing paint to properly protect the internal components from flooding and damage. Due to time constraints this was not carried out, however it is absolutely critical for longer deployments as PLA and even PETG are not fully waterproof materials. Alternatively, fully waterproof materials could be used.

Lastly if we wanted to extend the deployment range of the system to areas with high ice coverage, a thruster based ice avoidance system is proposed. This theoretical system would allow the system to move horizontally for brief periods when it is under an ice layer; allowing the system to resurface for location data transmission and device retrieval. This system would have to be coupled with some additional ice sensing capabilities, as well as an additional control system to prevent roll.

Chapter 9

Appendix: Bill of Materials

Table 9.1: Bill of Materials

Component	Quantity	Unit Cost (R)	Total Cost (R)	Subsystem
NBR O-ring Cord 3.53 mm Diameter, 2.5 m Length	1	11.50	11.50	Housing
Circular Connector – RD24 Style Econo Series 7 Pole (6P+Earth) Panel Flange Mount Male Solder Terminal, 10A/250VAC, IP67	1	100.98	100.98	Housing
PLA Filament	1.37 (kg)	299.00(R/kg)	409.63	Housing
O-ring 2.0X1.0-70 Shore 70	1	0.50	0.50	Housing
M10x100mm Hex Screws and Bolts	16	11.00	176.00	Housing
Building Sand (3kg)	1	2.00	2.00	Housing
Raspberry Pi Pico 2W Dev Board	1	158.70	158.70	Actuator
RS PRO Geared DC Motor, 19.68 W, 3V dc, 7.2 V dc, 107.3 g.cm, 22356 rpm, 2.3 mm Shaft Diameter	1	155.42	155.42	Actuator
PLA Filament	0.195 (kg)	0.299 (R/kg)	58.31	Actuator
Radial Bearing	1	13.33	13.33	Actuator
Thrust Bearings	4	11.11	44.44	Actuator
MS5837-02BA Depth Sensor	1	111.58	111.58	Control
AS5600 Magnetic Hall Effect Sensor	1	46.87	46.87	Control
3.7V Rechargeable Lithium Battery	3	95.00	285.00	Power
18650 Battery Holder – Wire – 3 Cell	1	10.35	10.35	Power
HKD 3S Lithium Battery Charge/Protection 10A	1	22.00	22.00	Power
LiPo Charger Boost Board 3S 2A	1	32.20	32.20	Power
BMT ADJ DC/DC Module 3A, 1.5–35V	1	19.80	19.80	Power
XL6009 DC-DC Adjustable Buck Boost Module	1	46.00	46.00	Power
INA226 DC I2C Current Sensor Logic 3.3V and 5V	1	91.35	91.35	Power

Component	**Quantity**	**Unit Cost (R)**	**Total Cost (R)**	**Subsystem**
160mA Poly Switch	1	3.45	3.45	Power
3A Poly Switch	1	6.83	6.83	Power
4A Poly Switch	1	6.35	6.35	Power
40 Pin Female Header	1	4.50	4.50	Power
40 Pin Male Header	1	2.00	2.00	Power
KCD8 Switch 220V 6A Black – Threaded	1	16.10	16.10	Power
Capacitor 100 nF Ceramic	3	1.10	3.30	Power
Capacitor 10 μF	2	0.60	1.20	Power
220 μF Electrolytic Capacitor	1	1.21	1.21	Power
34 μH Power Inductor	1	7.40	7.40	Power
Veroboard (1/3 used)	1	25.00	25.00	Power
Motor Driver (BTS7960)	1	91.75	91.75	Power
1.5 mm^2 Wire (0.5 m)	1	5.00	5.00	Power
0.5 mm^2 Wire (0.5 m)	1	5.00	5.00	Power
ST Micro 7805 Linear Voltage Regulator 5V 1A (Max 1.5A)	1	5.00	5.00	Power
2.2kΩ Resistor	2	0.35	0.70	Power
220kΩ Resistor	2	0.35	0.70	Power
IRF9530 MOSFET P-Channel	1	10.00	10.00	Power
2N700 PNP Transistor	1	2.50	2.50	Power
		Total	**1993.95**	

Chapter 10

Appendix: Actuation System

10.1 Dimension Analysis Further Discussion

When choosing the radius of the piston cylinder, a few things need to be taken into account:

The choice of radius has large implications on the power requirements, since the force and thus power required from the motor is directly proportional to cylinder radius via: $F_{piston} = P(\pi r^2)$, where P is water pressure and $P_{mech} = Fv$, where P_{mech} is mechanical power. To summarise, the smaller the choice of radius, the smaller the required mechanical power from our motor.

On the other hand the choice of radius is also hugely impactful on the length of the cylinder, since the piston must maintain a constant volume. Thus, from $V = \pi r^2 l$, we can see that length is inversely proportional the square of the radius, meaning a small decrease in the radius can drastically increase the length.

The choice between cylinder radius then, therefore represents a trade-off between power requirements and length of the actuator. For our printed system a longer length would mean longer print times and higher filament cost, as well as increased mechanical instability to ocean currents. $6cm$, was seen as the optimal operating point here and was decided upon using the code available on our Github. Below is a a table of possible radius values that could have been used and their impact on the power and length requirements of the system:

radius(cm)	**Mechanical Power**	**Length (cm)**
3	1.6	71
6	6.3	18
9	14.2	8
12	25.3	4

Table 10.1: Table Showing Trade-offs Associated with Different Radius sizes

10.2 Piston Head

An image for the final CAD design of the piston head is seen below:

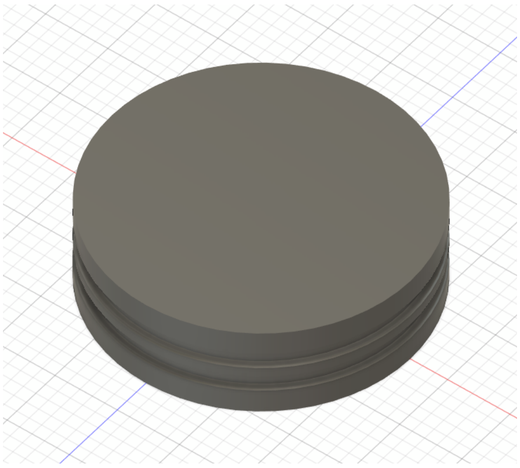

Figure 10.1: Image Showing final design of CAD model

The thickness of the piston head used was $3.56cm$, which was calculated to meet our stress requirements. Notably the piston head was printed using PETG, outside of UCT using a 3-D printing company. This was done to ensure water-proofing to pass ATP01. To assist in the waterproofing of the final design O-ring grooves were also added into the design, as seen in Figure 3.5 with a $0.5mm$ chamfer around the edges to ensure easy integration of O-ring sealing. This sealing however, was not tested for this report, however as it would require full system integration with the housing subsystem, which had not been done yet.

10.3 Screw Failure

The image below shows the screw after being glued back together. Due to the likelihood of the screw breaking again all subsequent full load tests were abandoned until a stronger screw can be reprinted:

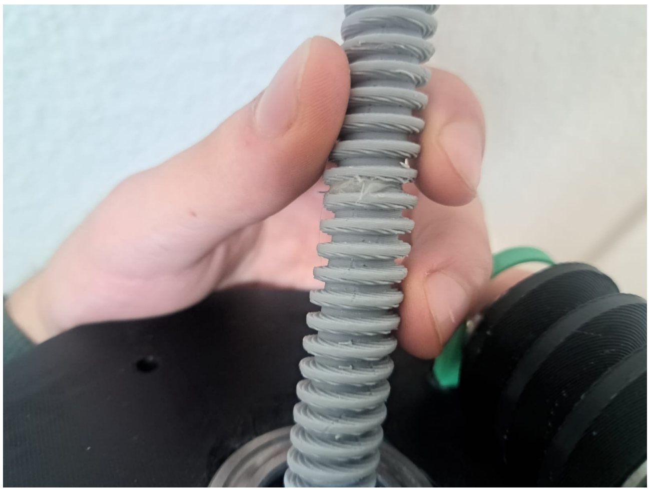

Figure 10.2: Image showing the Failure caused by the Full Load Test

Chapter 11

Appendix: Controller Subsystem

11.1 Plant Modelling

Figure B.1 — Step Response of the Full Third-Order Plant

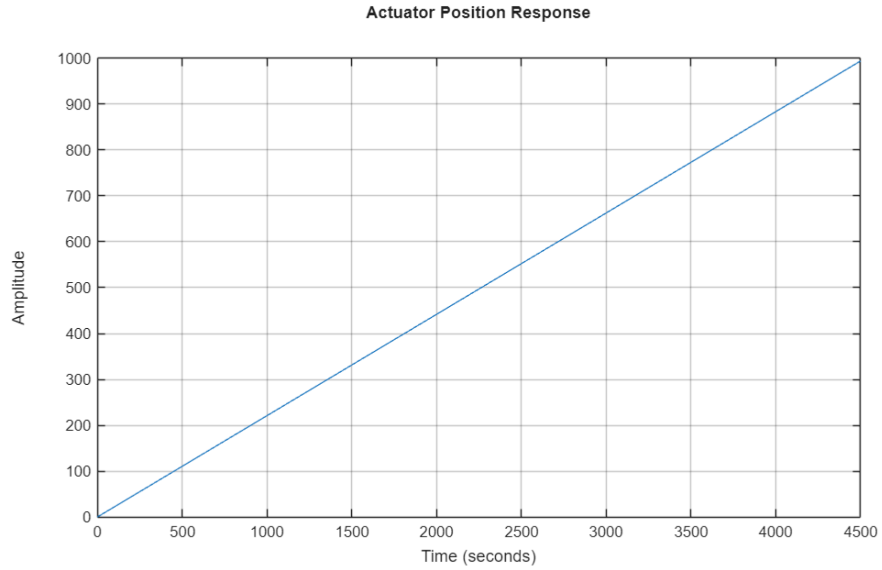

Figure 11.1: Step response of the full third-order plant $G_{\text{position}}(s)$. The ramp output confirms the presence of the position integrator — a constant voltage input produces linearly increasing position, with slope equal to the DC velocity gain of 0.221 m/s/V.

Figure B.2 — Bode Plot of the Full Third-Order Plant

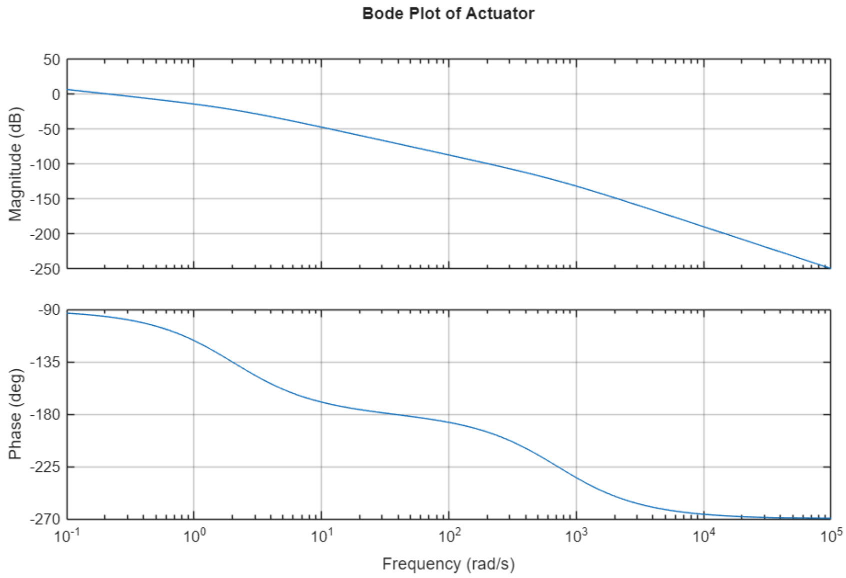

Figure 11.2: Bode plot of the full third-order plant. Phase begins at $-90°$ at low frequency (confirming the position integrator), passes through $-180°$, and approaches $-270°$ at high frequency, consistent with a three-pole system.

Figure B.3 — Third-Order vs Second-Order Model Comparison

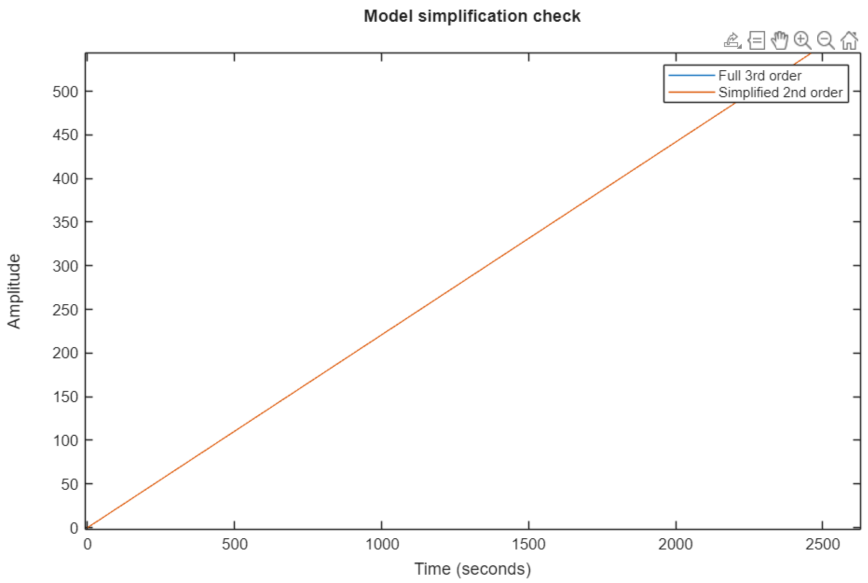

Figure 11.3: Step response comparison of the full third-order and simplified second-order plant models. The two responses are visually indistinguishable, confirming that the electrical pole at -712.89 rad/s ($\tau_e = 1.4$ ms) has negligible influence relative to the dominant mechanical pole at -2.02 rad/s ($\tau_m = 1.1$ s).

11.2 Inner Loop Design

Figure B.4 — MATLAB sisotool Session: Inner Loop Compensator

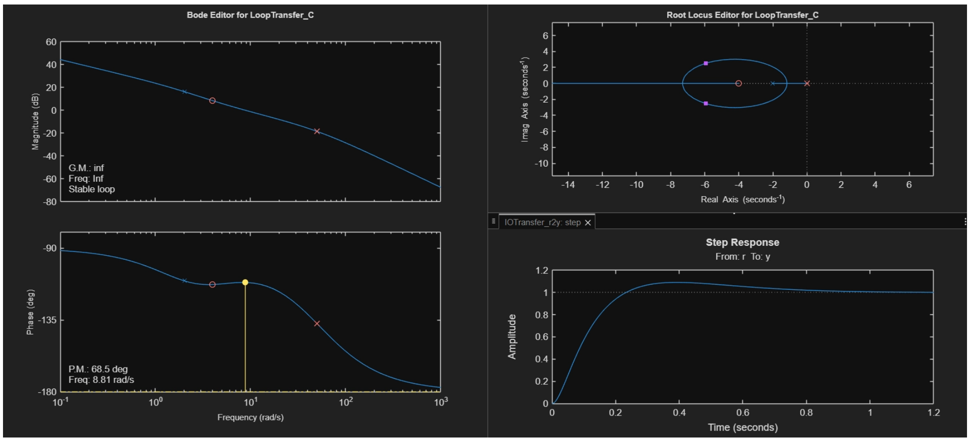

Figure 11.4: MATLAB sisotool session for the inner velocity loop. The step response panel shows the response reaching exactly 1.0, confirming unity DC gain and zero steady-state velocity error.

Figure B.5 — Root Locus of the Inner Loop

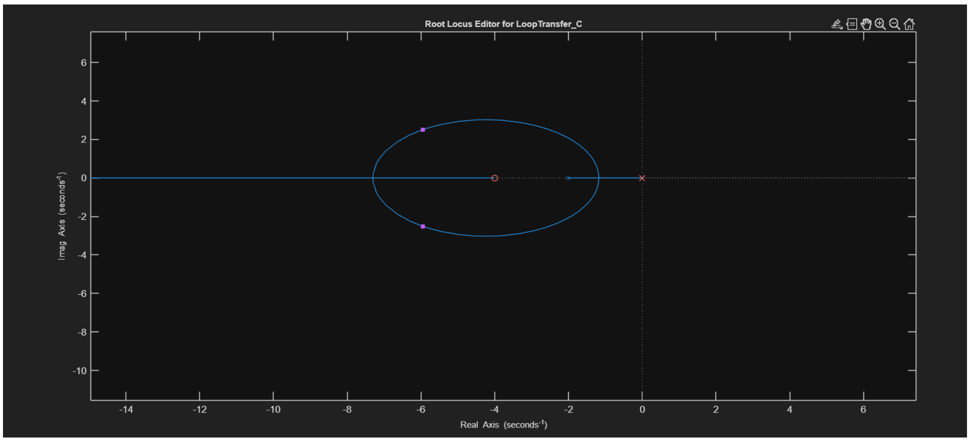

Figure 11.5: Root locus of the inner loop open-loop transfer function $L_{\text{inner}}(s) = C_{\text{inner}}(s) \cdot G_{\text{inner}}(s)$. All closed-loop poles remain in the left half-plane at the selected gain, confirming closed-loop stability. The dominant complex pole pair has natural frequency $\omega_n \approx 6.45$ rad/s and damping ratio $\zeta \approx 0.92$.

Figure B.6 — Inner Loop Closed-Loop Step Response

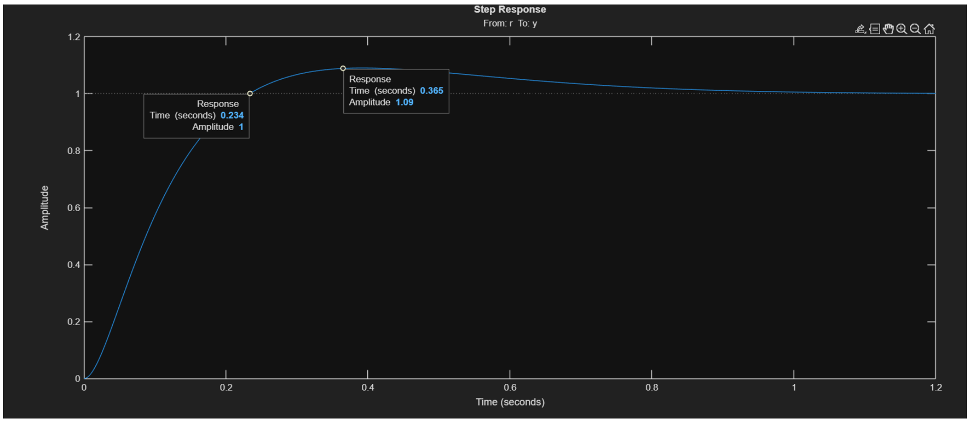

Figure 11.6: Closed-loop step response of the inner velocity loop. The response reaches exactly 1.0 (DC gain = 1.0000), confirming zero steady-state velocity error. Rise time is approximately 0.23 s with overshoot below 15%, both within specification.

Figure B.7 — Inner Loop Open-Loop Bode Plot

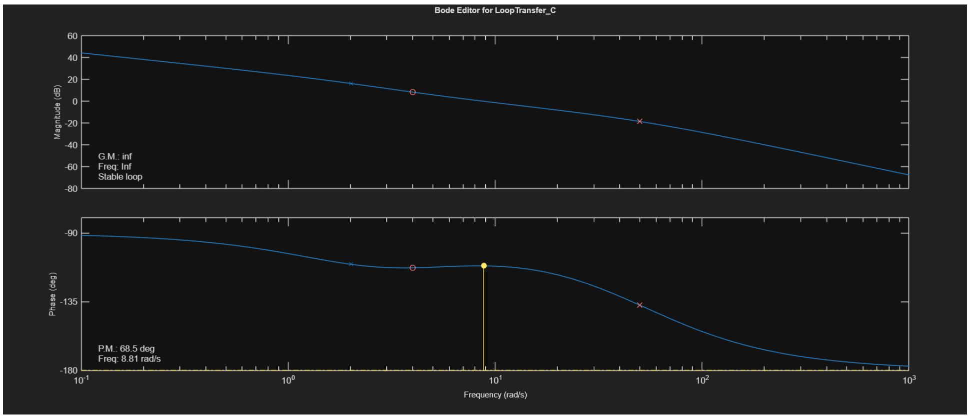

Figure 11.7: Open-loop Bode plot of the inner velocity loop with gain and phase margins annotated. Phase margin PM = 61.53° and gain margin GM = ∞ (the phase never crosses −180°). Bandwidth is 21.53 rad/s.

11.3 Outer Loop Design

Figure B.8 — Outer Loop Plant Bode Plot

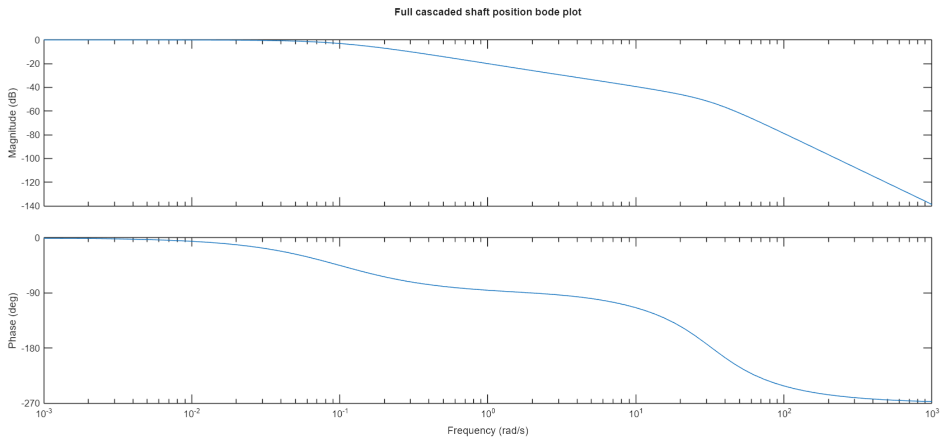

Figure 11.8: Bode plot of the outer loop plant $G_{\text{outer}}(s) = T_{\text{inner}}(s) \cdot (1/s)$. The approximately first-order slope at low frequencies confirms that the fast inner loop dynamics have been absorbed, presenting a well-behaved plant to the outer loop and confirming the cascade separation is effective.

Figure B.9 — Outer Loop Step Response (Shaft Model, $K_{\text{outer}} = 0.1$)

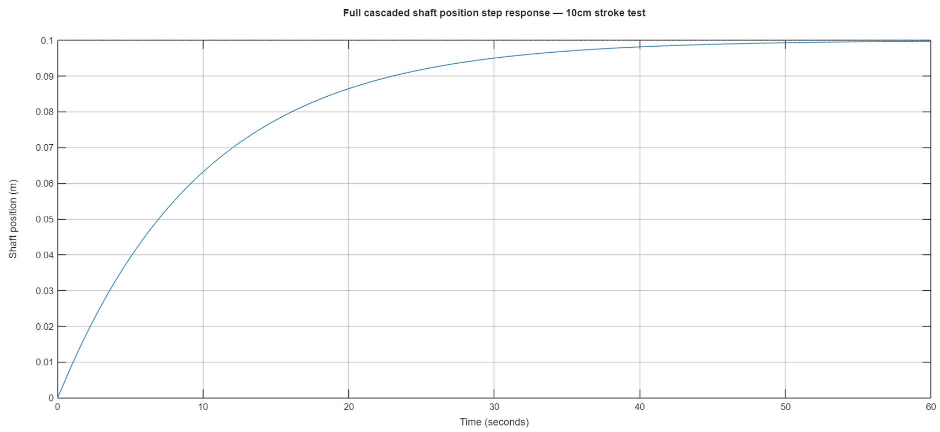

Figure 11.9: Closed-loop step response of the outer position loop on the MATLAB shaft model with $K_{\text{outer}} = 0.1$. Zero overshoot is achieved and the shaft settles in approximately 39 s for a 10 cm step. Note that this represents shaft position response only; the actual depth settling time is longer due to buoyancy dynamics captured in the SIL simulation (Appendix 11.7).

11.4 Sensitivity Analysis

Figure B.10 — Sensitivity and Complementary Sensitivity Bode Magnitude

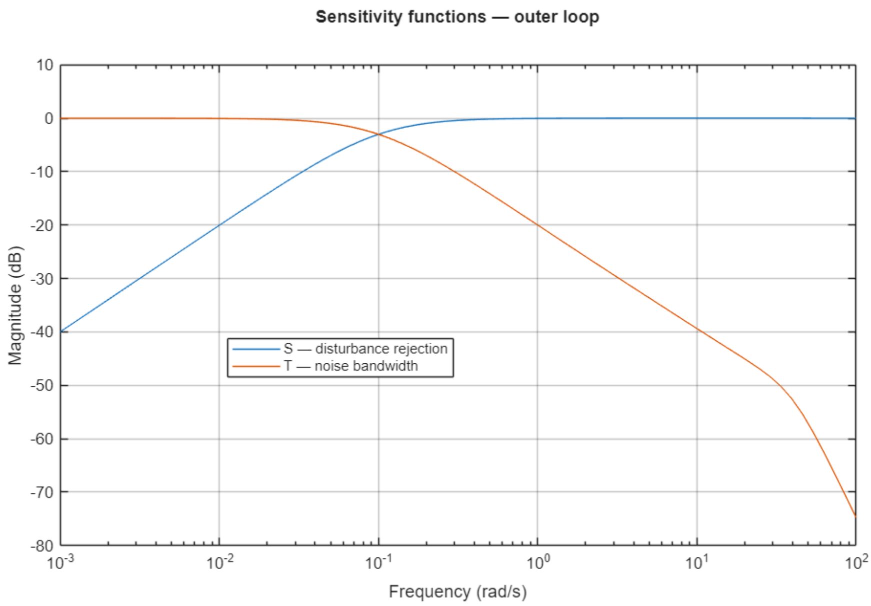

Figure 11.10: Bode magnitude of the sensitivity function $S(s)$ (disturbance rejection) and complementary sensitivity function $T(s)$ (noise bandwidth). Peak $|S| = 0.87$ dB is well below the 6 dB robustness specification, confirming disturbances are attenuated rather than amplified. $T(s)$ rolls off above the outer loop bandwidth, confirming high-frequency noise is attenuated before reaching the motor command.

Figure B.11 — Disturbance Step Response

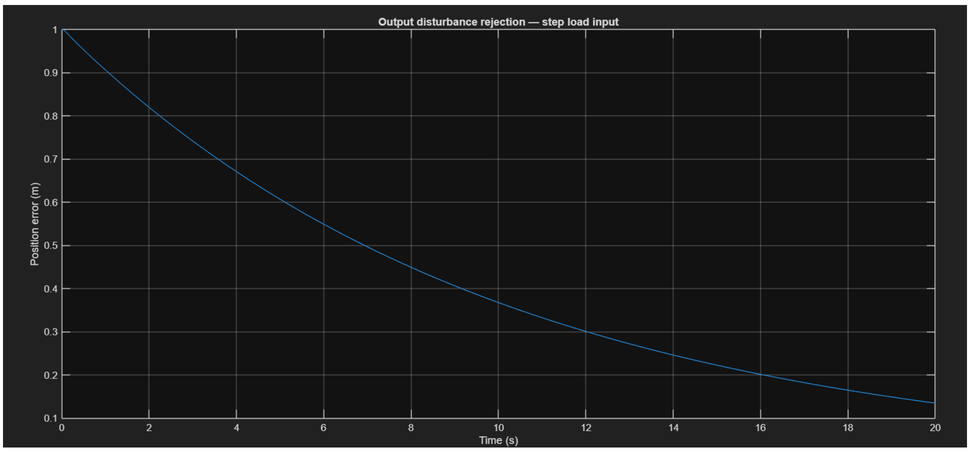

Figure 11.11: Position error response to a step load disturbance applied to the outer loop. The integrator in the inner loop drives steady-state error to zero within approximately 8–10 s, confirming effective disturbance rejection under the shaft model.

11.5 Discretisation

Figure B.12 — Continuous vs Discrete Step Response

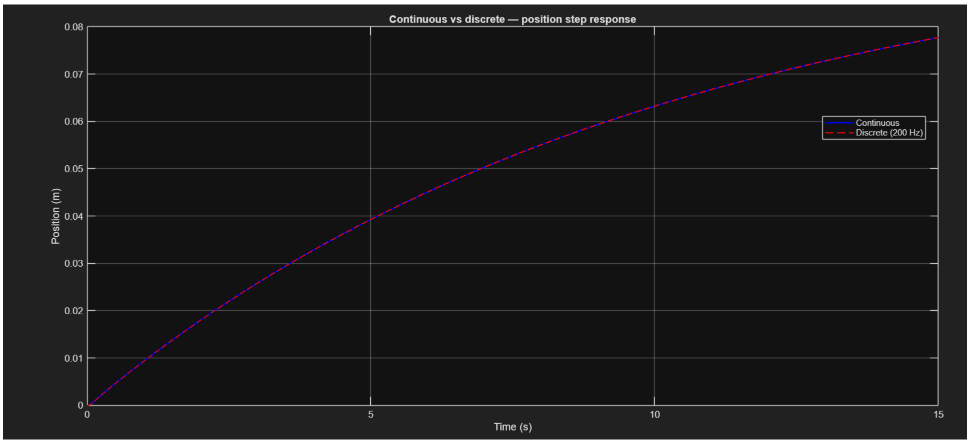

Figure 11.12: Comparison of continuous-time (solid blue) and discrete-time at 200 Hz (dashed red staircase) outer loop step responses. The near-identical responses confirm that the Tustin discretisation at 200 Hz introduces negligible distortion. The staircase shape of the discrete response reflects the zero-order hold behaviour of the digital implementation.

11.6 Outer Loop Gain Tuning (Physics Simulation)

Figure B.13 — Physics Simulation Interface

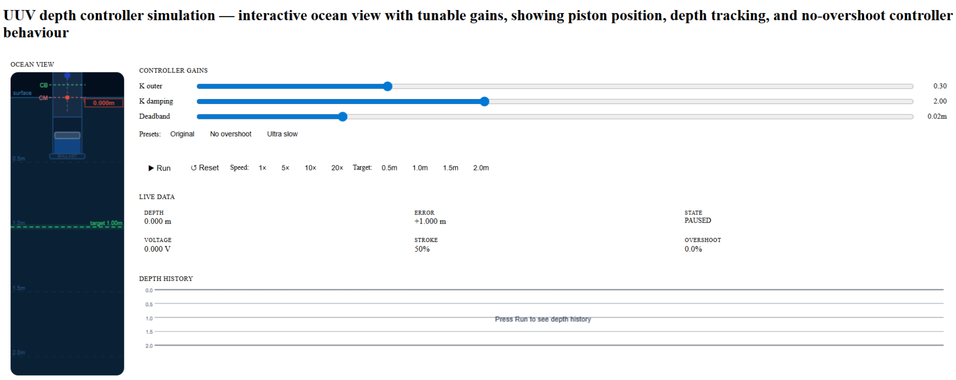

Figure 11.13: Full-physics simulation interface used for outer loop gain tuning. The display shows the animated AUV cylinder in the water column, the piston position indicator, depth history trace, and gain input fields. The simulation incorporates buoyancy force coupling, vehicle inertia (3 kg), water drag ($\zeta \approx 2.05$), and MS5837 sensor noise ($\sigma = 1$ mm).

Figure B.14 — Tuned Response ($K_{\text{outer}} = 0.1,\ K_D = 4.3$)

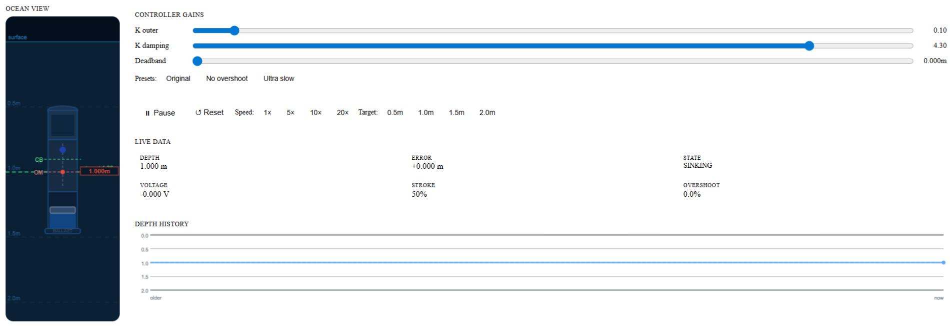

Figure 11.14: Depth response with the final tuned outer loop gains ($K_{\text{outer}} = 0.1$, $K_D = 4.3$). The vehicle converges monotonically to the 1.0 m target depth with zero overshoot. The depth rate filter (cutoff 2 rad/s) prevents the derivative term from amplifying sensor noise into the velocity command.

11.7 Python SIL Simulation Results

Figure B.15 — SIL Scenario 1: Clean Step Response

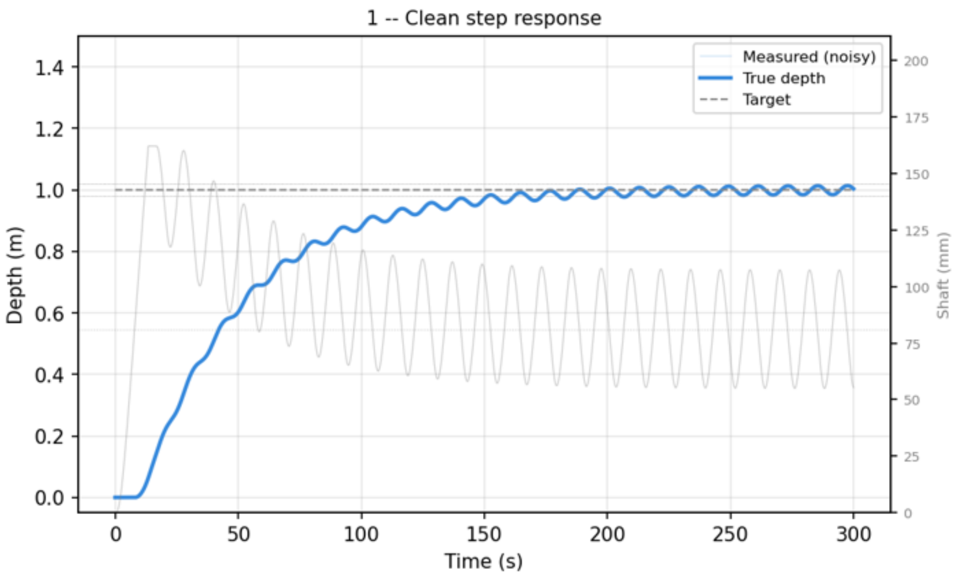

Figure 11.15: SIL Scenario 1 — clean step response. The faint trace shows the noisy simulated MS5837 reading ($\sigma = 1$ mm); the bold trace shows the true depth. The vehicle converges to 1.0 m with zero overshoot, steady-state error of 2.6 mm, and settling time of approximately 87 s. This provides evidence for ATP-2, ATP-3, ATP-4, and ATP-5

Figure B.16 — SIL Scenario 2: Load Disturbance at $t = 60$ s

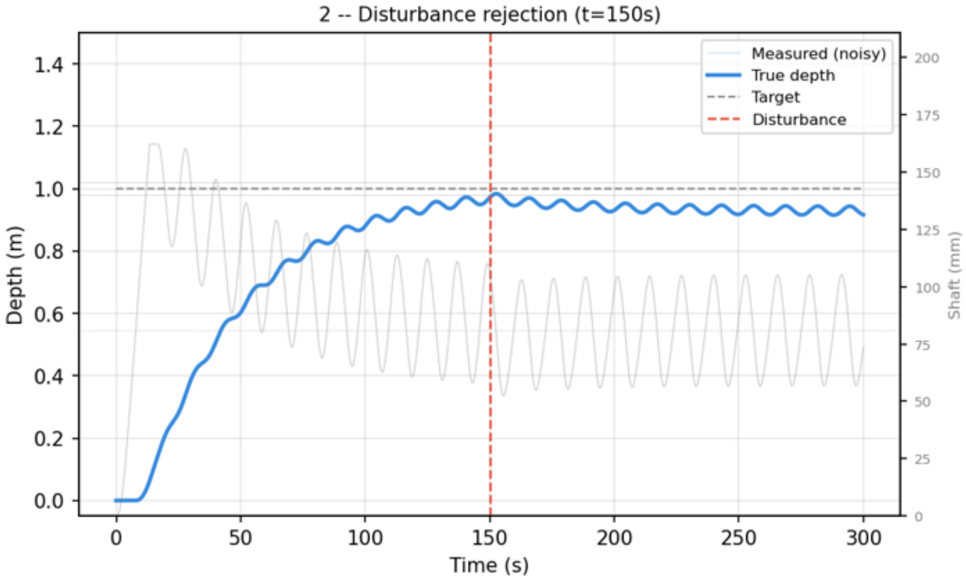

Figure 11.16: SIL Scenario 2 — 0.5 N constant load disturbance applied at $t = 60$ s. The vehicle remains stable with no oscillation or divergence after the disturbance (passing ATP-6), but settles with a residual 70 mm depth offset due to the PD outer loop structure. This is the qualified result discussed in Section 6.3. Evidence for ATP-6 (disturbance rejection).

Figure B.17 — SIL Scenario 3: Sensor Noise Only

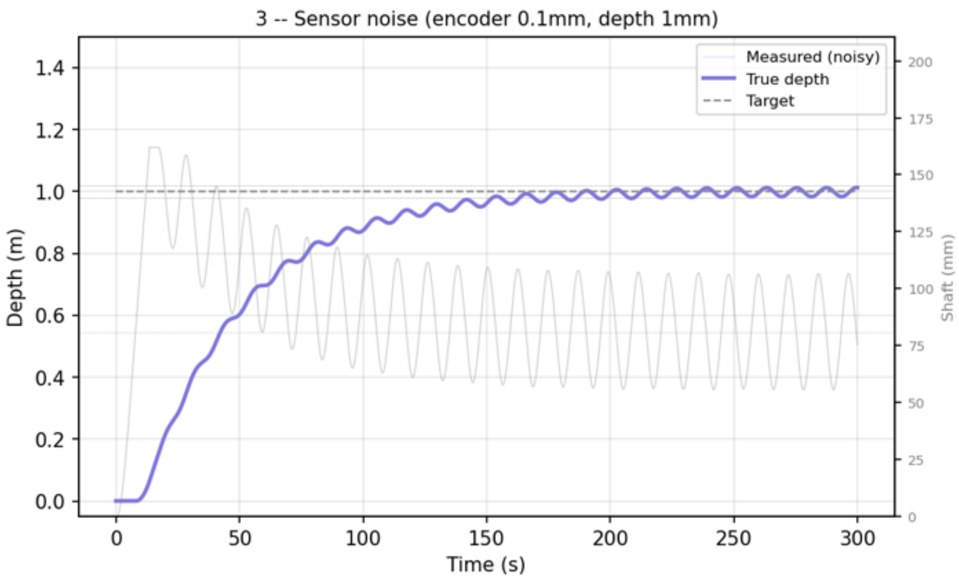

Figure 11.17: SIL Scenario 3 — MS5837 noise ($\sigma = 1$ mm) applied with no load disturbance. The true depth (bold) converges cleanly to 1.0 m with a steady-state error of 3.1 mm despite the clearly visible noisy measurement trace. This confirms the depth rate filter (cutoff 2 rad/s, $\alpha = 0.990$) successfully prevents noise from propagating into the velocity command. Evidence for ATP-7 (noise rejection).

Figure B.18 — SIL Scenario 4: Combined Noise and Disturbance

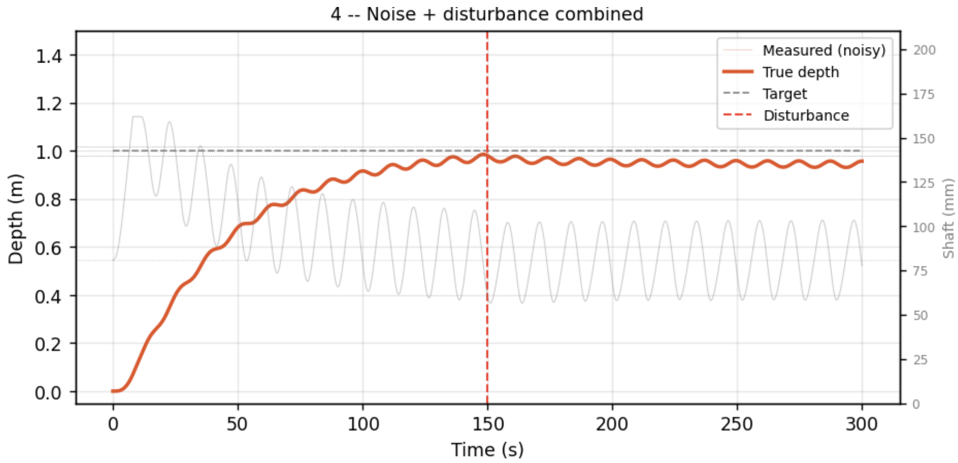

Figure 11.18: SIL Scenario 4 — combined sensor noise and load disturbance. The depth response remains monotonic with zero overshoot, confirming that the controller does not oscillate or diverge under worst-case combined conditions. A steady-state depth error of approximately 55 mm is observed, consistent with the proportional-only outer loop behaviour documented in ATP-6: a persistent depth error is required to sustain the corrective velocity command against the constant voltage disturbance. The noise contribution does not add meaningfully to the steady-state error, as the 2 rad/s low-pass filter on the depth rate estimate attenuates the MS5837 noise before it reaches the derivative term. Brief velocity reference spikes are visible in the inner loop signal but are suppressed by the velocity ceiling clamp and do not propagate to the depth response.

11.8 Equation Derivations

11.8.1 Screw Geometry: Lead and Screw Gain K_s

The lead of a screw thread is the linear distance travelled per one full revolution of the shaft. For a screw with lead angle θ_L and mean diameter D, the lead is derived from the geometry of the helical thread unwrapped into a right-angled triangle:

$$\text{Lead} = \pi D \tan(\theta_L) \tag{11.1}$$

Substituting the physical parameters of the screw jack ($\theta_L = 10°$, $D = 0.025$ m):

$$\begin{aligned}\text{Lead} &= \pi \times 0.025 \times \tan(10°)\\ &= \pi \times 0.025 \times 0.17633\\ &= 0.013849 \text{ m/rev} \quad (13.849 \text{ mm/rev})\end{aligned} \tag{11.2}$$

The screw gain K_s converts angular shaft velocity (rad/s) to linear piston velocity (m/s). Since one full revolution corresponds to 2π radians of shaft rotation and one lead of linear travel:

$$K_s = \frac{\text{Lead}}{2\pi} = \frac{0.013849}{2\pi} = \boxed{0.002204 \text{ m/rad}} \tag{11.3}$$

This value appears in the inner loop plant transfer function as the linear scaling factor between motor shaft angular velocity and piston linear velocity.

11.8.2 Current Limit to Voltage Ceiling

The DC motor armature current is governed by Kirchhoff's voltage law applied to the armature circuit:

$$V = E_b + I_a R_a + L_a \frac{dI_a}{dt} \tag{11.4}$$

where V is the applied voltage, $E_b = K_e\omega$ is the back-EMF, I_a is the armature current, R_a is the armature resistance, and L_a is the armature inductance. At the worst-case condition for current draw — stall, where $\omega = 0$ so $E_b = 0$ — and in steady state ($dI_a/dt = 0$), this reduces to:

$$I_{\text{stall}} = \frac{V}{R_a} \tag{11.5}$$

With $V = 12$ V and $R_a = 0.714\ \Omega$:

$$I_{\text{stall}} = \frac{12}{0.714} = 16.8 \text{ A} \tag{11.6}$$

This greatly exceeds the 3 A continuous current limit of the BTS7960. The maximum safe voltage V_{safe} that keeps stall current at or below $I_{\text{limit}} = 3$ A is:

$$V_{\text{safe}} = I_{\text{limit}} \times R_a = 3.0 \times 0.714 = \boxed{2.142 \text{ V}} \tag{11.7}$$

The controller output is clamped to ± 2.142 V in software, ensuring the motor current cannot exceed 3 A regardless of the magnitude of the depth error.

11.8.3 Maximum Stroke Velocity from Physical Measurement

The maximum linear velocity of the piston was determined empirically: the piston was observed to travel the full stroke $x_{\text{stroke}} = 162$ mm in $t = 11$ s at a depth of approximately 3 m, where water pressure loading is greatest within the proof-of-concept operating range. The worst-case maximum velocity is:

$$v_{\max} = \frac{x_{\text{stroke}}}{t_{\text{full stroke}}} = \frac{0.162 \text{ m}}{11 \text{ s}} = \boxed{0.01473 \text{ m/s}} \quad (14.73 \text{ mm/s}) \tag{11.8}$$

This value is used as the velocity ceiling in the control loop. The outer loop velocity reference v_{ref} is clamped to $\pm v_{\max}$ before being passed to the inner loop, preventing the controller from commanding physically unrealisable velocities and avoiding integrator windup. The measurement at 3 m depth is conservative: at shallower depths the water pressure load is lower and the piston moves faster, so the 3 m measurement provides a safe ceiling across the full 0–2 m operating range.

11.8.4 sisotool Gain Conversion: Time-Constant Form to Pole-Zero Form

MATLAB's sisotool expresses compensators in time-constant form:

$$C(s) = K \cdot \frac{1 + \tau_z s}{s(1 + \tau_p s)} \tag{11.9}$$

where $\tau_z = 1/z$ and $\tau_p = 1/p$ are the time constants of the zero and pole respectively. The inner loop compensator obtained from sisotool was:

$$C(s) = 75 \cdot \frac{1 + 0.25s}{s(1 + 0.02s)} \tag{11.10}$$

with $K = 75$, $\tau_z = 0.25$ s (zero at $s = -4$ rad/s), and $\tau_p = 0.02$ s (pole at $s = -50$ rad/s). For implementation in MATLAB code and the discrete difference equation, this must be expressed in pole-zero form:

$$C(s) = K_{\mathrm{pz}} \cdot \frac{s + z}{s(s + p)} \tag{11.11}$$

Expanding each factor in the time-constant form:

$$(1 + \tau_z s) = \tau_z \left(\frac{1}{\tau_z} + s \right) = \tau_z (s + z) \tag{11.12}$$

$$(1 + \tau_p s) = \tau_p \left(\frac{1}{\tau_p} + s \right) = \tau_p (s + p) \tag{11.13}$$

Substituting back:

$$C(s) = K \cdot \frac{\tau_z (s + z)}{s \cdot \tau_p (s + p)} = K \cdot \frac{\tau_z}{\tau_p} \cdot \frac{s + z}{s(s + p)} \tag{11.14}$$

Therefore the pole-zero gain is:

$$K_{\mathrm{pz}} = K \cdot \frac{\tau_z}{\tau_p} = K \cdot \frac{p}{z} \tag{11.15}$$

Substituting the numerical values ($K = 75$, $p = 50$, $z = 4$):

$$K_{\mathrm{pz}} = 75 \times \frac{50}{4} = 75 \times 12.5 = \boxed{937.5} \tag{11.16}$$

The final pole-zero form of the inner loop compensator is therefore:

$$C_{\text{inner}}(s) = \frac{937.5(s+4)}{s(s+50)} \tag{11.17}$$

Using the sisotool gain $K = 75$ directly in the pole-zero expression without this conversion would produce a compensator with 12.5$\times$ less loop gain, reducing the inner loop bandwidth from 21.53 rad/s to approximately 1.7 rad/s and completely altering the designed stability margins.

Chapter 12

Appendix: Power Subsystem

12.1 Load Map and Load Characterisation

The load map summarises the voltage rails, operating modes, and current demands of the main AUV loads and supporting power electronics. It informs the power specifications by showing which rails require continuous supply, which loads can be switched, and which components introduce peak-current or supply-stability constraints.

Item	**Type**	$V_{\textbf{Supply}}$ **[V]**	$I_{\textbf{Sleep}}$ **[mA]**	$I_{\textbf{Active}}$ **[mA]**	$I_{\textbf{Peak}}$ **[A]**
RS PRO DC motor	Load	7.2	0	5250	11.2
BTS7960 driver	Supporting	6–27; 3.3–5	-	Motor-set	43
XL6009, 7.2 V rail	Supporting	5–32; 7.2 out	0.07–0.10	2.5–5	4
LM7805 regulator	Supporting	≥7.5; 5 out	-	6–8	1.5

Table 12.1: Motor power: loads and supporting electronics.

Notes: The motor active current is its rated current and the peak current is the stall current. The BTS7960 current is set by the motor load; its peak value is the rated current path capability. The XL6009 peak value is the switch-current limit, not a guaranteed output current [79, 80, 81, 82].

Item	**Type**	$V_{\textbf{Supply}}$ **[V]**	$I_{\textbf{Sleep}}$ **[mA]**	$I_{\textbf{Active}}$ **[mA]**	$I_{\textbf{Peak}}$ **[mA]**
Raspberry Pi Pico	Load	5; 3.3 I/O	1.3	86.5	91.6
MS5837 depth sensor	Load	3.3	0.0001	0.00063–0.0201	1.25
AS5600 position sensor	Load	3.3	1.5	6.5	100
LM2596S, 3.3 V rail	Supporting	3.2–40; 3.3 out	-	Eq. (12.1)	≤3000

Table 12.2: Control power: loads and supporting electronics.

$$I_{\text{in,active}} \approx \frac{3.3 \sum I_{\text{Active,3V3}}}{\eta V_{\text{in}}}, \qquad \eta \leq 0.92 \tag{12.1}$$

Notes: The Pico current values are typical datasheet values. The AS5600 peak value is for OTP programming only and is not expected during normal deployment. The LM2596S current depends on the total load connected to the 3.3 V rail [83, 84, 85, 86].

Item	**Type**	$V_{\mathbf{Supply}}$ **[V]**	$I_{\mathbf{Sleep}}$ **[mA]**	$I_{\mathbf{Active}}$ **[mA]**	$I_{\mathbf{Peak}}$ **[mA]**
ECO FLNTU sensor	Load	10	0.14	60	60
TRN100 NTC sensor	Load	3.3	0	0.165	0.32
CD-PA1010D GNSS	Load	3.3	0.015	28	36
MAX3232 converter	Supporting	3.3 or 5	-	0.3	-
XL6009, 12 V rail	Supporting	5–32; 12 out	0.07–0.10	2.5–5	4000

Table 12.3: Research instrument power: loads and supporting electronics.

Source note: Research instrument load values are taken from the ECO FLNTU, TRN100 NTC, CD-PA1010D GNSS, MAX3232, and XL6009 datasheets [87, 88, 89, 90, 81].

Sensitive-load note: The CD-PA1010D GNSS module is treated as the most ripple-sensitive load on the 3.3 V rail. Its supply must remain within 3.0 V to 4.3 V, with operation supply ripple kept below 50 mVpp [89].

Measurement-sensitivity note: On the main rail, the INA226 is treated as the main measurement-sensitive device. Its current and power readings depend on microvolt-level shunt measurements, with a shunt-voltage LSB of 2.5 µV and maximum shunt offset of 10 µV. Its supply must remain within 2.7 V to 5.5 V, while the monitored bus voltage must remain within the 0 V to 36 V sensing range [91].

12.2 Energy Source and Battery Topology Support

12.2.1 18650 Cell-Level Justification

The selected 18650 cell has the key datasheet values shown in Table 12.4 [1].

Parameter	Value	Design relevance
Nominal voltage	3.7 V	Enables modular series pack construction.
Capacity	2.6 Ah	Sets runtime per parallel row.
Energy	9.62 Wh	Used for pack energy calculations.
Mass	45 g	Supports compact, mass-limited packaging.
Internal resistance	$\leq 60\,\mathrm{m\Omega}$	Affects voltage sag under high current.
Maximum discharge current	$1.5\,\mathrm{C} = 3.9\,\mathrm{A}$	Sets current capability per parallel row.
Cycle life	> 500 cycles at 80% DOD	Supports repeated prototype use.
Discharge temperature range	$-20\,°\mathrm{C}$ to $60\,°\mathrm{C}$	Supports cold deployment, with derating.

Table 12.4: Key datasheet values for the selected 18650 Li-ion cell.

Energy density

$$\text{Energy density} = \frac{9.62\,\mathrm{Wh}}{0.045\,\mathrm{kg}} = 213.8\,\mathrm{Wh/kg} \approx 214\,\mathrm{Wh/kg}$$

Therefore, each cell provides approximately 214 Wh/kg.

Cost per stored energy

$$\text{Cost per Wh} = \frac{\mathrm{R95}}{9.62\,\mathrm{Wh}} = \mathrm{R9.88/Wh}$$

Maximum discharge current

$$I_{\text{max}} = 1.5C \times 2.6\,\mathrm{Ah} = 3.9\,\mathrm{A}$$

Pack parallel rows	Maximum discharge current
1P	3.9 A
2P	7.8 A
3P	11.7 A

Table 12.5: Discharge current scaling with added parallel rows.

A 1P pack is close to the prototype's maximum current condition, while a 2P pack provides stronger current margin for simultaneous loading.

12.2.2 3S vs 2S Topology Comparison

Pack energy, mass, cost, and current capability

Pack	Cells	Nominal voltage	Capacity	Energy	Mass	Cost	Max current
2S1P	2	7.4 V	2.6 Ah	19.24 Wh	90 g	R190	3.9 A
3S1P	3	11.1 V	2.6 Ah	28.86 Wh	135 g	R285	3.9 A
2S2P	4	7.4 V	5.2 Ah	38.48 Wh	180 g	R380	7.8 A
3S2P	6	11.1 V	5.2 Ah	57.72 Wh	270 g	R570	7.8 A

Table 12.6: Pack-level comparison of 2S and 3S Li-ion configurations.

The same cell is used in both configurations, so the current capability per parallel row is the same. The difference is that 3S provides a higher pack voltage and more stored energy per row [1].

Parallel expansion

Added parallel row	Added cells	Added energy	Added current capacity
Add one 2S row	2 cells	19.24 Wh	+3.9 A
Add one 3S row	3 cells	28.86 Wh	+3.9 A

Table 12.7: Effect of adding one parallel row to each topology.

Both configurations gain the same current capacity when a parallel row is added. However, each added 3S row contributes more energy and maintains the higher system voltage.

Response to most power-intensive prototype load

The most power-intensive prototype load is the motor rail. It was agreed that the prototype motor would operate at $\leq 3\,\mathrm{A}$, so the maximum motor load is:

$$P_{\text{motor}} = 7.2\,\mathrm{V} \times 3\,\mathrm{A} = 21.6\,\mathrm{W}$$

Battery-side current is estimated using:

$$I_{\text{in}} = \frac{P_{\text{out}}}{\eta V_{\text{in}}}$$

The planning efficiencies are used to reflect the different conversion conditions. The 2S case uses a lower estimate because it operates from a lower input voltage and must supply the same output power at higher input current. The 3S case uses a higher estimate because the higher input voltage reduces battery-side current and converter stress.

Pack	**Input voltage used**	**Planning efficiency**	**Battery current for** 21.6 W
2S	6.0 V	85%	4.24 A
3S	9.0 V	90%	2.67 A

Table 12.8: Battery-side current required to support the most power-intensive prototype load.

A 2S1P pack exceeds the 3.9 A maximum cell discharge rating under the most power-intensive prototype load before any other loads are considered. A 3S1P pack remains within the 3.9 A rating, while a 3S2P pack gives additional current margin.

Even if the same efficiency is assumed for both configurations, 3S still draws less battery current because its input voltage is higher.

Efficiency assumption	**2S battery current**	**3S battery current**
Both at 85%	4.24 A	2.82 A
Both at 90%	4.00 A	2.67 A

Table 12.9: Battery-side current comparison under equal efficiency assumptions.

Cold-energy derating

The datasheet temperature curve shows that cold operation reduces usable voltage and capacity. For conservative planning, a 50% usable-energy derating can be applied [1].

Pack	**Nominal energy**	**50% cold-derated usable energy**
2S1P	19.24 Wh	9.62 Wh
3S1P	28.86 Wh	14.43 Wh
2S2P	38.48 Wh	19.24 Wh
3S2P	57.72 Wh	28.86 Wh

Table 12.10: Conservative cold-energy derating comparison for 2S and 3S configurations.

This strengthens the 3S decision: under cold derating, 3S retains more usable energy while also reducing battery-side current for the same high-power load.

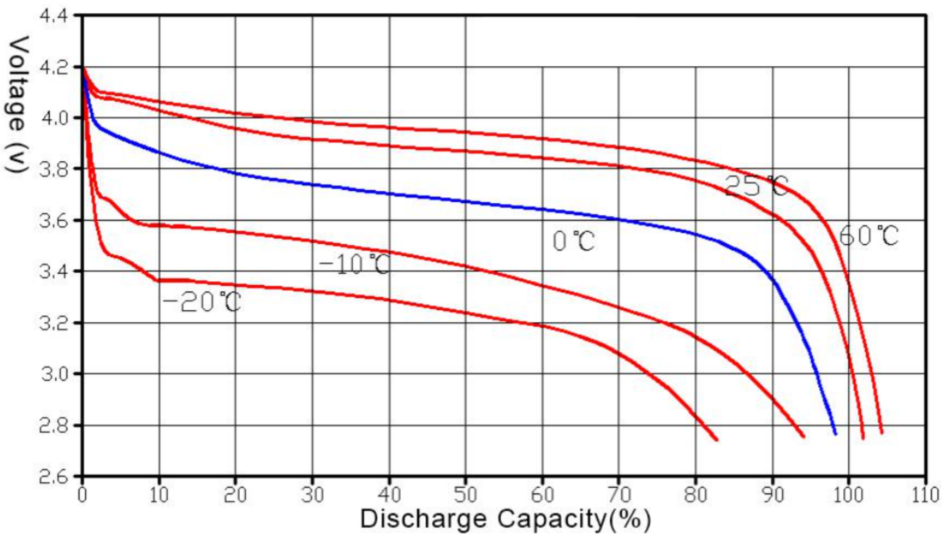

Figure 12.1: Different-temperature discharge curve for the selected 18650 cell. Cold operation reduces terminal voltage and usable capacity [1].

12.3 Motor Driver Selection Support

Criterion	**L298N**	**BTS7960**	**Design implication**
Current capability	2 A peak module rating	43 A peak module rating	The L298N is below the $\leq$ 3 A prototype motor limit and cannot accommodate the estimated 11.2 A stall current. The BTS7960 has sufficient current margin.
Motor supply range	5 V–35 V module supply	6 V–27 V module supply	Both support the 7.2 V motor rail.
Loss mechanism	Bipolar transistor saturation voltage	MOSFET on-resistance	The L298N loses voltage across its output stage. The BTS7960 mainly loses power through I^2R conduction loss.
Estimated running loss	Using the 2 A datasheet drop: $$P_{\text{loss}} \approx 4.9 \times 2 = 9.8\,\text{W}$$	Assuming two conducting MOSFET paths: $$R_{\text{path}} \approx 2(16\,m\Omega) = 32\,\text{m}\Omega$$ $$P_{\text{loss}} = 3^2(0.032) = 0.29\,\text{W}$$	The L298N would waste a large fraction of the motor rail power as heat. The BTS7960 is much more efficient at the prototype running current.
Estimated stall loss	Not suitable for 11.2 A stall current	$$P_{\text{loss}} = 11.2^2(0.032) \approx 4.0\,\text{W}$$	The BTS7960 can tolerate short high-current events with much better thermal margin.
Protection	Protection diodes and over-temperature protection	Over-voltage, under-voltage, over-current, short-circuit and over-temperature protection; diagnosis/current sense	The BTS7960 gives stronger protection for the highest-power load.

Table 12.11: Comparison of L298N and BTS7960 motor drivers for the prototype motor rail [92, 80].

12.4 Final Power Subsystem Architecture

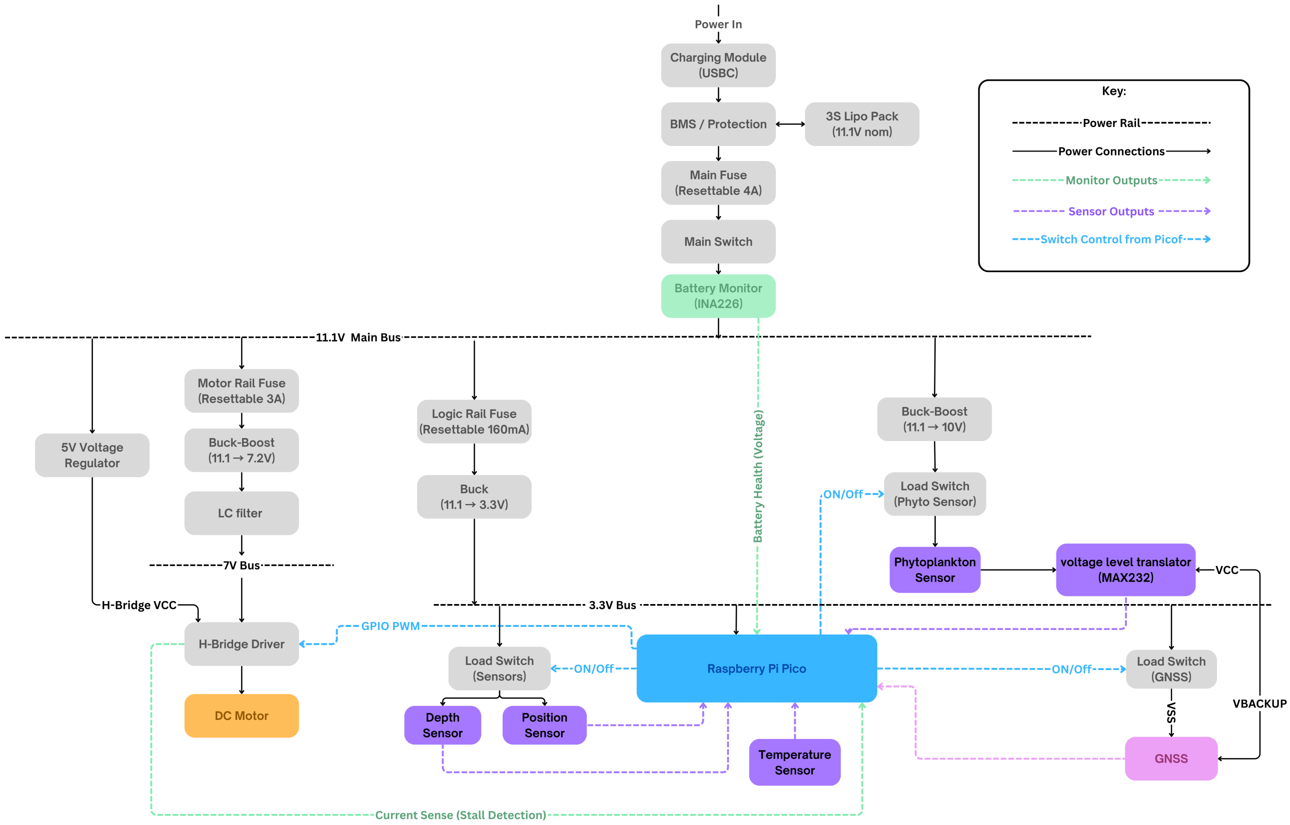

Figure 12.2: Final power subsystem architecture.

Table 12.12: Final design component summary.

Subsystem	Final design components and function
Power Source and Protection	• **LiPo Charger Boost Board 3S 2A:** Provides the USB-C charging interface for the 3S lithium battery pack and regulates charging up to approximately 12.6 V. • **3S lithium BMS balance charger/protection board:** Provides cell balancing and battery protection, including overcharge, over-discharge, short-circuit, and fault protection. • 4 A **main resettable fuse:** Provides upstream overcurrent protection for the full power subsystem. • **KCD8 main switch:** Provides a physical hard-disconnect between the battery and the rest of the system. • **INA226 voltage monitor:** Monitors battery voltage only through VBUS so that the Pico can detect low-battery conditions and enter sleep mode [91].
Motor Power Delivery	• 3 A **motor resettable fuse:** Protects the motor branch from sustained overcurrent. • **Adjustable buck converter module:** Regulates the 3S battery voltage to the required 7.2 V motor rail [81]. • 5 V **regulator module:** Provides the required logic supply for the BTS7960 motor driver [82]. • **LC filter:** Reduces motor-rail ripple and motor-generated noise before the H-bridge stage. • **BTS7960 motor driver:** Provides bidirectional motor control using PWM and logic control signals from the Pico [80].
3.3 V Regulated Rail	• 160 mA **resettable fuse:** Provides branch-level protection for the low-power logic rail. • **LM2596 adjustable buck converter module:** Steps the 3S battery voltage down to a stable 3.3 V rail for control electronics, sensor interfaces, and load-switch control [86].
Control System Power Delivery	• 3.3 V **sensor load switch:** Allows the low-voltage sensor supply to be disconnected during sleep or inactive modes. • 3.3 V **GNSS load switch:** Allows the GNSS module to be powered only during location acquisition. • 10 V **phytoplankton sensor load switch:** Allows the phytoplankton sensor supply to be enabled only during measurement periods.
Research Instrument Power Delivery	• **LTC3780 automatic buck-boost converter module:** Regulates the 3S battery voltage to a stable 10 V supply for the phytoplankton sensor [93]. • **MAX3232 RS232-to-TTL level translator:** Converts the phytoplankton sensor communication signals to 3.3 V UART-compatible logic levels for the Pico [90].

12.4.1 Load-Switch Circuit Justification

The external load switches use a high-side PMOS configuration, where the PMOS source is connected to the supply input and the drain is connected to the switched load output [72]. This was selected instead of low-side switching because the external modules share signal references with the controller. Switching the positive supply keeps the load ground common, avoids ground-lift errors on sensor and communication lines, and reduces the risk of back-powering modules through GPIO, UART, or sensor interface pins.

The PMOS gate is pulled up to its source through a 220 kΩ resistor, making the switch default to the off state when the controller is inactive. The 2N7000 NMOS pulls the PMOS gate low when the control signal is asserted, turning the PMOS on [73]. A 220 kΩ pull-down is placed at the NMOS gate so that the switch remains off while the controller pin is floating during reset or start-up. The 2.2 kΩ resistors limit gate-drive current, reduce switching transients, and protect the controller pin, while remaining small compared with the 220 kΩ pull-up so that the PMOS gate can still be pulled close to ground during turn-on.

For the on state, the PMOS gate-to-source voltage is approximated as

$$V_{GS,P} \approx -V_{\text{load}} \left(\frac{R_{\text{PU}}}{R_{\text{PU}} + R_{\text{G}}} \right),$$

where $R_{\text{PU}} = 220\,\text{k}\Omega$ and $R_{\text{G}} = 2.2\,\text{k}\Omega$. Therefore,

$$V_{GS,P} \approx -0.99 V_{\text{load}}.$$

At 3.3 V,

$$V_{GS,P} \approx -3.27\,\text{V},$$

while at 10 V,

$$V_{GS,P} \approx -9.90\,\text{V}.$$

The 10 V case is close to the datasheet condition used for the IRF9530N's quoted on-resistance. The 3.3 V case is more uncertain because the device is not guaranteed to be fully enhanced at this gate voltage. Therefore, the 3.3 V GNSS, depth-sensor, and position-sensor cases require sensitivity testing to confirm that the voltage drop across the PMOS remains acceptable.

Placeholder for IRF9530N datasheet I_D graph.

Insert the typical output or transfer characteristics showing drain current dependence on V_{GS}.

Figure 12.3: IRF9530N drain-current characteristics used to assess the marginal 3.3 V gate-drive case.

The IRF9530N is rated for a drain-source voltage of −100 V, a continuous drain current of −14 A at 25 °C, and a maximum gate-source voltage of ±20 V [72]. These ratings are well above the load-switch operating range, so the limiting factor is not the absolute voltage or current rating. The critical concern is instead whether the PMOS conducts strongly enough with the available 3.3 V gate drive.

Load case	**Nominal voltage**	**Load current**	**Equivalent LTspice load**
GNSS	3.3 V	mA	$R = 3.3/I_{\text{GNSS}}$
Depth sensor	3.3 V	mA	$R = 3.3/I_{\text{depth}}$
Position sensor	3.3 V	mA	$R = 3.3/I_{\text{position}}$

Table 12.13: Load cases used to assess the 3.3 V high-side switch behaviour.

The 2N7000 NMOS is only used as a gate-pull-down device, not as the main load-current path [73]. Its current is therefore limited mainly to the PMOS gate-bias path:

$$I_{\text{bias,on}} \approx \frac{V_{\text{load}}}{220\,\text{k}\Omega + 2.2\,\text{k}\Omega}.$$

Thus,

$$I_{\text{bias,on}}(3.3\,\text{V}) \approx 14.9\,\mu\text{A}, \qquad I_{\text{bias,on}}(10\,\text{V}) \approx 45.0\,\mu\text{A}.$$

This is far below the 2N7000 current capability, so the NMOS is suitable as a gate driver. Its role is not to carry the external load current, but only to sink the small PMOS gate-bias current during turn-on.

For a ±5% 3.3 V rail tolerance, the minimum acceptable switched output voltage is

$$V_{\text{out,min}} = 0.95(3.3) = 3.135\,\text{V}.$$

Therefore, the maximum acceptable voltage drop across the PMOS at the nominal 3.3 V input is

$$V_{\text{drop,max}} = 3.3 - 3.135 = 165\,\text{mV}.$$

If the voltage drop exceeds this limit, the IRF9530N is not suitable for the 3.3 V switched loads and should be replaced with a logic-level PMOS specified at $V_{GS} = -2.5\,\text{V}$ or $V_{GS} = -3.3\,\text{V}$.

Chapter 13

Appendix: Housing Subsystem

13.1 Buoyancy and Mass Balance Calculations

The housing's stability and buoyancy behaviour were determined from a static mass-balance analysis combined with Archimedes' principle. This appendix documents the full worked calculation that underpins the ballast sizing decision in Section 6.4.1. The reactive weight calculator (Figure 6.1) was used to iterate on ring geometry and verify the final configuration.

13.1.1 Component mass and centre of mass

Each subassembly is treated as a point mass located at its geometric centroid along the float's vertical axis (measured from the base of the external cylinder). The composite centre of mass is

$$z_{\mathrm{CM}} = \frac{\sum_i m_i z_i}{\sum_i m_i} \tag{13.1}$$

where m_i is the mass of component i and z_i is the height of its centroid above the base [94]. Table 13.1 lists the component mass budget used in the calculation.

Table 13.1: Mass budget for the assembled prototype (without ballast). Masses are slicer-derived for printed parts and datasheet/BOM values for all other components.

Component	**Mass** (g)	**Centroid** z_i (mm)
Service cap (PLA)	90	521
Electronics tube (PLA)	186	415
Electronics balancer (PLA)	18	415
Battery pack and electronics	380	415
Sensor-actuator tube (PLA)	490	213
ECO FLNTU sensor	400	279
TRN100 temperature sensor	35	279
MS5837 depth sensor	5	279
Motor, gearbox, and lead screw assembly	320	107
External cylinder (PLA)	484	100
Piston (at mid-stroke)	110	82
Fasteners, cables, hardware	113	—
Total (system without ballast)	**1631**	—

13.1.2 Centre of buoyancy

The centre of buoyancy is the centroid of the displaced water volume. For the float at full piston extension, the submerged volume comprises the external cylinder (open-bottom, piston extended) plus all sealed dry zones. Treating the submerged envelope as a stacked cylinder:

$$z_{\mathrm{CB}} = \frac{\sum_j V_j z_j}{\sum_j V_j} \tag{13.2}$$

where V_j is the displaced volume of zone j and z_j is the centroid height of that zone [95]. For the prototype configuration, $z_{\mathrm{CB}} \approx 303.5\,\mathrm{mm}$ above the base, equal to $L/2$ for the stacked cylindrical envelope.

13.1.3 Ballast sizing for stability margin

The CB–CM separation, expressed as a percentage of total float length $L = 528\,\mathrm{mm}$, must exceed the 5 % stability target (S3). Without ballast, z_{CM} from Equation 13.1 computes to approximately 279.3 mm, yielding a CB–CM separation of only 4.6 % — below the target. A ballast ring placed at the base of the float ($z_{\mathrm{ballast}} = 40\,\mathrm{mm}$) is required to lower z_{CM}.

The mass of the bolt-and-sand filled annular ring is calculated as:

$$m_{\mathrm{ballast}} = \frac{\pi}{4}\left(D_{\mathrm{o}}^2 - D_{\mathrm{i}}^2\right) h\, \rho_{\mathrm{fill}} \tag{13.3}$$

For $D_{\mathrm{o}} = 200\,\mathrm{mm}$, $D_{\mathrm{i}} = 126\,\mathrm{mm}$, $h = 80\,\mathrm{mm}$, and an effective fill density accounting for M10 hex bolts (720 g) and building sand ($1920\,\mathrm{kg\,m^{-3}}$) across the remaining groove volume, Equation 13.3 gives $m_{\mathrm{ballast}} = 3574\,\mathrm{g}$ [94].

Substituting into Equation 13.1 with the ballast included:

$$\begin{aligned} z_{\mathrm{CM}} &= \frac{m_{\mathrm{sys}} \cdot z_{\mathrm{sys}} + m_{\mathrm{ballast}} \cdot z_{\mathrm{ballast}}}{m_{\mathrm{sys}} + m_{\mathrm{ballast}}} \\ &= \frac{1631 \times 279.3 + 3574 \times 40.0}{1631 + 3574} = 115.0\,\mathrm{mm} \end{aligned} \tag{13.4}$$

giving a CB–CM separation of

$$\frac{z_{\mathrm{CB}} - z_{\mathrm{CM}}}{L} = \frac{303.5 - 115.0}{528} = 28.2\,\% \tag{13.5}$$

which far exceeds the 5 % target (S3) [11].

13.1.4 Net buoyancy across piston stroke

The net vertical force on the float is

$$F_{\text{net}} = \rho_{\text{water}}\, g\, V_{\text{disp}}(s) - m_{\text{total}}\, g \tag{13.6}$$

where $V_{\text{disp}}(s)$ is the displaced volume as a function of piston position s, and $m_{\text{total}} = 1.631\,\text{kg} + 3.574\,\text{kg} = 5.205\,\text{kg}$ [95]. Using saltwater density $\rho_{\text{sw}} = 1025\,\text{kg}\,\text{m}^{-3}$ and total displacement $V = \pi(0.06)^2 \times 0.528 = 5.972\,\text{L}$ at full piston extension:

$$\begin{aligned} F_{\text{buoy}} &= \rho_{\text{sw}} \cdot g \cdot V = 1025 \times 9.81 \times 0.005972 = 60.05\,\text{N} \\ W_{\text{total}} &= m_{\text{total}} \cdot g = 5.205 \times 9.81 = 51.06\,\text{N} \\ F_{\text{net}}^{\text{extended}} &= 60.05 - 51.06 = 27.56\,\text{N} \quad \text{(float ascends)} \end{aligned} \tag{13.7}$$

The float therefore retains net positive buoyancy across the full piston stroke, and uses piston position to control the *magnitude* of the ascent/descent force rather than the equilibrium depth [11]. The equilibrium piston position at neutral buoyancy is 43.2 mm from the base of the external cylinder (26 % of stroke).

13.1.5 Sensitivity analysis

To verify robustness against manufacturing tolerances and zone-height adjustments, the ballast ring outer diameter, height, and inner diameter were each swept across ±5 % of their nominal values, and zone heights were varied by ±10 mm. Across the full parameter sweep, the CB–CM separation remained well above the 5 % target (S3) in all cases, confirming the stability margin is robust to expected build variation.

13.2 Housing Dimensions

Table 13.2: Key dimensions of the final housing assembly.

Component	**Dimension**
Electronics tube (ID × height)	Ø120 mm × 115 mm
Sensor-actuator tube, upper (ID × height)	Ø140 mm × 150 mm
Sensor-actuator tube, lower (ID × height)	Ø161 mm × 63 mm
External wet cylinder (ID × height)	Ø120 mm × 200 mm
Piston outer diameter	Ø118 mm
Piston stroke	∼164 mm
Ballast ring (OD × ID × height)	Ø200 mm × Ø126 mm × 80 mm
System mass without ballast	1.63 kg
Ballast mass	∼3574 g
CB–CM separation	28.2 % of float length
Net buoyancy (piston extended)	27.56 N

13.3 FEA Stress and Displacement Diagrams

The following figures show the Von Mises stress and displacement magnitude results from the SimScale static FEA (finite element analysis) described in Section 6.5. Each component is presented as a row: Von Mises stress (left) and displacement magnitude (right). All simulations used PLA material properties ($E = 3.5\,\text{GPa}$, $\nu = 0.36$, $\sigma_y = 50\,\text{MPa}$) with an applied inward pressure of 19.62 kPa [21].

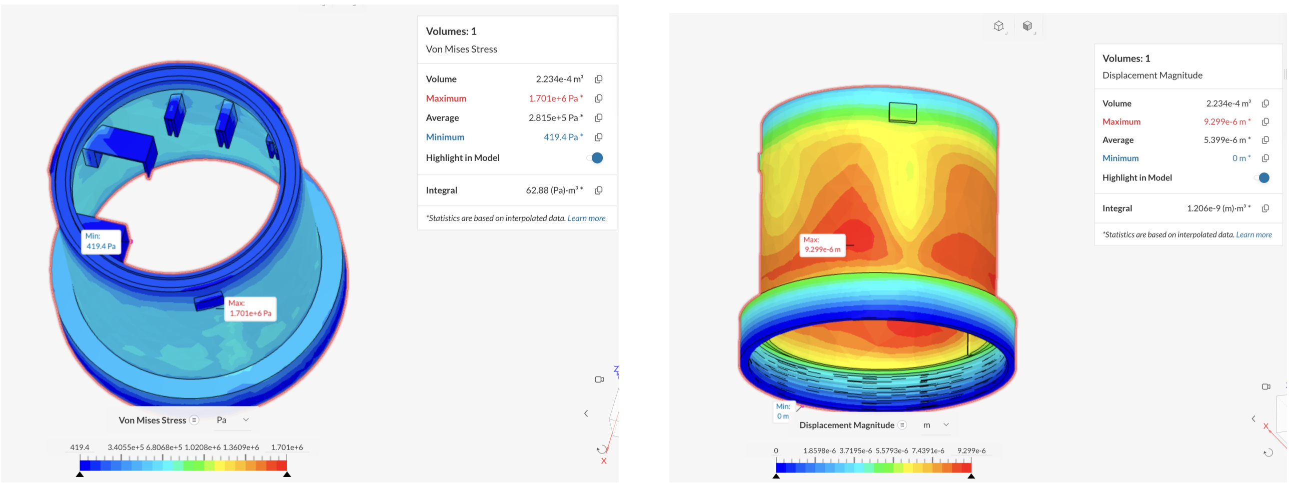

Figure 13.1: **Electronics tube.** Von Mises stress (left) and displacement magnitude (right). Max stress 1.70 MPa, max displacement 0.009 mm, safety factor 29.4. Peak stress localised at internal rail slots; cylindrical wall remains uniformly low stress.

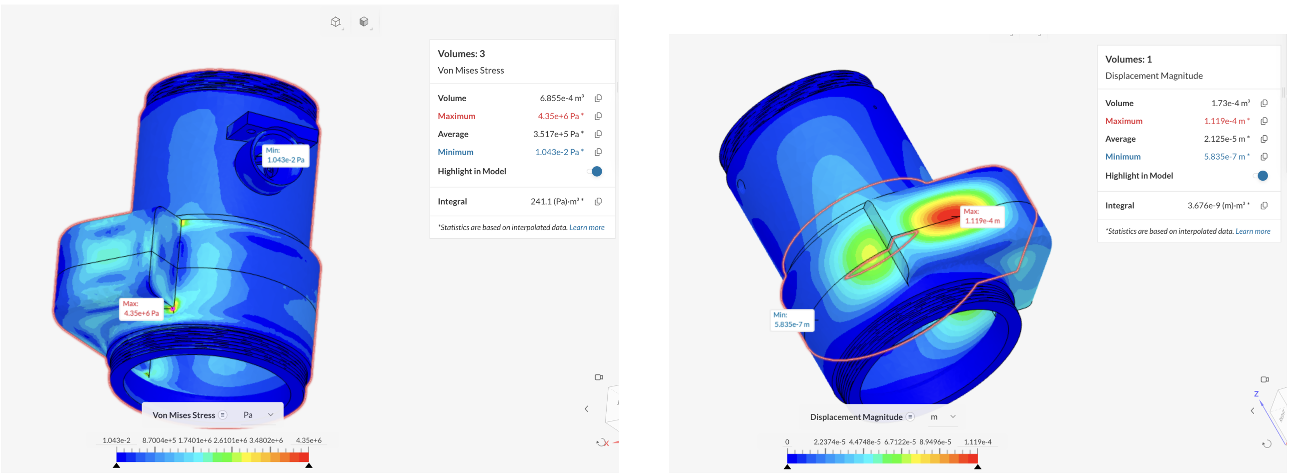

Figure 13.2: **Sensor-actuator zone.** Von Mises stress (left) and displacement magnitude (right). Max stress 4.35 MPa, max displacement 0.112 mm, safety factor 11.5. Peak stress concentrated at the ECO FLNTU L-bracket mounting recess; bulk wall stress remains below 1 MPa.

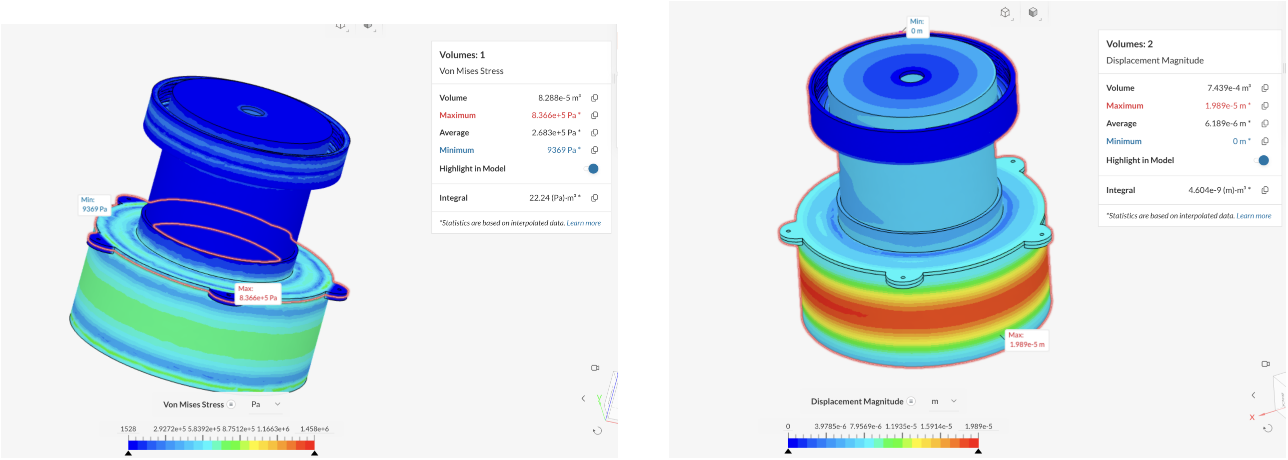

Figure 13.3: **External wet cylinder.** Von Mises stress (left) and displacement magnitude (right). Max stress 0.84 MPa, max displacement 0.020 mm, safety factor 59.7. Peak stress at the flange–cylinder transition, consistent with the analytical buckling safety factor of 4.8.

13.4 Housing Component CAD Renders

The following are renders of key structural components of the housing prototype. All parts were modelled in Autodesk Fusion and 3D printed in PLA using Prusa Mini and Bambu printers. For each component, the CAD render (left) and cross-section view (right) show internal features.

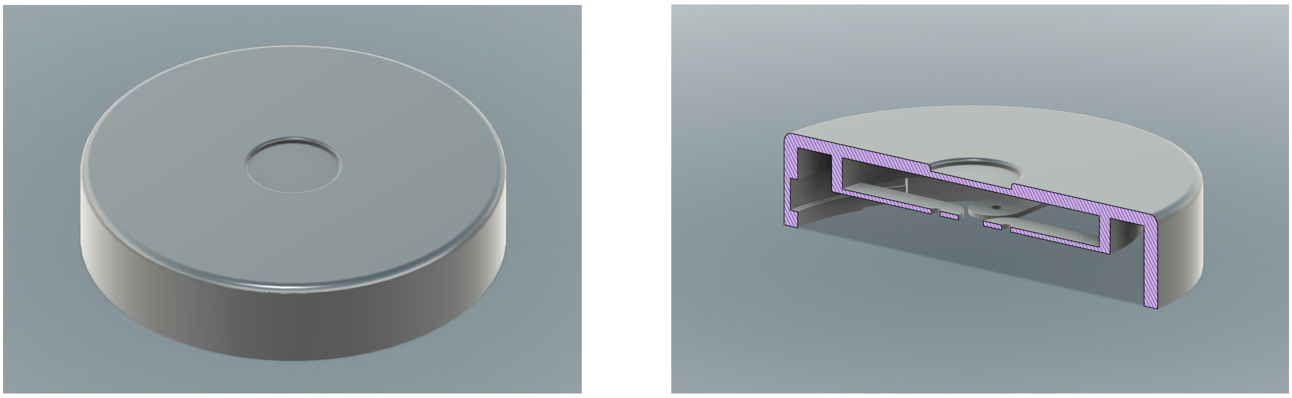

Figure 13.4: **Service Cap.** Forms the uppermost closure of the housing, interfacing with the electronics tube via a bayonet locking mechanism. A single NBR face O-ring provides the primary watertight barrier. The cross-section reveals the O-ring groove geometry and the recessed radome window [2] that accommodates an optional GNSS patch antenna [3] without penetrating the pressure boundary.

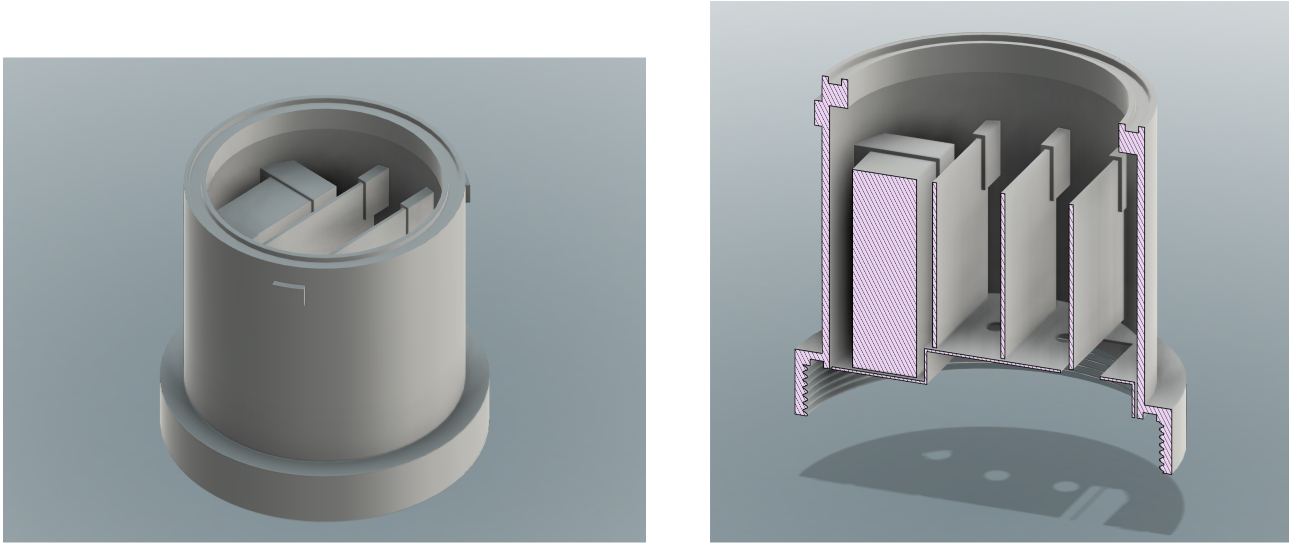

Figure 13.5: **Electronics Tube.** Houses the PCB, battery pack, and power regulation circuitry on a central mounting rail. Fully sealed from the adjacent sensor-actuator zone by a face seal. The cross-section shows the internal rail geometry and the balancer insert that aligns the PCB concentrically while contributing to the low centre-of-mass target.

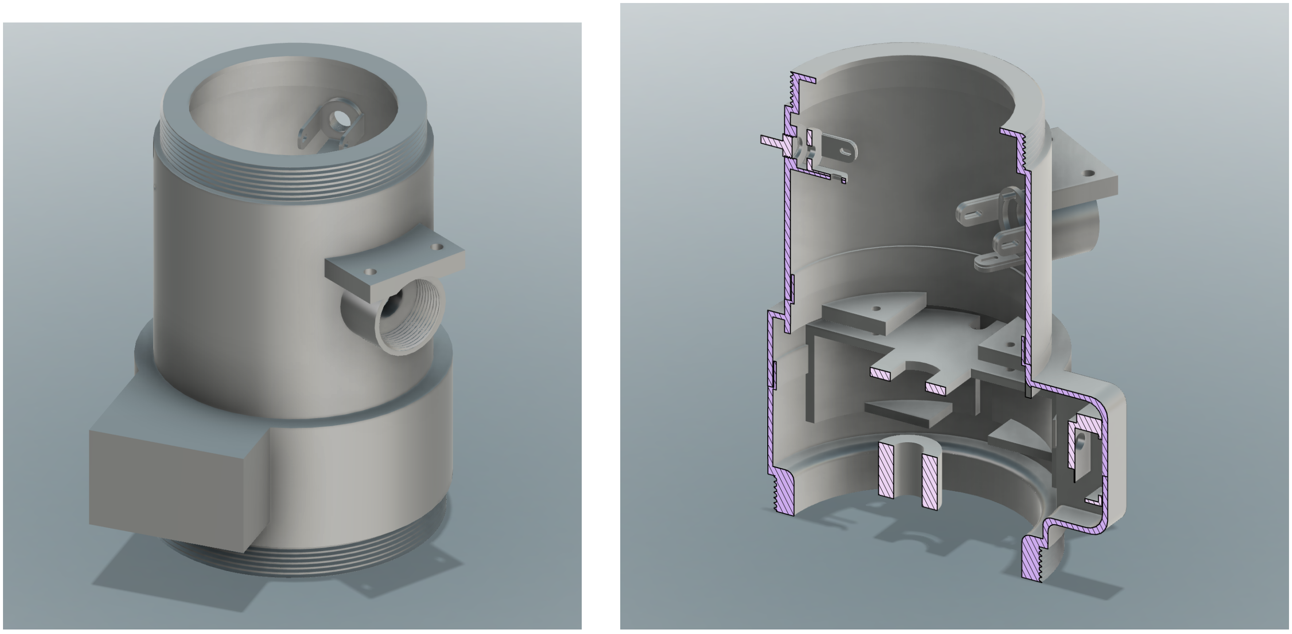

Figure 13.6: **Sensor-Actuator Zone.** Three-part assembly (top, middle, bottom) containing the motor, worm gearbox, lead screw, and piston. The cross-section shows the shaft seal stack at the mid-section where the lead screw exits the dry zone, and the motor mounting geometry at the base. The external sensor collar carrying the ECO FLNTU and TRN100 sensors mounts at the midsection.

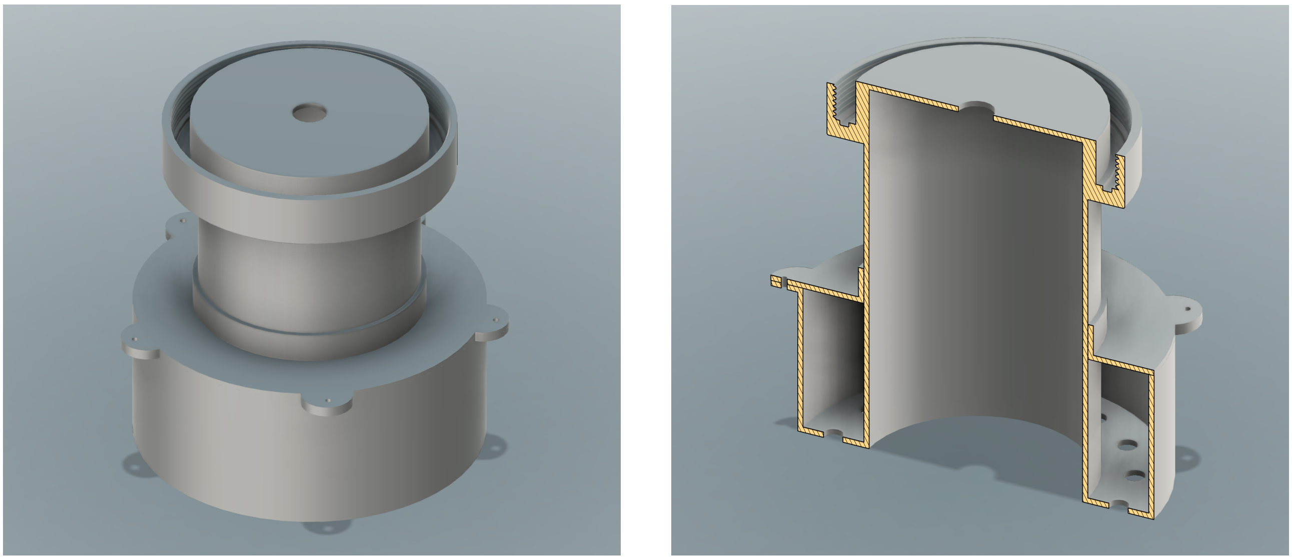

Figure 13.7: **External Cylinder and Piston.** Open-base PLA cylinder forming the variable-volume buoyancy chamber. The acetal piston travels the full 164 mm stroke to modulate net buoyancy force. The cross-section shows the dual NBR O-ring grooves in the piston head [2] that maintain the dynamic seal against the cylinder bore, and the sand-filled ballast shell fixed at the base to achieve the required CB–CM separation.

13.5 Acceptance Test Procedures

The following acceptance test procedures define the pass criteria for the housing subsystem. Each ATP maps to requirements from Section 6.3 and is written as a sequential procedure to allow independent reproduction.

ATP-H01 — Dimensional verification

Materials: Digital calipers, CAD nominal dimension sheet.

Procedure: Measure the electronics tube bore ID, face O-ring groove depth and width on both tube ends, and the MS5837 boss bore diameter after reaming. Record all values against nominal CAD dimensions.

Pass criterion: All dimensions within ±0.2 mm of nominal. O-ring groove depth and width within 5 % of the design target for a 74 % compression ratio on the 3.53 mm wire O-ring.

ATP-H02 — Dry assembly fit check

Materials: Assembled housing components, silicone grease.

Procedure: Engage threaded joint J1 (electronics tube to sensor-actuator tube) and joint J2 (sensor-actuator tube to external cylinder) by hand to full engagement. Seat the service cap via the bayonet lock and record the rotation angle to the positive stop. Insert the piston into the wet cylinder with O-rings and silicone grease applied and translate the full stroke manually in both directions.

Pass criterion: All joints reach full engagement without binding. Bayonet lock seats in under 90° rotation with a positive tactile stop. Piston travels the full ∼164 mm stroke without O-ring rollover or binding.

ATP-H03 — Static waterproofing

Materials: Fresh water tank (≥1.2 m depth), moisture indicator strip, fully assembled float.
Procedure: Place a moisture indicator strip inside the electronics tube. Seal the tube with the service cap and fit all three sensor penetrations. Lower the fully assembled float to 1 m depth and hold for 30 min, per the IPX7 immersion standard [96]. Retrieve the float, open the electronics tube immediately, and inspect the moisture indicator strip and all internal surfaces. Inspect all external joints and penetration interfaces for weeping.
Pass criterion: Moisture indicator strip shows no colour change. No visible water droplets on any internal surface. All joints and penetrations dry on external inspection.

ATP-H04 — Piston travel under wet conditions
Materials: External wet cylinder, silicone grease, fresh water.
Procedure: Flood the external wet cylinder with fresh water and apply silicone grease to the piston O-rings. Translate the piston manually from fully retracted to fully extended and back, inspecting the O-rings visually at both stroke limits for rollover or extrusion.
Pass criterion: Piston completes the full ∼164 mm stroke in both directions without binding. No O-ring rollover or visible extrusion at the bulkhead or bore interface.

ATP-H05 — Neutral buoyancy verification
Materials: Pool or tank (≥1 m depth), reactive weight calculator output, ballast sand, scale.
Procedure: Calculate the equilibrium piston position using the reactive weight calculator and set the piston accordingly. Lower the float into the pool and release. Observe and record float depth over 60 s. If depth error exceeds ±50 mm, add or remove sand from the ballast ring in 5 g increments and repeat until equilibrium is achieved. Record the total trim adjustment.
Pass criterion: Float hovers within ±50 mm of the target depth for 60 s after trim.

ATP-H06 — Stability self-righting
Materials: Pool or tank, stopwatch.
Procedure: Hold the float horizontally just below the water surface, release, and simultaneously start a timer. Stop the timer when the float reaches vertical orientation (less than 10° from vertical). Repeat three times and record all righting times.
Pass criterion: Float self-rights to vertical in under 5 s across all three trials.

ATP-H07 — Sensor penetration seal
Materials: Sensor-actuator tube collar, all three sensor penetrations (Weipu WA22 bulkhead [76], TRN100 [75], MS5837 [54]), fresh water tank.
Procedure: Fit all three sensor penetrations to the collar. Submerge the sensor-actuator tube collar only to 0.5 m and hold for 5 min. Retrieve and inspect each penetration individually for weeping or ingress.
Pass criterion: No ingress at any of the three penetrations. Any weeping is cause for rework and retest before proceeding to ATP-H03.

13.6 Housing Materials

This appendix documents the materials used in the housing subsystem prototype, organised by category. Sensor and electronics components are documented in their respective subsystem chapters and are not duplicated here.

13.6.1 3D-Printed Components (PLA)

All structural housing components were fabricated from PLA filament on an FDM printer [43]. Table 13.3 lists each component with its measured filament consumption from the slicer.

Table 13.3: 3D-printed housing components with filament usage.

Component	Filament (g)	Notes
Top cap	89.69	Bayonet lock, GNSS radome
Electronics zone	185.88	Main electronics enclosure
Electronics balancer	17.77	Internal rail and balance mount
Sensor-actuator zone (top)	194.88	Upper actuator housing
Sensor-actuator zone (middle)	137.49	Shaft seal and guide region
Sensor-actuator zone (bottom)	157.32	Motor mount and lower end
AS5600 angle sensor mount	8.69	Internal to actuator zone [63]
MS5837 depth sensor mount	0.71	Collar penetration boss [54]
ECO FLNTU mount bracket	3.06	Collar mounting pad [74]
Mock ECO FLNTU body	74.54	Prototype testing only
TRN100 temperature sensor mount	1.88	G 1/4 threaded boss [75]
Ballast shell (weight lid)	67.53	Sand-filled annular shell
External cylinder	483.99	Outer wet cylinder
Total	**1423.43**	

13.6.2 Procured Structural and Sealing Materials

Table 13.4: Procured housing materials.

Component	Specification	Qty
NBR 70 O-ring	2.0 mm × 1.0 mm; MS5837 radial seal	1
NBR 70 O-ring cord, 3.53 mm	Bulk cord for piston and face seals	1
MCBH-6 bulkhead connector	CA6GS-E (Weipu WA22) [76], 6+PE, IP67	1
Building sand	Ballast fill material	3 kg

13.6.3 Recommendations for Field Deployment

For a deployable configuration, the following substitutions are recommended: EPDM O-rings throughout (in place of NBR) for improved low-temperature and saltwater performance [23]; PETG filament in place of PLA for improved moisture resistance and dimensional stability [21]; a machined 316 stainless steel ballast ring in place of the sand-filled shell for precise, moisture-stable ballast; and a fully depth-rated bulkhead connector (Blue Robotics MCBH-6 or equivalent) in place of the IP67-rated CA6GS-E used in the prototype. For any extended deployment, anti-fouling treatment of the ECO FLNTU optical window should also be considered [26].

Chapter 14

Evidence of Graduate Attributes

14.0.1 KRZDAN001

GA 3: Engineering Design

The ballast actuation subsystem demonstrates a complete, structured, and analytical engineering design process from user requirements through to validated implementation. User requirements were derived from the project brief and translated into functional requirements and measurable design specifications with corresponding acceptance test procedures. Design decisions, including actuation method selection, motor selection and drivetrain architecture were made by comparing alternatives against defined criteria, with the final choices explicitly justified.

The actuation method selection followed a structured comparative process. Thruster-based and buoyancy-based actuation methods were evaluated against performance, reliability, and autonomy criteria, with the ballast-based approach selected on the basis of robustness to biofouling and lower marine exposure risk, consistent with findings in the literature. Within buoyancy-based systems, variable mass and variable volume approaches were compared, with a piston-driven water ballast cylinder selected for its simplicity and suitability for the operating depth range.

The mechanical design followed an analytical process. The cylinder dimensions were derived from the required displaced volume to achieve the target buoyancy change, and the piston force requirements were calculated from hydrostatic pressure at the maximum design depth, with these being simulated to determine stress and structural integrity of the piston.

The lead screw was sized against buckling as the governing failure mode, and the drivetrain gear ratios were derived from the motor's peak efficiency operating point to ensure the motor operates near its optimal condition at maximum load. The worm gear lead angle was selected to satisfy the self-locking condition for the measured friction coefficient of the printed material, ensuring the piston holds position without power consumption between actuations. All specifications are traceable to user requirements, and all acceptance test procedures are traceable to specifications.

GA 7: Sustainability and Impact of Engineering Activity

The ballast actuation subsystem was designed with energy efficiency and long-duration autonomy as primary constraints, directly supporting the broader goal of enabling low-cost autonomous ocean monitoring in remote and logistically challenging environments. By using a worm gear drivetrain with a self-locking lead screw, the actuator consumes power only during piston movement and draws no current while maintaining a fixed depth at neutral buoyancy. This is a significant advantage over thruster-based depth control systems, which require continuous power to maintain depth, and directly extends the deployment autonomy of the system.

The use of 3-D printed components and commercially available low-cost motors and fasteners reduces the manufacturing cost of the system and increases accessibility for research institutions operating with limited budgets. The design was also developed with scalability in mind, with the analytical framework for cylinder sizing, gear ratio selection, and force calculation applicable to deeper deployment variants requiring only parameter updates in the code provided on the Github.

By enabling autonomous phytoplankton profiling in Antarctic waters, the system contributes to environmental monitoring capacity in a region where vessel-based sampling is prohibitively expensive and logistically constrained. This aligns with the sustainable development goal of protecting life below water and supporting Afro-centric research.

GA 8: Individual, Team and Multidisciplinary Working

At the individual level, the ballast actuation subsystem was designed, analysed, and validated independently, encompassing the mechanical design of the cylinder and piston, the analytical sizing of the lead screw and drivetrain, the selection and justification of the motor, and the development of all acceptance test procedures for the subsystem.

At the team level, the project was developed in parallel across subsystems with shared interface definitions established early in the design process. The Microsoft Teams channel contains records of design discussions, integration planning, and collaborative problem solving throughout the project period. The actuator subsystem interfaces directly with the depth control subsystem through the motor driver and with the power subsystem, requiring active coordination with team members responsible for those subsystems to ensure compatibility of electrical interfaces and control signals. Lastly, the subsystem also had to integrate with the housing, requiring close communication to ensure all aspects of the subsystem could be properly installed and secured.

The subsystem design required the integration of knowledge from multiple engineering disciplines, including fluid mechanics for hydrostatic force and buoyancy calculations, mechanical engineering for lead screw buckling analysis and gear geometry, and electrical engineering for motor selection and current budget analysis. Lastly, the system also required an understanding of the needs of Antarctic researches, communicating with Sandy and building a device for her field of study. The successful integration of these areas into a single coherent mechanical design demonstrates multidisciplinary engineering practice.

GA 10: Engineering Professionalism

The group's Microsoft Teams channel provides evidence of professional communication throughout the project, including technical design discussions, coordination of subsystem interfaces, and collaborative resolution of integration issues over the 10-week project period.

Professional engineering practice is further reflected in the structured and traceable approach to the design process, including the linking user requirements to functional requirements, design specifications, and acceptance test procedures. The use of analytical tools including MATLAB for parametric design calculations ensured that design decisions were made on a quantitative basis and remain reproducible and adjustable as system parameters evolve.

14.0.2 HNYPHI001

GA 3: Engineering Design

The depth control subsystem demonstrates a complete engineering design process from requirements definition to validated implementation. User requirements were derived from the project brief and translated into functional requirements and measurable design specifications through a traceability matrix linking each specification to an acceptance test procedure. Design decisions, including sensor selection, microcontroller selection, and controller architecture, were made by comparing alternatives against defined figures of merit, with the final choices explicitly justified.

The controller design followed a structured analytical process. The plant was modelled as a third-order electromechanical transfer function, validated against expected time constants, and simplified to a second-order model with justification. The inner loop compensator was designed in MATLAB using frequency-domain techniques, with gain and phase margins verified throughout. The outer loop gains were tuned using a full-physics simulation incorporating buoyancy dynamics not represented in the MATLAB model. This demonstrates an understanding of the limitations of each modelling tool and the selection of appropriate methods for different stages of the design process. The controller was then discretised, validated against the continuous-time design, and implemented in MicroPython using difference equations. All specifications are traceable to user requirements, and all acceptance tests are traceable to specifications.

GA 7: Sustainability and Impact of Engineering Activity

The AUV profiling float addresses the need for low-cost autonomous ocean monitoring in remote environments that are expensive and difficult to access using conventional research vessels. By enabling autonomous phytoplankton measurements in Antarctic waters, the system has the potential to reduce the dependence on vessel-based sampling while increasing the quantity of environmental data available to researchers.

The buoyancy-driven operating principle is energy efficient because power is required only during piston movement and not while maintaining depth at neutral buoyancy. This provides an advantage over thruster-based systems for long-duration profiling applications. The use of commercially available low-cost components also reduces the cost of deployment and increases accessibility for research institutions with limited resources. Although designed as a 2 m proof of concept, the control architecture and sensor interfaces were developed with scalability to deeper deployments in mind.

GA 8: Individual, Team and Multidisciplinary Working

At the individual level, each team member was responsible for the design, implementation, and validation of a specific subsystem.

At the team level, the project was developed in parallel across four subsystems with shared interface definitions established early in the design process. The Microsoft Teams channel contains records of design discussions, integration planning, and collaborative problem solving throughout the project.

The project also required integration of knowledge from multiple engineering disciplines, including control systems, embedded software, electromechanical systems, and fluid mechanics. The successful integration of these areas into a single working system demonstrates multidisciplinary engineering practice.

GA 10: Engineering Professionalism

The group's Microsoft Teams channel provides evidence of professional communication, including technical discussions, coordination of deliverables, and collaborative resolution of design issues throughout the 10-week project period.

Professional engineering practice is also reflected in the use of version-controlled code through a shared GitHub repository, centralised parameter management in parameters.py, and the inclusion of a dedicated hardware diagnostic script (hardware-test.py) for systematic subsystem testing.

14.0.3 MXNBUM001

GA 3: Engineering Design

The power subsystem shows engineering design through the systematic development of an electrical architecture that converts system-level energy needs into protected, regulated, and testable power-delivery functions. User requirements were translated into functional requirements and measurable specifications through the power load map, which identified the voltage rails, current demands, operating modes, noise sensitivities, and peak-current constraints of the actuator, controller, GNSS, and phytoplankton sensor interfaces.These requirements informed a protected 3S lithium battery architecture, regulated motor, logic, and research-instrument rails, branch-level protection, battery monitoring, and selective load switching.

The design decisions were justified through comparison, calculation, and verification. The 3S battery topology was selected over 2S because it provided better voltage headroom, lower battery-side current, and higher stored energy per pack row. Motor noise was addressed through load separation, star grounding, and an LC filter designed around the 20 kHz PWM frequency. The BTS7960 was selected over the L298N because it provided stronger current margin, lower conduction loss, and better fault protection for the highest-power load. The custom load-switch circuit was the only non-prebuilt section of the subsystem, so it was validated separately through sensitivity analysis to confirm acceptable switching behaviour for the low-current external loads. Physical testing then verified the main power-delivery functions, including battery sag, 3.3 V rail regulation and ripple, H-bridge PWM reversal, and cell balance. The failed off-state leakage test was analysed and used to motivate a clear recommendation for lower-leakage load-switch ICs.

GA 7: Sustainability and Impact of Engineering Activity

The project supports sustainability by enabling more efficient phytoplankton research in remote polar environments. By reducing dependence on research-vessel-based sampling, the AUV concept supports longer-term and more accessible environmental data collection in the Southern Ocean. The power subsystem contributes directly to this impact because deployment duration, energy efficiency, and reliable power delivery determine whether the sensing mission can be sustained.

Within the power subsystem, sustainability was addressed by selecting rechargeable lithium cells rather than disposable primary cells for the prototype, reducing material waste across repeated testing and deployment cycles. Energy efficiency was also prioritised through a battery-led architecture, efficient DC-DC conversion, selection of a low-loss motor driver, and selective switching of non-essential loads. The use of digital load switches allows sensors, GNSS, and research-instrument loads to be disconnected when inactive, reducing standby losses and preserving stored energy for mission-critical operation.

GA 8: Individual, Team and Multidisciplinary Working

Although the system was divided into four multidisciplinary modules (i.e actuation, control, power, and housing) the power subsystem required continuous integration with every other subsystem. Individually, the power work required independent design of the energy source, protection, regulation, filtering, monitoring, and switching architecture. However, these decisions could only be made correctly by understanding the electrical and physical needs of the whole AUV.

The actuator interface required understanding the motor power demand, stall risk and bidirectional operation. The controller interface required coordination around the Pico supply, sensor sensitivity, logic levels, switching control signals, and and the effect of 20 kHz PWM switching on the rest of the system. The housing interface required negotiation around board area, wiring layout, chamber separation, and connector placement. The power goal was to keep high-current and sensitive connections short to limit voltage drop and noise propagation, while the housing goal was to preserve dry and wet zone separation and maintain mechanical integration with the sensors and actuator. The final power subsystem was therefore not designed in isolation; it was shaped by continuous subsystem-level trade-offs and integration discussions.

GA 10: Engineering Professionalism

Engineering professionalism was demonstrated through structured communication, documented decision-making, and responsible project coordination. The team held weekly supervisor meetings, during which I took meeting minutes and converted them into actionable goals for the following sprint. This helped the group track progress, identify risks early, and assign clear follow-up tasks across the power, control, actuation, and housing subsystems.

Professional communication was also maintained through Microsoft Teams, where the group discussed technical decisions, coordinated ordering and delivery issues, and resolved integration problems as they arose. In addition to written communication and physical meetings, the team used Teams calls to check progress, align subsystem interfaces, and plan the next stages of implementation. This ensured that design changes in one subsystem, such as actuator current demand, sensor placement, or housing space constraints, were communicated before they caused integration failures.

14.0.4 LNGLUL002

GA 3: Engineering Design

The housing subsystem demonstrates a complete engineering design process from requirements definition through to physical prototype validation. User requirements were translated into five functional requirements, each mapped to measurable design specifications and traceable acceptance test procedures (ATP-H01 through ATP-H07). Three candidate architectures were evaluated using a weighted decision matrix against criteria including waterproofing reliability, manufacturability, and field serviceability.

Structural analysis combined an analytical buckling model with FEA in SimScale, confirming safety factors of 11.5 to 59.7 across the three primary components. A reactive weight calculator produced a verified CB to CM separation of 28.2 % of float length, confirming passive stability across a $\pm 5\,\%$ parameter sweep. Five of seven ATPs passed on the prototype, with the two failures correctly attributed to PLA material porosity rather than a seal design failure, demonstrating honest and evidence-based engineering judgement.

GA 7: Sustainability and Impact of Engineering Activity

The housing is the component that makes autonomous long-term ocean deployment physically possible. By providing a sealed, pressure-resistant enclosure for all electronics and sensors, it directly enables the broader goal of replacing costly, carbon-intensive research vessel campaigns with persistent autonomous monitoring platforms in Antarctic waters.

Material and manufacturing choices were made with accessibility and sustainability in mind. FDM-printable geometry and off-the-shelf hardware keep fabrication costs low and make the design reproducible by research groups without access to specialised machining. The modular architecture was a deliberate design priority throughout, keeping the footprint compact and ensuring individual zones can be accessed, repaired, or replaced independently without disturbing the rest of the assembly. This reduces material waste, lowers servicing costs, and simplifies field debugging compared to a monolithic design that would require full disassembly or replacement upon failure.

GA 8: Individual, Team and Multidisciplinary Working

The housing was the most physically interdependent subsystem in the project, as every other subsystem either mounts inside it, passes through it, or depends on its sealing integrity to function. Internal geometry decisions had to simultaneously account for the actuator piston travel range, the power electronics footprint, and the sensor penetration positions, requiring ongoing coordination with all three other subsystem designers. When 3D printing delays and wet testing failures caused integration to stall, diagnosing the root cause and communicating a concrete remediation path to the team was itself a significant exercise in collaborative problem solving.

The subsystem also demanded breadth across disciplines not typically combined in a single design task, including structural mechanics, fluid mechanics for buoyancy and stability, materials engineering for seal compatibility, and mechanical design for the piston and sensor interfaces.

GA 10: Engineering Professionalism

Professional practice is demonstrated through the structured use of a requirements traceability matrix, formal acceptance test procedures with documented outcomes, and explicit acknowledgement of prototype limitations alongside a clear remediation plan. The analysis of the PLA porosity findings, which correctly distinguished a manufacturing limitation from a design failure, reflects the kind of evidence-based technical judgement expected of a professional engineer.

All project deadlines were met and contributions to the shared Overleaf document were made consistently throughout the ten-week development period.

Bibliography

[1] Cell Manufacturer, "Selected 18650 lithium-ion cell datasheet," https://www.batteryspace.com/, n.d., datasheet for the selected 3.7 V, 2.6 Ah 18650 Li-ion cell.

[2] Parker Hannifin Corporation, "Parker o-ring handbook," https://www.parker.com, 2022.

[3] Quectel, "Cd-pa1010d gnss patch antenna module datasheet," https://www.quectel.com, 2022.

[4] D. Righetti *et al.*, "Global pattern of phytoplankton diversity driven by temperature and environmental variability," *Science Advances*, vol. 5, no. 5, p. eaau6253, 2019.

[5] P. Prakash *et al.*, "Phytoplankton dynamics in the antarctic marginal ice zone: Trends and drivers," *Journal of Marine Systems*, 2025.

[6] M. Lin and C. Yang, "Ocean observation technologies: A review," *Chinese Journal of Mechanical Engineering*, vol. 33, no. 32, 2020.

[7] S. C. Riser *et al.*, "Ocean observation and climate monitoring using autonomous platforms," *Frontiers in Marine Science*, 2022.

[8] W. Xu and T.-C. Su, "A self-sustaining autonomous system for long-term arctic monitoring," *Applied Ocean Research*, vol. 154, p. 104316, 2025.

[9] Argo Science Team, "On the design and implementation of argo: A global array of profiling floats," GODAE/CLIVAR, Tech. Rep., 1998.

[10] T. Morris *et al.*, "Best practices for core argo floats - part 1: getting started and data considerations," *Frontiers in Marine Science*, vol. 11, 2024.

[11] Y. Bai, R. Hu, Y. Bi, C. Liu, Z. Zeng, and L. Lian, "Design and depth control of a buoyancy-driven profiling float," *Sensors*, vol. 22, no. 7, p. 2505, 2022.

[12] T.-S. Kim, J. Kim, and S.-C. Yu, "Design of a buoyancy controllable auv by changing volume for data collection in the water column," in *IEEE/OES Autonomous Underwater Vehicle Workshop (AUV)*, 2018, pp. 1–3.

[13] X. André *et al.*, "Preparing the new phase of argo: Technological developments on profiling floats in the naos project," *Frontiers in Marine Science*, vol. 7, p. 577446, 2020.

[14] E. Petritoli and F. Leccese, "Autonomous underwater glider: A comprehensive review," *Drones*, vol. 9, no. 1, p. 21, 2025.

[15] P. Testor *et al.*, "Autonomous surface and underwater vehicles as effective ecosystem monitoring platforms," *Sensors*, vol. 21, no. 20, p. 6752, 2021.

[16] S. Fan, N. Bose, and Z. Liang, “Polar auv challenges and applications: A review,” *Drones*, vol. 8, no. 8, p. 413, 2024.

[17] L. Paull, S. Saeedi, M. Seto, and H. Li, “Auv navigation and localization: A review,” *IEEE Journal of Oceanic Engineering*, vol. 39, no. 1, pp. 131–149, 2014.

[18] S. Rysgaard, J. Bendtsen, W. Boone, D. F. Carlson, H. H. Christiansen, B. Elberling, S. B. Hansen, J. Mortensen, T. Juul-Pedersen, S. H. Mernild, M. Olsen, D. Petersen, M. Rasch, J. C. Refsgaard, T. Riis, M. Rysgaard, A. M. Solgaard, D. Tran *et al.*, “A mobile observatory powered by sun and wind for near real time measurements of atmospheric, glacial, terrestrial, limnic and coastal oceanic conditions in remote off-grid areas,” *HardwareX*, vol. 12, p. e00331, 2022.

[19] I. P. Morales-Aragón, J. Giménez-Gallego, J. Gilabert, R. Torres-Sánchez, and F. Soto-Valles, “Design and application of depth control methods for autonomous underwater profilers in challenging marine environments,” *Results in Engineering*, vol. 25, 2025.

[20] M. Choyekh, N. Kato, R. Dewantara, H. Senga, and H. Chiba, “Depth and altitude control of an auv using buoyancy control device,” *Journal of Electrical Engineering*, vol. 4, pp. 133–149, 2016.

[21] M. Govindaraj, N. M. H. Narayanarao, K. Munishaiah, and R. Nagappa, “Comparative study of metallic and polymer composite shells for underwater vessels using fea,” *International Journal of Ocean System Engineering*, vol. 3, no. 3, pp. 136–141, 2013.

[22] N. Vedachalam, S. Ramesh, A. N. Subramanian, D. Sathianarayanan *et al.*, “Design and development of remotely operated vehicle for shallow waters and polar research,” *Marine Technological Society Journal*, vol. 48, no. 5, 2014.

[23] A. H. Haghighi, V. Mobaraki, S. M. R. Shayegani, and M. Sharif, “Introducing the elastomers with lowest water absorption and permeability,” *Results in Chemistry*, vol. 16, p. 102485, 2025.

[24] J. Rabault, G. Sutherland, O. Gundersen, A. Jensen, A. Marchenko, and Ø. Breivik, “An open source, versatile, affordable waves in ice instrument for scientific measurements in the polar regions,” *Cold Regions Science and Technology*, vol. 170, p. 102955, 2020.

[25] J. Rabault *et al.*, “A position and wave spectra dataset of marginal ice zone dynamics collected around svalbard in 2022 and 2023,” *Scientific Data*, vol. 11, p. 1417, 2024.

[26] D. V. Manov, G. C. Chang, and T. D. Dickey, “Methods for reducing biofouling of moored optical sensors,” *Journal of Atmospheric and Oceanic Technology*, vol. 21, no. 6, pp. 958–968, 2004.

[27] M. Elkolali, A. Al-Tawil, and A. Alcoce, “Design and testing of a miniature variable buoyancy system for underwater vehicles,” *IEEE Access*, vol. 10, 2022.

[28] Y. Zhang, H. Deng, and Y. Li, “Depth control of auv using sliding mode active disturbance rejection control,” in *2018 3rd International Conference on Advanced Robotics and Mechatronics (ICARM)*, 2018, pp. 1–6.

[29] J. Rabault, J. Voermans, K. Filchuk, A. Jensen, Ø. Breivik, G. Sutherland, O. Gundersen, and A. Marchenko, “Openmetbuoy-v2021: An easy-to-build, affordable, customizable, open-source

instrument for oceanographic measurements of drift and waves in sea ice and the open ocean," *Geosciences*, vol. 12, no. 3, p. 110, 2022.

[30] M. Noyce, "Uct sharc buoy v3.0: Waves-in-ice measurement in the antarctic miz," Master's thesis, University of Cape Town, 2023.

[31] H. Jung, B. Friedman, W. Hwang, A. Copping, R. Branch, and Z. D. Deng, "Self-powered arctic satellite communication system by harvesting wave energy using a triboelectric nanogenerator," *Nano Energy*, vol. 114, p. 108633, 2023.

[32] G. Zuo, H. Huang, and H. Chen, "Performance analysis of an ice-based buoy operating from the packed ice zone to the marginal ice zone with an imaging system," *Journal of Marine Science and Engineering*, vol. 13, no. 9, p. 1717, 2025.

[33] Y. Sun, X. Qin, L. Li, Y. Zhang, J. Zhang, and J. Qi, "The impact of temperature on the performance and reliability of li/socl$_2$ batteries," *Energies*, vol. 17, p. 3063, 2024.

[34] C. W. I. McAfee, J. Rix, S. J. Quirk, P. G. D. Anker, A. M. Brisbourne, and K. Makinson, "Non-contact measurement system for hot water drilled ice boreholes," *Annals of Glaciology*, vol. 62, no. 85–86, pp. 223–232, 2021.

[35] Y. Zhang *et al.*, "State-of-the-art underwater vehicles and technologies enabling smart ocean," *arXiv preprint arXiv:2412.18667*, 2024.

[36] J. Smith *et al.*, "Adaptive robotic sampling and ocean monitoring systems," *HardwareX*, 2025.

[37] B. Garau, A. Alvarez, and G. Oliver, "Long-range route planning for autonomous vehicles in polar oceans," in *IEEE Conference Proceedings*, 2024.

[38] X. Wang *et al.*, "Autonomous underwater glider: A comprehensive review," *Drones*, vol. 9, no. 1, p. 21, 2024.

[39] T. D. A. Khatwate, Kunder, "Optimization of power screw material used in screw jack," *International Journal of Emerging Trends in Research*, 2025.

[40] Guruswamy, "Performance analysis of buck, boost, and buck-boost converters under variable load condition," *World Journal of Advanced Research and Reviews*, 2020.

[41] Mantech, "Dyd3430d024," *Datasheet*, 2026.

[42] M. Takriti, "A comprehensive guide on dc motor efficiency," *International Journal of Engineering Research and Applications*, 2025.

[43] A. et. al, "Tensile behavior of 3d printed polylactic acid (pla) based composites reinforced with natural fib," *Polymers*, 2022.

[44] d. O. T. Cardoso, De Oliveira, "3d printed parts of polylactic acid reinforced with carbon black and alumina nanofillers for tribological applications," *Macromolecular Symposia*, 2020.

[45] K. Harrington, "Characterization of small dc brushed and brushless mot," *Army Research Laboratory*, 2013.

[46] S. et. al, "The influence of worm gear material and lubricant on the efficiency and coefficient of friction," *Tribology and Materials*, 2024.

[47] Creality, "3d printing infill patterns: Strength, speed, and efficiency," *Creality.com*, 2025.

[48] A. Elhamid, "Cascade control system of direct current motor," *World Applied Sciences Journal*, vol. 18, pp. 1680–1688, 01 2012.

[49] Ibrahim, Mazree and Sy Salim, Sy Najib and Kamarudin, Muhammad Nizam and Noordin, Aminurrashid, "Cascade control of dc motor with inner speed and outer position loop," https://www.researchgate.net/publication/258432089_Real_Time_Cascade_PI_Control_for_Position_Monitoring_of_DC_Brushed_Motor, 2009.

[50] ScienceDirect Topics, "Nyquist theorem," https://www.sciencedirect.com/topics/engineering/nyquist-theorem, 2026.

[51] Wayne State University, Department of Electrical and Computer Engineering, "Practical sampling and the nyquist criterion," https://neuron.eng.wayne.edu/auth/ece4330/practical_sampling.pdf, 2018.

[52] Motion Control Tips, "Servo motor current, velocity, position loops and bandwidths," https://www.motioncontroltips.com/faq-servo-motor-current-velocity-position-loops-bandwidths/, 2024.

[53] TE Connectivity, "Ms5837-02ba01 pressure sensor datasheet," https://cdn.sparkfun.com/assets/3/0/9/3/8/ENG_DS_MS5837-02BA01_A8.pdf, 2015.

[54] ——, "Ms5837-30ba pressure sensor datasheet," https://www.tinytronics.nl/product_files/005046_ENG_DS_MS5837-30BA_C3.pdf, 2015.

[55] Raspberry Pi Ltd, "Raspberry pi pico datasheet," https://pip-assets.raspberrypi.com/categories/610-raspberry-pi-pico/documents/RP-008307-DS-1-pico-datasheet.pdf, 2021.

[56] Espressif Systems, "Esp32 series datasheet," https://documentation.espressif.com/esp32_datasheet_en.pdf, 2023.

[57] Arduino, "Arduino nano 33 iot datasheet," https://docs.arduino.cc/resources/datasheets/ABX00027-datasheet.pdf, 2020.

[58] ——, "Arduino uno rev3 datasheet," https://docs.arduino.cc/resources/datasheets/A000066-datasheet.pdf, 2021.

[59] STMicroelectronics, "Stm32h743vi microcontroller datasheet," https://www.st.com/resource/en/datasheet/stm32h743vi.pdf, 2024.

[60] Raspberry Pi Ltd, "Raspberry pi compute module 4 datasheet," https://pip-assets.raspberrypi.com/categories/634-raspberry-pi-compute-module-4/documents/RP-008168-DS-3-cm4-datasheet.pdf, 2021.

[61] WayCon Positionsmesstechnik GmbH, "Lms18 linear potentiometer datasheet," https://www.waycon.biz/fileadmin/linear-potentiometers/Linear-Potentiometer-LMS18.pdf, 2021.

[62] Omron Corporation, “E6c2-c incremental rotary encoder datasheet,” https://www.mouser.com/datasheet/2/307/e6c-n_ds_csm492-45791.pdf, 2015.

[63] AMS AG, “As5600 magnetic rotary position sensor datasheet,” https://files.seeedstudio.com/wiki/Grove-12-bit-Magnetic-Rotary-Position-Sensor-AS5600/res/Magnetic%20Rotary%20Position%20Sensor%20AS5600%20Datasheet.pdf, 2018.

[64] RLS Merilna tehnika, “Mbd01 magnetic encoder datasheet,” https://www.rls.si/media/wysiwyg/RLS/datasheet/MBD01_02.pdf, 2020.

[65] LibreTexts, “An electro-mechanical system model,” https://eng.libretexts.org/Bookshelves/Industrial_and_Systems_Engineering/Introduction_to_Control_Systems_(Iqbal)/01:_Mathematical_Models_of_Physical_Systems/1.04:_An_Electro-Mechanical_System_Model, 2024.

[66] EEEGuide, “Transfer function of armature controlled dc motor,” https://www.eeeguide.com/transfer-function-of-armature-controlled-dc-motor/, 2024.

[67] MathWorks, “Edit compensator dynamics,” https://www.mathworks.com/help/control/ug/edit-compensator-dynamics.html, 2024.

[68] Toronto Metropolitan University, “Lead controller,” https://pressbooks.library.torontomu.ca/controlsystems/chapter/13-2lead-controller/, 2024.

[69] Alvarez Technology Group, “Pid control with matlab and simulink, chapter 7,” http://alvarestech.com/temp/smar/PID-MatLab-Simulink/ch07.pdf, 2010.

[70] California Institute of Technology, “Feedback systems: Controller design,” https://www.cds.caltech.edu/~murray/courses/cds101/fa04/caltech/am04_ch9-3nov04.pdf, 2004.

[71] Massachusetts Institute of Technology, “Multivariable control systems lecture 11,” https://ocw.mit.edu/courses/6-245-multivariable-control-systems-spring-2004/e7aeed6b7a0d508ad3632c9a46b9a21d_lec11_6245_2004.pdf, 2004.

[72] International Rectifier, “Irf9530n hexfet power mosfet,” https://www.infineon.com/, 1998, datasheet, PD-91482C.

[73] Microchip Technology Inc., “2n7000 n-channel enhancement-mode vertical dmos fet,” https://www.microchip.com/, 2021, datasheet, DS20005695A.

[74] Sea-Bird Scientific, “Wetlabs eco flntu chlorophyll/turbidity sensor datasheet,” https://www.comm-tec.com.

[75] TE Connectivity, “Stainless steel threaded temperature sensor datasheet,” https://www.te.com, 2023.

[76] Weipu Connector, “Wa22 series waterproof connector datasheet,” http://archive.communica.co.za/Content/Catalog/Documents/D4048518423.pdf, 2023.

[77] TE Connectivity, "Ms5837 o-ring mount application note," https://www.scribd.com/document/591900498/ENG-SS-Application-Note-MS5837-O-Ring-mount-A.

[78] W. C. Young and R. G. Budynas, *Roark's Formulas for Stress and Strain*, 8th ed. McGraw-Hill, 2011.

[79] RS Components, "Rs pro dc motor, 24.6 w, 3–7.2 v dc, rs stock no. 238-9721," https://uk.rs-online.com/, n.d., datasheet.

[80] Handson Technology, "Bts7960 high current 43a h-bridge motor driver," https://www.handsontec.com/, n.d., user guide, SKU: DRV-1012.

[81] XLSEMI, "Xl6009 400 khz 60 v 4 a switching current boost, buck-boost and inverting dc/dc converter," https://www.xlsemi.com/, n.d., datasheet, Rev. 1.1.

[82] Texas Instruments, "Lm340, lm340a and lm78xx wide vin 1.5-a fixed voltage regulators," https://www.ti.com/lit/ds/snosbt0k/snosbt0k.pdf, 2016, datasheet, SNOSBT0K, revised July 2016.

[83] Raspberry Pi Ltd, "Raspberry pi pico datasheet," https://datasheets.raspberrypi.com/pico/pico-datasheet.pdf, n.d., rP-008307-DS-1.

[84] TE Connectivity, "Ms5837-30ba ultra-small gel-filled pressure sensor with stainless steel cap," https://www.te.com/, 2019, datasheet, Rev. C2, December 2019.

[85] ams AG, "As5600 12-bit programmable contactless potentiometer," https://ams-osram.com/, 2018, datasheet, v1-06, 20 June 2018.

[86] Handson Technology, "Lm2596s step down 3a dc-dc converter," https://www.handsontec.com/, n.d., data specs, SKU: MDU-1050.

[87] Sea-Bird Scientific and WET Labs, "Eco flntu fluorometer and scattering meter," https://www.seabird.com/, 2014, datasheet, Rev. October 2014.

[88] TE Connectivity Sensors, "Trp100 and trn100 stainless steel threaded temperature sensor," https://www.te.com/, 2026, datasheet, Rev. B2, April 2026.

[89] CDTop Technology, "Cd-pa1010d gnss patch antenna module data sheet," https://www.cdtop-tech.com/, n.d., datasheet.

[90] Seeed Studio, "Rs-232 to ttl converter based on max3232idr," https://wiki.seeedstudio.com/RS-232_To_TTL_Converter_MAX3232IDR/, n.d., module datasheet / product documentation.

[91] Texas Instruments, "Ina226 36 v, 16-bit, ultra-precise i2c output current, voltage, and power monitor with alert," https://www.ti.com/lit/ds/sbos547b/sbos547b.pdf, 2024, datasheet, SBOS547B, revised September 2024.

[92] STMicroelectronics, "L298 dual full-bridge driver datasheet," https://www.st.com/resource/en/datasheet/l298.pdf, 2000, datasheet.

[93] Analog Devices, “Ltc3780 high efficiency, synchronous, 4-switch buck-boost controller datasheet,” https://www.analog.com/media/en/technical-documentation/data-sheets/3780ff.pdf, n.d., datasheet.

[94] J. L. Meriam and L. G. Kraige, *Engineering Mechanics: Statics*, 8th ed. Wiley, 2015.

[95] B. R. Munson, D. F. Young, and T. H. Okiishi, *Fundamentals of Fluid Mechanics*, 7th ed. Wiley, 2012.

[96] International Electrotechnical Commission, “Iec 60529: Degrees of protection provided by enclosures (ip code),” https://www.iec.ch/standard/41738, 2013.